Use of numerical models and satellite data to study physical processes in Lake Baikal

Thesis submitted for the degree of
Doctor of Philosophy
at the University of Leicester

by

Helen Louise Le Core
Department of Physics and Astronomy
University of Leicester

September 1998

ProQuest LLC
789 East Eisenhower Parkway
P.O. Box 1346
Ann Arbor, MI 48106-1346

To my Parents

"Well, I mean, *yes* idealism, *yes* the dignity of pure research, *yes* the pursuit of truth in all its forms, but there comes a point I'm afraid where you begin to suspect that if there's any *real* truth, it's that the entire multi-dimensional infinity of the Universe is almost certainly being run by a bunch of maniacs."

"The Hitch Hiker's Guide to the Galaxy" - D. Adams

Use of numerical models and satellite data to study physical processes in Lake Baikal

Helen Louise Le Core

Presented for the degree of Doctor of Philosophy
at the University of Leicester, 1998

Abstract

The survival of Lake Baikal's unique flora and fauna, of over 1500 endemic species, depends on water circulation carrying oxygen to all depths. However, the mechanisms by which this takes place are not well understood. A three-dimensional model of the lake has been developed, which is the first to be discussed in the open literature. The model, in conjunction with satellite data, is demonstrated to be particularly useful for investigating mixing processes occurring in the upper layer when the lake surface is frozen. Model generated temperature-depth profiles show that mixing extends to a depth of 40 m under regions of snow-free ice, compared to 15 m under snow-covered ice (after a period of 8 days). The model can, therefore, provide an indication of diatom populations (a vital part of the food chain), as these are larger in regions where convective mixing is most active.

Satellite data are analysed to assess the spatial and temporal distribution of snow and ice cover, in order to study density driven currents caused by non-uniform solar heating through the ice and snow. Incorporating these into the model generates current speeds of about 5×10^{-3} m s^{-1}, an order of magnitude smaller than those observed in the lake. This suggests that current flow in the real lake may not be purely density driven, as was previously thought.

Other features observed in satellite images include thermal bars and gyres, both possible mechanisms for deep circulation of water. Thermal bars occur primarily along the south coast of the Central Basin, during June. Numerical modelling experiments suggest that gyre formation is due to the combination of a north-west wind, the Coriolis effect, and the presence of the steep Academician Ridge separating the Central and North Basins.

Finally, as regards the ice-free lake, it has been suggested that deep water ventilation might occur if internal waves are able to displace the thermocline downwards to a depth sufficient to cause 'thermobaric instability'. Model results show that wind speeds greater than 40 m s^{-1} must be uniformly applied to the surface of the lake for 1 to 2 days for the depth criterion to be met. It therefore seems unlikely that deep water ventilation is due to wind-induced internal waves.

Acknowledgements

This thesis only exists due to the help and support of a large number of people. I would firstly like to thank my supervisors, Professor David Llewellyn-Jones and Dr Sean Lawrence, for introducing me to Lake Baikal, initiating this research, and invaluable assistance throughout. Many thanks also to Dr David Jewson, from the University of Ulster, for his helpful suggestions and discussions on the focus of this study, background information and a great deal of data. Thanks to Dr Rolf Kipfer, from EAWAG/ETH in Switzerland, for his hospitality during my visit to Zurich, and for introducing me to the local cuisine. For other help, data and information thanks go to Dr Nick Granin from the Siberian Institute of Limnology in Irkutsk, and Dr Anthony Kay from the University of Loughborough. This work would not have been possible, of course, without funding, for which I thank the Natural Environment Research Council. Satellite data from the ATSR instruments are courtesy of the Rutherford Appleton Laboratory.

These acknowledgements would not be complete without a huge 'thank you' to the other members of the Earth Observation Science group at Leicester, both for academic assistance and for making the last four years such an enjoyable experience. Thanks especially to Will, Andrew, Ian, Rowan and Tom. To my family and all my friends, many thanks for being there through thick and thin. Special thanks go to Jane for being a wonderful listener and true friend, and to Gregg, Allison, Viv and Neil for all the excellent 'house' re-unions.

To my parents, much love and gratitude for their constant support and encouragement, and for giving me the opportunity to go so far.

Contents

Abstract iv

Acknowledgements v

Contents vi

1. Introduction 9

1.1 Overview 9

1.2 Lake Baikal 10

1.2.1 Upper layer dynamics and diatom motions 11

1.2.2 Deep water processes 13

1.3 Remote sensing from satellites 16

1.3.1 Principles of thermal remote sensing 16

1.3.2 Cloud detection 18

1.3.3 An overview of the ATSR instruments 18

1.4 Numerical modelling 20

2. Observations of physical processes using satellite data 22

2.1 Overview 22

2.2 Thermal bars 22

2.2.1 Temperature transects 24

2.2.2 Histogram plots 28

2.3 Gyres 34

2.4 Coastal upwelling 37

2.5 Suspended sediment plumes 38

3. Snow and Ice cover 42

3.1 Overview 42

3.2 Description of ice cover on Lake Baikal 43

3.3 Detection of snow/ice cover using infra-red satellite data 47

3.4 Detection of snow/ice cover using visible wavelength satellite data 50

3.5 Use of NDSI and Near IR to detect ice and snow 53

3.5.1Quantitative analysis of ice-covered period 59

4. Single layer barotropic model 60
4.1 Overview 60
4.2 Model description 60
4.2.1 Finite difference equations used in the model 64
4.2.2 Stability analysis 65
4.3 Model initialisation 66
4.4 Results 68
4.4.1 Wind stress 68
4.4.2 Viscosity 74
4.4.3 River inflow/outflow 74
4.5 Summary and discussion 80

5. Multi-layer baroclinic model 83
5.1 Overview 83
5.2 Introduction to the problems 83
5.3 Overview of the model 84
5.3.1 Stability requirements 85
5.3.2 Equations of motion 86
5.3.3 Adaptations to fresh water lake 86
5.3.4 Conversion to *N* layers 86
5.4 Parameterisation of physical processes 87
5.4.1 Solar heating 87
5.4.2 Ice and snow layer 88
5.4.3 Wind stress 89
5.4.4 Convective mixing 89
5.4.5 Turbulent mixing 89
5.5 Vertical structure 92
5.6 Model runs investigating under-ice flow 93
5.6.1 Mixing schemes 94
5.6.2 Albedo and extinction coefficients 94
5.6.3 Snow thickness 95
5.7 Results from R1 95
5.7.1 Temperature profile development 95
5.7.2 Surface temperature 99
5.7.3 Under-ice currents 99

5.8 Results from R2 105
5.8.1 Temperature profile development 105
5.8.2 Under-ice currents 106
5.9 Results for R3 and R4 108
5.9.1 Temperature 110
5.9.2 Under-ice currents 110
5.9.3 Summary 111
5.10 Results for R5 111
5.10.1 Temperature 111
5.10.2 Under-ice currents 113
5.10.3 Summary 114
5.11 Results for R0 and R6 115
5.11.1 Temperature 115
5.11.2 Under-ice currents 118
5.11.3 Summary 118
5.12 Model runs investigating internal waves 122

6. Conclusions and Summary 125
6.1 Conclusions 125
6.2 Summary and discussion of results 126
6.2.1 Satellite data 126
6.2.2 Ice and snow cover 126
6.2.3 Barotropic model 128
6.2.4 Multi-layer model 129
6.3. Discussion of results from the baroclinic model 131
6.4. The relative merits of other modelling techniques 132
6.5. Suggestions for further work 132
6.5.1. The formation of gyres 132
6.5.2 Thermal bars and gyres as a mechanism for deep water ventilation 133
6.5.3 Current flow under ice 133
6.5.4 Investigation of deep water processes 133

7. Bibliography 134

1. Introduction

1.1 Overview

Lake Baikal is unique in many ways and has been the subject of much scientific study (Kozhov, 1963; Shimaraev *et al.*, 1994). The aim of the research described in this thesis is to explore the physical processes that occur in the lake. A number of techniques are required in order to study the lake system: *in situ* data forms an important basis but is sparse and not easily obtainable; satellite data provide good spatial and temporal coverage but only of the surface; therefore, a numerical model, into which both *in situ* and satellite data can be integrated, is used to investigate the hydrodynamics of the lake.

In this introductory chapter, section 1.2 provides an introduction to Lake Baikal, and a discussion of the problems under consideration. These include circulation in the upper few hundred metres of the lake and the mechanisms by which surface water can be transported to great depths. Satellite data are used to determine the surface conditions of the lake during the period of ice-cover, which has a great influence on the development of the temperature structure and circulation patterns. Therefore, section 1.3 gives a brief introduction to the technique of thermal remote sensing from satellites. Finally, numerical modelling, and its application in this work, is described in section 1.4.

Chapter 2 presents the results of using satellite data to observe physical processes. Among the features observed are thermal bars, gyres, coastal upwelling and suspended sediment plumes. Particular emphasis is placed on the detection of thermal bars, as these are thought to be one of the mechanisms which cause deep water ventilation events.

Chapter 3 discusses the use of satellite data to detect snow and ice cover. The aim of this is to obtain classification 'maps' of the lake surface, showing particular types of ice or snow, at a number of times throughout the ice-covered period. By assigning albedo and extinction coefficients to each classification type, these maps can be integrated into the numerical model as a means of determining the amount of light (and hence heat) which penetrates beneath the ice.

A single layer barotropic model is described in Chapter 4. Gyres, observed in satellite data of the lake (Chapter 2), could be another mechanism involved in the ventilation of deep water. The model is, therefore, used to determine the factors that influence their formation.

Chapter 5 introduces the multi-layer baroclinic model, developed in order to study hydrodynamic processes in the lake. A description of the model and the parameterisations used is followed by results from model runs investigating under-ice current flow, convective mixing

processes and the generation of internal waves as a means of causing deep water ventilation events.

Finally, Chapter 6 draws together the conclusions, and suggestions are made for further work.

1.2 Lake Baikal

Lake Baikal contains about 20% of the world's liquid fresh water. It is the deepest and also the oldest lake on Earth, having an estimated age of 30 million years (Kozhov, 1963; Logatchev, 1993; Callender and Granina, 1997). Baikal is a rift lake in south-eastern Siberia, composed of three distinct basins, as can be seen in Figure 1.1. The Selenga Delta region, a vast accumulation of sediment formed over many millennia, separates the South and Central basins. The Academician Ridge separates the Central and North basins, the peak of the ridge lying 300-400 m below the surface. The deepest part of the lake lies at 1,638 m, on the south side of the steep ridge. All three basins are steep-sided, significantly more so along the north-west coast. Baikal annually receives up to 60 km^3 of water from river inlets (Granina, 1997), 70% of this is from just three rivers: the Selenga, Barguzin and Upper Angara (Kozhov, 1963). Around three hundred others contribute the rest. The only outlet is the Lower Angara in the south, the considerable power of which has been harnessed by a chain of hydroelectric power stations (Kozhov, 1963). The climate in the Lake Baikal region is continental: the winters are long, cold and dry; the summers are short and relatively warm. The lake has a significant influence on the coastal climate; winter temperatures along the coast tend to be up to 10°C warmer than those inland, and summer temperatures cooler by around 7°C (Kozhov, 1963). The duration of ice cover is typically four to five months each year, with a maximum ice thickness of around one metre.

One of the features of this ancient lake is its high biodiversity, including over a thousand endemic species. In other comparably deep lakes, such as Malawi (706 m) and Tanganyika (1435 m) in Africa, the waters are anaerobic below about 300 m. In Lake Baikal, however, the water contains sufficient oxygen to support species even at a depth of 1600 m. Baikal has the unique ability of being able to circulate water and, therefore, oxygen, down to its greatest depths. It is not, however, fully understood how this circulation takes place (Shimaraev *et al.*, 1994). Section 1.2.2 describes this problem in more detail.

At the base of the food chain are many species of phytoplankton, including diatoms. Since planktonic diatoms are non-motile, the vertical and horizontal circulation of water within the upper layer (the top few hundred metres of the lake in which the majority of mixing occurs) is vital to their survival. However, they can vary their sinking rate (Moore and Villareal, 1996). Due to the major role the diatoms have in the lake ecosystem, it is important to understand how water circulates within the lake and, hence, the distribution of properties such as dissolved oxygen, nutrients, pollutants and the diatoms themselves. The dynamics of the upper layer of the lake, and how it relates to diatom motions, is discussed in Section 1.2.1 below.

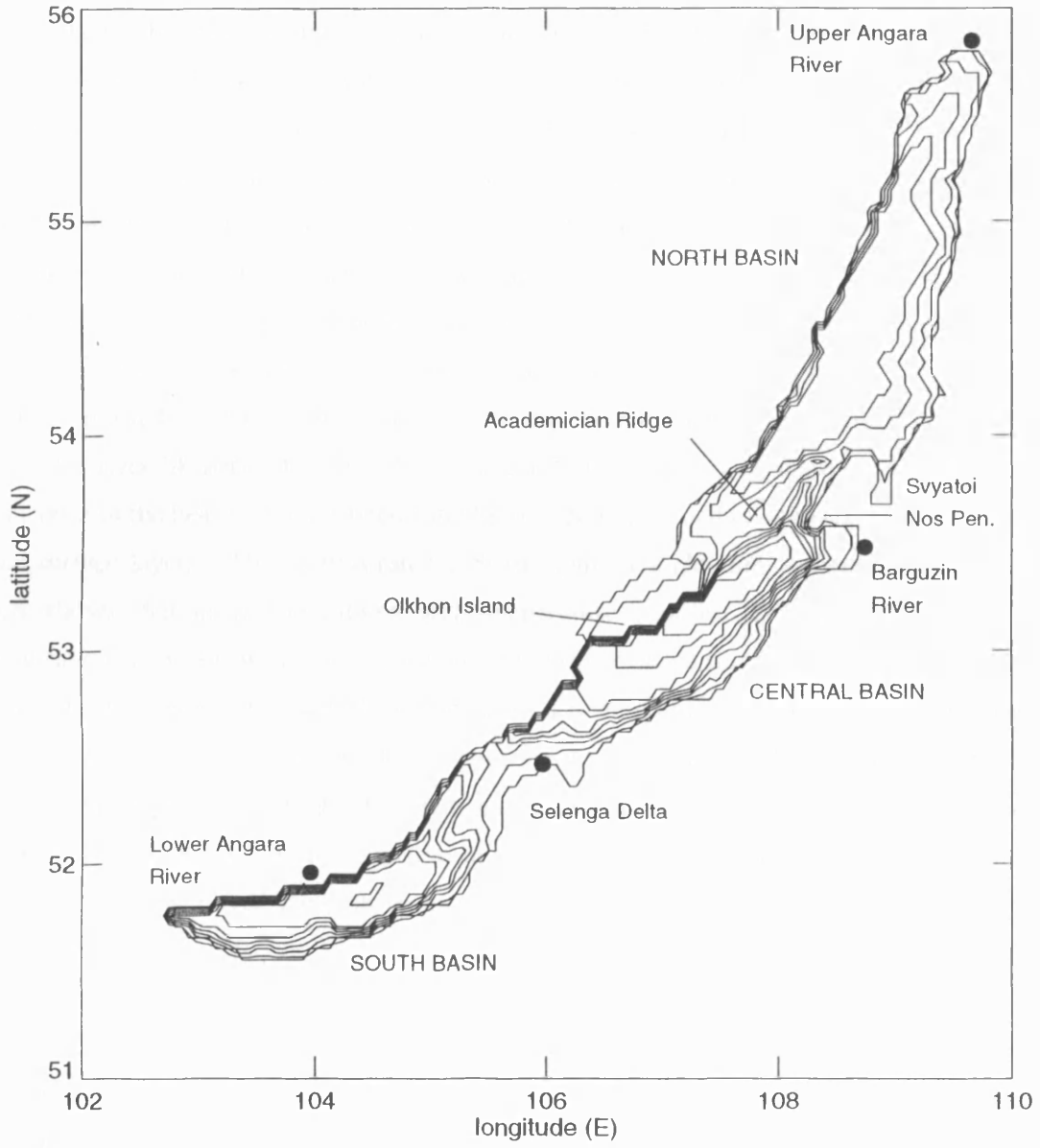

Figure 1.1: Bathymetry of Lake Baikal, with contour intervals of 200 m, showing the important locations such as the Selenga Delta, Academician Ridge and the major rivers.

1.2.1 Upper layer dynamics and diatom motions

Many different species of diatoms live in Lake Baikal, some of which occur nowhere else in the world. The abundance of these plankton means that they are a major part of the food chain. They are either single cells or filaments, formed by cells remaining attached after division. They have no means of propelling themselves and, therefore, will sink at a rate of about 1 m day^{-1}, but in Baikal the large cells have been reported to sink at up to 3 m day^{-1} (Votinsev and Popovskaya, 1964). It can be seen that in order to maintain a population near the surface of the lake (in the zone of light penetration), some other means of re-suspension is required. This is necessary not only on a daily basis, but also on an annual basis, particularly in the case of the endemic species

which cannot be re-populated from an outside source (e.g. rivers). Some species, which occur mainly in the shallower coastal regions, can be re-suspended from the bottom by wind induced mixing. Those that populate the open water will sink to the bottom, unless they are re-suspended by some mechanism, such as density driven mixing. Only a small percentage need to remain in the top few hundred metres in order for the population to recover in the spring.

Ice cover is an important factor in the diatom life cycle. During March, when the ice is at its thickest, the diatoms begin to reproduce (Skabitchevsky, 1929). This occurs partly due to increasing daylength but is also modified by snow on the surface of the ice which melts or is driven away by winds, allowing solar radiation to penetrate beneath the ice to the upper layer of the water. Decreases in the solar radiation levels, caused either by snow cover or simply by nightfall (diurnal variation) have a considerable effect on the variation of diatom depth distribution over 24 hours. Lower light levels result in a 'drop-out' of diatoms, most likely due to the absence of the heat required to generate the convection needed to keep the particles suspended in the surface layers. This is illustrated well in Figure 1.2 (Jewson, personal correspondence), which shows diatom concentrations and temperature profiles for mid-March 1994. The concentrations beneath snow-covered ice are of the order of ten times lower than for a snow-free ice region. The temperature profile in Figure 1.2a is much more stratified than in Figure 1.2b, which has a mixed region indicated by an isotropic temperature profile (0 - 40 m depth). On a longer timescale, it has been observed that in certain years the lake has remained snow-covered for longer periods, resulting in a reduction in overall diatom population, compared to years with more typical snow cover (Jewson, personal correspondence). Determining the factors that influence the diatom suspension is important if we are to be able to predict and understand changes in their population levels.

In addition to vertical mixing, the horizontal movement of diatoms is also an important consideration. Strong under-ice currents (up to 0.1 m s^{-1}) can occur, and are thought to be driven by density gradients due to differential heating between regions of snow-covered and snow-free ice. Residual currents due to river inflow die away after a few weeks of total ice-cover and, therefore, are not thought to contribute significantly to the under-ice currents (Granin, personal correspondence).

The hydrodynamics of the upper 200-300 m of the lake are investigated here, using a combination of satellite data and numerical modelling. These techniques are described briefly in sections 1.3 and 1.4 below.

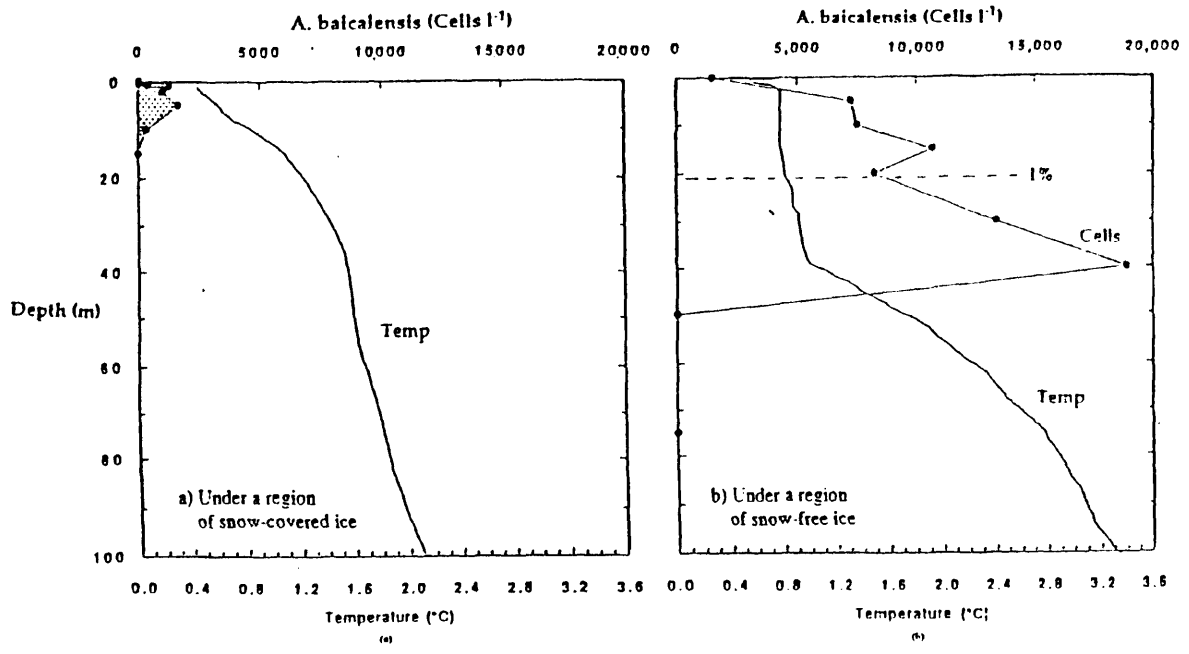

Figure 1.2: Diatom concentrations for March 1994 a) under snow-covered ice (10 cm), b) under snow-free ice. The highest concentrations occur under snow-free ice, where the temperature is uniform with depth. (Jewson and Granin, personal correspondence)

1.2.2 Deep water processes

Fresh water at atmospheric pressure reaches its maximum density at a temperature of 4°C (T_{md}). Temperate lakes with a depth less than about 300 m experience a 'turnover' twice yearly as the surface temperature passes through T_{md}. For example, in autumn as the surface water cools to 4°C, the density becomes greater than that of the water below and convection occurs, displacing bottom waters. This deep water formation by convective processes cannot occur in Lake Baikal, however, due to its great depth and low temperature, as explained below.

Direct heating occurs in the top few tens of metres only, due to the absorption of solar radiation (Goldman *et al.*, 1983). In Lake Baikal, convection and wind stresses have only enough energy to be able to mix this water down to a depth of 200-300 m forming the upper, or mixed, layer. The deep layer remains at about 3.3°C throughout the year. As stated above, water at atmospheric pressure reaches its maximum density at a temperature of 4°C (T_{md}) (Eklund, 1963). However, T_{md} depends on pressure, such that it decreases by ~0.021°C bar^{-1} (a decrease of about 0.021°C every 10 m) (Chen and Millero, 1986; Eklund, 1965). At around 200 m there persists a so-called mesothermal temperature maximum (T_{mm}) of 3.5°C (Shimaraev *et al.*, 1993), corresponding to the temperature of maximum density at that depth. In autumn, the upper layer is cooled by wind mixing and heat loss to below 4°C. Figure 1.4a is an example of a typical temperature profile, showing a cool upper layer overlying a slightly warmer and denser deep layer, with a region at T_{mm} between. Figure 1.4b is an example of a temperature profile for summer, showing a warm upper layer above a denser deep layer. Both situations are stably stratified; free convection cannot take place between the upper and lower layers due to the

mesothermal maximum region lying at T_{md} (Shimaraev *et al.*, 1994). Surface water is unable to convect freely to the deep layer; hence the concentration of oxygen at great depths would be expected to be very low, as in Lake Malawi for example. Measurements of oxygen levels in Lake Baikal (Weiss *et al.*, 1991), using CFCs as tracers, show that this is not the case. Oxygen and temperature profiles indicate an injection of slightly cooler, oxygenated water into the bottom few tens of metres of the lake. From the description of the lake stratification above it can be seen that, to account for the relatively high oxygen concentration, there must be a process at work in addition to free convection.

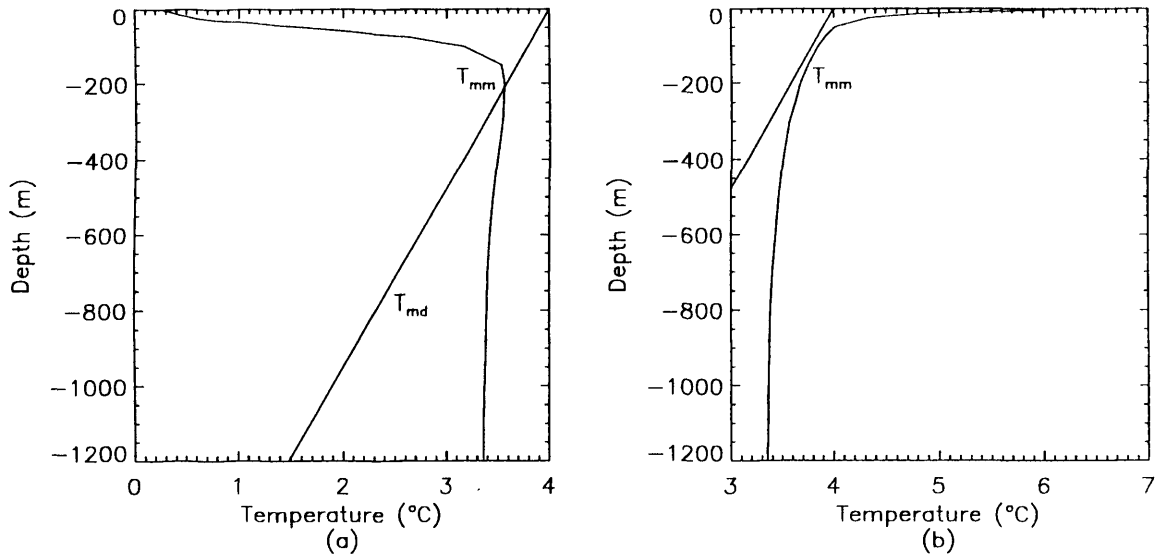

Figure 1.3: Typical temperature profiles for Lake Baikal in a) March and b) July. The mesothermal temperature maximum (T_{mm}) can be seen as a 'knee' in the profile, occurring at a depth of about 200 m, where the temperature crosses the line of maximum density (T_{md}) at about 3.5°C (Shimaraev *et al.*, 1994).

Weiss *et al.* (1991) describe a process which they refer to as a 'thermobaric instability' - that is, one which occurs due to the interdependence of temperature and pressure. Consider the simplified situation depicted in Figure 1.6, of a stable, reversely stratified lake ($\rho_1 < \rho_2$). T_{md} decreases with depth (pressure) as described above. Therefore, if the interface is depressed (by some external mechanism) to a depth (sometimes referred to as the compensation depth, H_c) such that ρ_1 and ρ_2 are equidistant from ρ_{max}, the situation becomes neutrally stable. If the interface deepens further, until T_1 lies on the T_{md} curve, water at the base of the upper layer will be able to displace deeper water, which now lies further from the T_{md} curve. In effect, a plume of cold water develops between the base of the mixed layer and the bottom (or at some other depth if the plume encounters water nearer the T_{md} curve). Shimaraev *et al.* (1993) observed the formation of such a jet in the region of a thermal bar during spring. Carmack and Weiss (1991) briefly describe another possible mechanism for the initiation of such an instability. They propose that during autumn-winter, when the lake is reversely stratified (as in Figure 1.6), surface wind stresses

generate internal waves on the interface between the upper and lower layers. These waves are baroclinic in nature - that is, they depend on changes in density. Since the difference in density between the two layers is small, the amplitude of the waves can be large (many metres). If the waves have an amplitude such that the interface is depressed below the compensation depth, a thermobaric instability could be formed, thus generating a region of local deep convection. The conditions that could give rise to this process (i.e. the generation of internal waves) will be investigated using numerical modelling in Chapter 5.

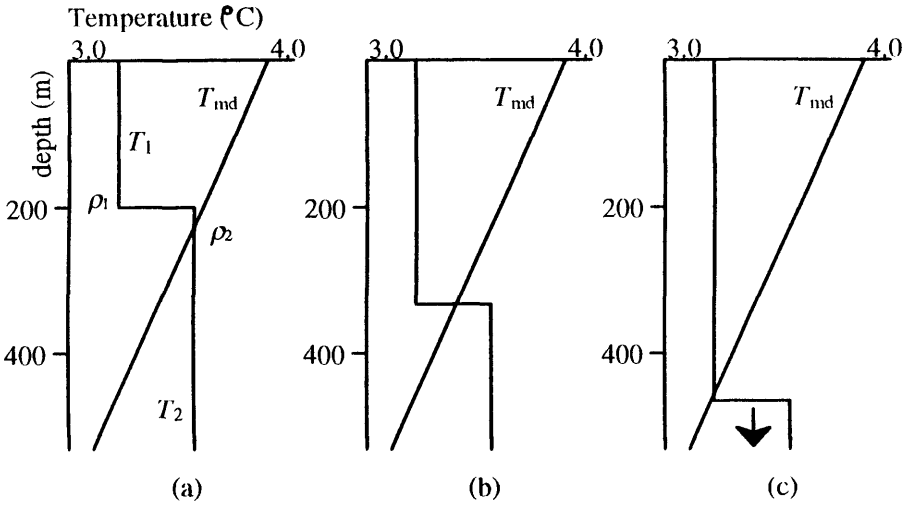

Figure 1.4: Illustration of the formation of a thermobaric instability. The upper layer and lower layers have temperatures T_1 and T_2 respectively. The densities of each layer immediately above and below the interface are ρ_1 and ρ_2 respectively. In (a) the situation is stable, as the upper layer is less dense than the lower. In (b), the interface has been depressed by some mechanism, such that the densities of the two layers above and below the interface are equal, resulting in a neutrally stable situation. Any further deepening of the interface will therefore cause the upper layer to become denser than the lower, resulting in a convective mixing event (c). (After Weiss *et al.* (1991))

Shimaraev *et al.* (1993) discussed thermal bars as a mechanism for deep ventilation. These long lived thermal and density fronts usually occur in temperate lakes during spring warming and autumn cooling. During the Lake Baikal spring (May-June) a front separates two regions of waters; one directly stratified, close to the shore (where the shallower water results in increased heating), with temperatures greater than T_{md}; the other, inversely stratified open water with temperatures less than T_{md}. In this open lake region, the surface of the lake is at a temperature of about 3°C. This increases with depth to T_{mm} at about 200 m, and then gradually decreases again. In the region of the thermal bar the mesothermal maximum has been observed to disappear during June, resulting in homothermy at 3.35°C between the hypolimnion (the deep layer below the thermocline) on the open lake side of the bar, down to the bottom of the lake. This temperature is lower than that of the surrounding water, and so a jet of cold water is formed which then travels along the bottom slope of the lake. Thus near-surface, oxygen-rich water is able to penetrate to great depths. Increased salinity in the coastal waters (due, for example, to dissolved salts in river

inflow), may be sufficient to increase the density of the surface water such that it is able to penetrate the T_{mm} region and sink to greater depths. This could be coupled with the thermobaric instability event described above. The formation of spring thermal bars will be investigated in Chapter 2, using satellite data.

1.3 Remote sensing from satellites

Remote sensing from satellites is a very useful tool in the study of oceans and large lakes. The relatively high frequency of overpasses and the large spatial coverage allow surface characteristics, such as temperature and reflectance, to be monitored on an almost continuous basis over a long period of time. *In situ* measurement campaigns are costly and are able to cover only very small regions at a time. They also have the disadvantage of inconsistencies in measuring instruments and techniques. For example, bulk sea temperature can be measured by taking buckets of water from over the side of a boat, or from sensors mounted on the hull, or from floating buoys. Each of these techniques could conceivably give different results even for the same region of water. Remote sensing, although unable to replace *in situ* measurements entirely due to the necessity of validation campaigns, can be a low-cost alternative in many cases, providing continuous, reliable data, available to a wide community of users.

The particular type of satellite data used in this study was chosen to meet the requirements of the problem under consideration. Thermal wavelength data (10-12 μm) are required in order to observe surface temperature features, which provide information about underlying physical processes. Visible wavelength data (0.55-0.87 μm) are important for detecting snow and ice on the surface of the lake. Spatial resolution is another factor to consider. Although very high resolution data (such as from Landsat) provides detailed information about small scale features, this level of detail is not required for this study, and is in fact undesirable. Obtaining such data for an area as large as Lake Baikal, and for many different dates, would be unfeasible in terms of data acquisition cost and storage space. An instrument is, therefore, chosen which has a resolution sufficient to show the features being investigated, at the required wavelengths. For this study, data from the Along Track Scanning Radiometer (ATSR) satellite instruments are used; both thermal and (in the case of ATSR-2) visible wavelength data are available, at a spatial resolution of 1 km. Section 1.3.3 gives more details of the ATSR instruments.

1.3.1 Principles of thermal remote sensing

All objects emit electromagnetic radiation at a rate according to the temperature of the object. This rate is modified by the emissivity of the object, a value between zero and unity which depends on the surface property. An object with an emissivity of unity emits thermally at the maximum possible rate (dependent only on temperature), and is known as a 'blackbody'. Although most objects have an emissivity less than one, some can be approximated to a blackbody; the Sun is one example. The spectral emittance of a blackbody at temperature T is dependent on wavelength and is given by Planck's radiation law (Eq. 1.1):

Eq. 1.1 $$B_\lambda = \frac{2hc^2}{\lambda^5}\left(\exp\left[{}^{hc}/_{kT\lambda}\right]-1\right)^{-1}$$

In order to measure an object's temperature, an instrument called a radiometer can be used, which utilises this relationship between emitted thermal radiation and temperature. The emitted radiation at different wavelengths is measured, from which a so-called Brightness Temperature (BT) can be derived using Planck's law. Atmospheric transmission is high between about 11 and 12 μm (see Figure 1.7), so these two wavelengths are commonly used by thermal remote sensing radiometers. Other atmospheric windows at 1.6 and 3.7 μm are used for measuring reflected and emitted thermal radiation respectively.

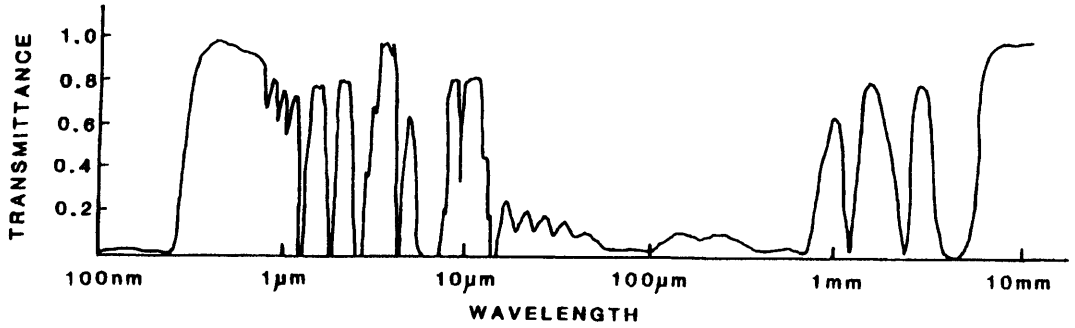

Figure 1.5: Atmospheric transmission, showing the wavelengths at which high transmittance occurs.

In situ measurements of water temperature tend to refer to the 'bulk', somewhere between a depth of a few centimetres to a few metres. However, BTs are skin temperatures, that is, the temperature of the top 100 μm of the water (Figure 1.8). Skin temperature is usually cooler than bulk temperature, due to the vertical heat flux through the sea-air interface. The difference in temperature between the two (δt) varies considerably depending on the local conditions, but is typically around 0.1 - 0.5 K. The bulk-skin difference reduces almost to zero when the sea-state is rough (strong mixing) and solar heating is low.

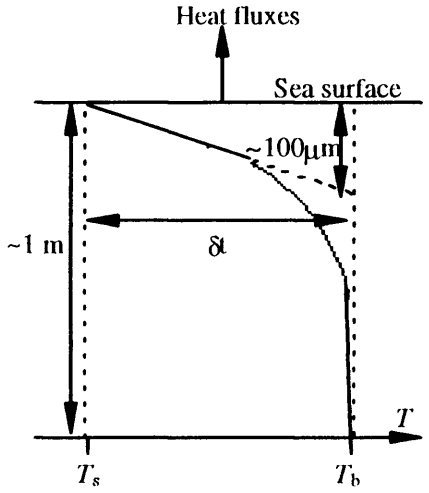

Figure 1.6: Bulk and Skin temperatures, T_b and T_s. The bulk-skin temperature difference, δt, can be up to 1-2 K.

1.3.2 Cloud detection

One of the problems with thermal and visible wavelength remote sensing is that cloud cover obscures the view of the surface, resulting in a potential loss of continuity. It is clearly very important to be able to identify cloud in satellite data, to prevent contamination of surface data. One of the simplest methods for identifying certain types of cloud is by utilising the fact that the BT of the tops of high clouds tend to be cold in comparison to the surface. Pixels with BTs colder than about 273K are likely to be cloud, although this will not always be the case. This is particularly true in cold regions, and where the cloud is very thin or patchy (e.g. small clouds which cover only a fraction of each 1 km^2 pixel), resulting in the contribution of surface radiation to the total amount detected. Much more sophisticated cloud tests have been developed, including one which utilises the relatively high reflectivity of clouds in the 1.6 μm channel compared with that of water.

1.3.3 An overview of the ATSR instruments

The Along Track Scanning Radiometer (ATSR) series of instruments were designed with the primary objective of detecting small changes in global temperature which may be indicative of global warming. A continuous dataset over a period of more than ten years will be available, with a period of overlap between each of the missions for inter-comparison and validation. Mission details are shown in Table 1.1 below.

Table 1.1: Mission details for the ATSR series of instruments

Instrument	Satellite	Launch date	Status
ATSR-1	ERS-1	July 1991	Dormant (from 1996)
ATSR-2	ERS-2	April 1995	Active
AATSR (Advanced ATSR)	ENVISAT	1999	-

The instruments detect thermal, and, in the case of ATSR-2 (and AATSR in the future), visible radiation. All the ATSR instruments detect radiation at three thermal infra-red wavelengths (3.7, 11 and 12 μm) and one reflected infra-red wavelength (1.6 μm). In addition to these channels, ATSR-2 has three visible bands at 0.865, 0.659 and 0.555 μm. Images representing brightness temperatures are obtained from the thermal bands. BT images are useful for the analysis of surface thermal features when only the *relative* temperatures are required, as BTs may be up to 2°C cooler that the actual temperature (as discussed in section 1.3.1 above). In order to derive accurate, absolute, sea (or more generally, water) surface temperatures (SSTs), the ATSR instruments observe each scene at two angles, approximately 55° and 0° to the nadir (See Figure 1.7). This dual-angle viewing geometry allows each scene to be viewed through two different atmospheric path lengths, which, in conjunction with measurements at up to three different wavelengths, enables accurate atmospheric corrections to be made. In order to achieve the objective of detecting signs of global warming, SSTs must have an absolute accuracy of 0.3°C and a relative accuracy of 0.1°C (Edwards *et al.*, 1990). The spatial resolution of ATSR is 1 km and each image covers an area of 512 x 512 km. During the mission a combination of 3 and 35 day repeat cycles has been used, the former during the commissioning phases only. During the 35-day repeat cycle, two overpasses of approximately the same region are made every three days - one during the day and one at night. The field-of-view returns to the same 512 x 512 km scene every 35 days. Since the mission started in 1991, there have been many hundreds of observations of Lake Baikal. Cloud cover will, of course, reduce the number of images suitable for surface temperature analysis, but the high spatial and temporal resolution of the instrument still makes it an ideal tool for observing large scale surface features. *In situ* measurements on this scale would be highly impractical, if not impossible, over such long time periods.

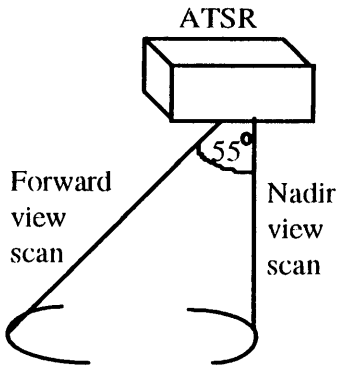

Figure 1.7: ATSR viewing geometry. The ATSR instruments scan along two arcs swept out by a cone, in the nadir direction and forward at an angle of 55° to the nadir. (Mutlow *et al.*, 1994)

1.4 Numerical modelling

In order to understand the hydrodynamics of Lake Baikal, the technique of numerical modelling is used. At its basic level, a model solves the equations describing conservation of mass, momentum and thermal energy for the system being studied. The model starts with a given set of initial conditions (such as the shape and size of the system, initial temperature and the spatial and temporal resolution at which to solve the equations), and integrates over time and space. In this way, the model acts as a laboratory in which the theoretical behaviour of the system can be examined for different conditions. In the case of Lake Baikal, one of the factors under consideration is the effect of variations in snow and ice cover on current flow and the development of the temperature profile, in relation to diatom distribution, as described in section 1.1.

One important use of satellite data is in conjunction with numerical models, whether it is on a global scale for predicting global climate change or weather forecasting, or on the smaller scale studied here. In order to provide realistic input of snow and ice cover to the model, satellite data from ATSR-2 is used, as described in Chapter 3. It is also used for the qualitative validation of the model, in conjunction with both recent and long term *in situ* observations of temperature.

Two types of model are developed and used here: the first, a barotropic model, to investigate principally the factors influencing gyre formation; the second, a baroclinic model, to study the hydrodynamics of the top few hundred metres of the lake, with particular emphasis on the period of ice-cover, and on the conditions necessary to generate a thermobaric instability. The two model types indicate the different wave modes that are resolved by the model. Waves occur on interfaces between layers of differing densities. The smaller the density difference, the greater the wave amplitude and period. Thus, on a water-air interface the waves have a small amplitude and a fast speed. This is known as the barotropic mode. Waves on internal interfaces between layers of different temperatures (and hence densities) are much slower, and larger in amplitude, due to the relatively small density differences. These are the baroclinic wave modes.

The barotropic model solves equations relating to pressure gradients caused by changes in surface height. The model consists of a single layer only, and since no density variations are included, only the short time-scale barotropic motions are resolved. Pressure gradients arise due to applied wind stresses on the surface, and changes in surface height at river inflows and outflows. The model output generated consists of the surface height and horizontal velocities representing the current flow caused by the surface displacements. Results from this model and a further discussion of the techniques involved are given in Chapter 4.

In addition to the barotropic mode, the baroclinic model[1] also solves equations which govern temperature (and hence density). The model, described in Chapter 5, is the first step towards a multi-layer general circulation model. The number of layers, N, is limited only by considerations of the computation time required by more layers. Pressure gradients arise due to gravity acting on changes in density (caused by surface heating) and from applied wind stresses.

A wide variety of models have been discussed in open literature. For example, a number of models are one-dimensional in the vertical (Patterson and Hamblin, 1988), or two-dimensional in the horizontal and vertical (Killworth *et al.*, 1996). Walker and Watts (1995) describe a non-hydrostatic three-dimensional model of a temperate lake and its use to study deep ventilation in Lake Baikal. Kelley (1997) uses analytical methods and Monte Carlo simulations to model two-dimensional steady circulation flow fields, in order to study algal suspension.

The baroclinic model which has been chosen to be developed for this study is an intermediate level model of the tropical Pacific Ocean, which has been in use for more than ten years (McCreary and Anderson, 1983; McCreary and Anderson, 1991). This model was chosen because it was thought to be the most suitable for representing the processes under investigation. It would allow a three-dimensional investigation of temperature and current flow, on the required timescales of days to months necessary to study mixing processes. Enhancements to the original model include: conversion to a fresh-water equation of state; an increase from two to N layers; inclusion of the barotropic mode alongside the baroclinic mode; and a scheme to model convective mixing. Further details of this model are given in Chapter 5. The relative merits of these models, in relation to the results of this research, are discussed in Chapter 6.

[1] Although this model is referred to as a baroclinic model, it resolves both the baroclinic and barotropic wave modes.

2. Observations of physical processes using satellite data

2.1 Overview

Satellite data is an important tool with which to study the physical processes in lakes with large surface areas (i.e. much greater than the spatial resolution of the satellite data), such as Lake Baikal (Bolgrien and Brooks, 1992; Malm and Jonsson, 1994). Thermal and visible wavelength satellite data provides direct information about the surface of the lake, which can then be used to determine details of dynamical processes within the lake. For example, 'thermal bars' play an important part in mixing and deep water renewal processes within the lake (Shimaraev *et al.*, 1993), and can also be clearly observed as a surface feature with thermal satellite data (Bolgrien *et al.*, 1995).

Section 2.2 describes thermal bars in more detail, and their observation using thermal wavelength satellite data from the ATSR instrument. Temperature transects and histogram analysis are used to produce time series of plots showing the development of thermal bars during the spring warming period. In section 2.3, observations of gyres are presented, and their potential role in deep water ventilation discussed. Sections 2.4 and 2.5 describe observations of coastal upwelling and suspended sediment plumes respectively.

2.2 Thermal bars

Dimictic lakes are defined as those that have a temperature stratification which is direct in the Summer and inverse in Winter, as shown in Figure 2.1. During Spring (Autumn) warming (cooling) the temperature therefore passes through the temperature of maximum density, T_{md} (4°C at the surface), resulting in convective overturn (Zilitinkevich *et al.*, 1992; Farrow, 1995).

Lake Baikal is a dimictic lake, although complete convective overturn does not occur, due to its great depth (for the reasons discussed in Chapter 1). A feature associated with this overturn, which occurs in Lake Baikal and other dimictic lakes, is the thermal bar (Figure 2.2). During the early stages of Spring warming the entire lake is homothermal at 3-4°C (Figure 2.1b). In the shallower coastal regions warming continues quickly, the water column becoming stably stratified with temperatures considerably greater than T_{md}, while the rest of the lake remains just below it.

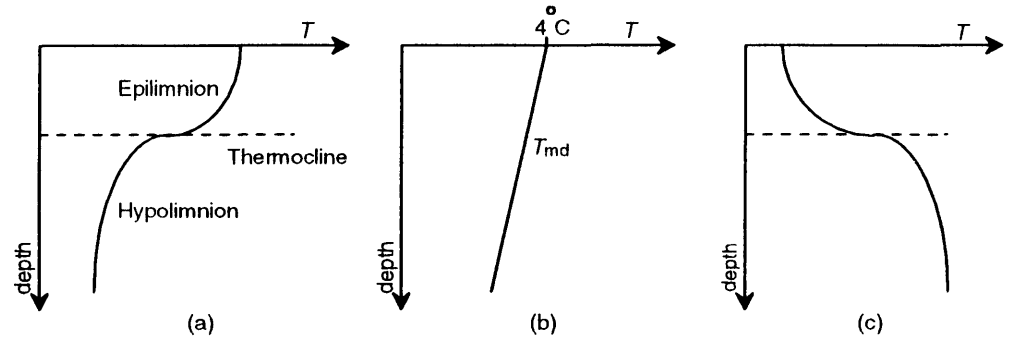

Figure 2.1: **Illustration of temperature stratification in a dimictic lake: (a) direct stratification in summer (warmer water overlying cooler, denser, water); (b) neutral stratification in spring/autumn; (c) indirect stratification in winter (cooler water overlying warmer, denser, water). The thermocline is the region of greatest temperature gradient, which separates the epilimnion (upper layer) from the hypolimnion (denser, lower layer).**

Separating these two regions, where the water column is neutrally stable at T_{md}, is a thermal and density front where convection can take place freely. This region, known as a 'thermal bar', gradually moves outward from the coast as warming continues.

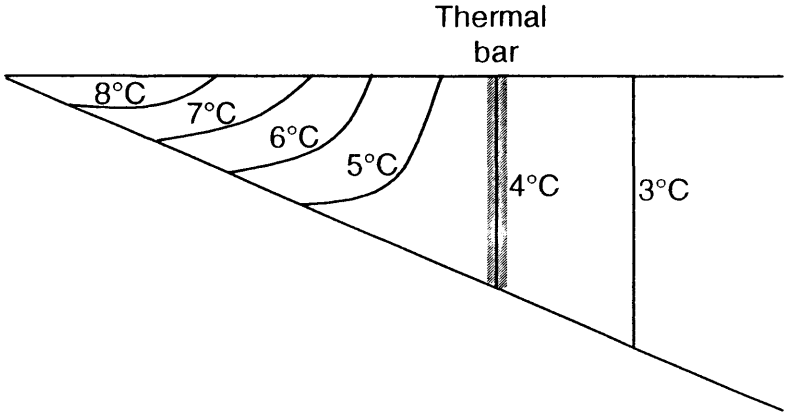

Figure 2.2: **An idealised cross-section of the coastal region of a lake, showing a thermal bar. The shallow coastal water warms more quickly than the open lake water, resulting in the formation of a temperature and density front (thermal bar) in the region where water greater than T_{md} meets water less than T_{md}. (After Malm and Jonsson, 1993)**

Shimaraev *et al.* (1993) discuss the thermal bar as a possible mechanism for deep ventilation of Lake Baikal waters. A cold jet of water on the open-lake side of the bar has been observed, which may be due to thermobaric instability (Weiss *et al.*, 1991; Shimaraev *et al.*, 1993) allowing cold water (3.35°C) to sink to depths as great as 1000-1500 m. The extent and duration of thermal bars is investigated here, using satellite data from the ATSR instrument, in order to provide further insight into their role in the process of deep water ventilation.

2.2.1 Temperature transects

Satellite data of Lake Baikal during the Spring/Summer warming period (June-July) of 1993 and 1995 was examined for the presence of thermal bars. These are evident in the images as a sharp temperature gradient a few kilometres from the coastal regions, particularly around the Selenga Delta. This can clearly be seen in plots of brightness temperature (BT) along a transect. Figure 2.4 is a time series of plots using transect A in the northern part of the Central Basin, between 10th June and 7th July 1993.

Figure 2.5 shows similar plots but for transect B across the Central Basin close to the Selenga Delta, between 4th June and 4th July 1995. Different transects were chosen for the two years in order to maximise the amount of cloud-free data at each location. The four lines shown in each plot represent BT measured in the four thermal channels of ATSR, as discussed in Chapter 1: 12 μm nadir (solid), 11 μm nadir (short dash), 12 μm forward (long dash) and 11 μm forward (dot dash). For simplicity, when specific temperatures are given below, the 12 μm nadir channel BT is used. Note that the number of pixels in the transect varies slightly with each plot, due to the different orientation of the descending (day) and ascending (night) images.

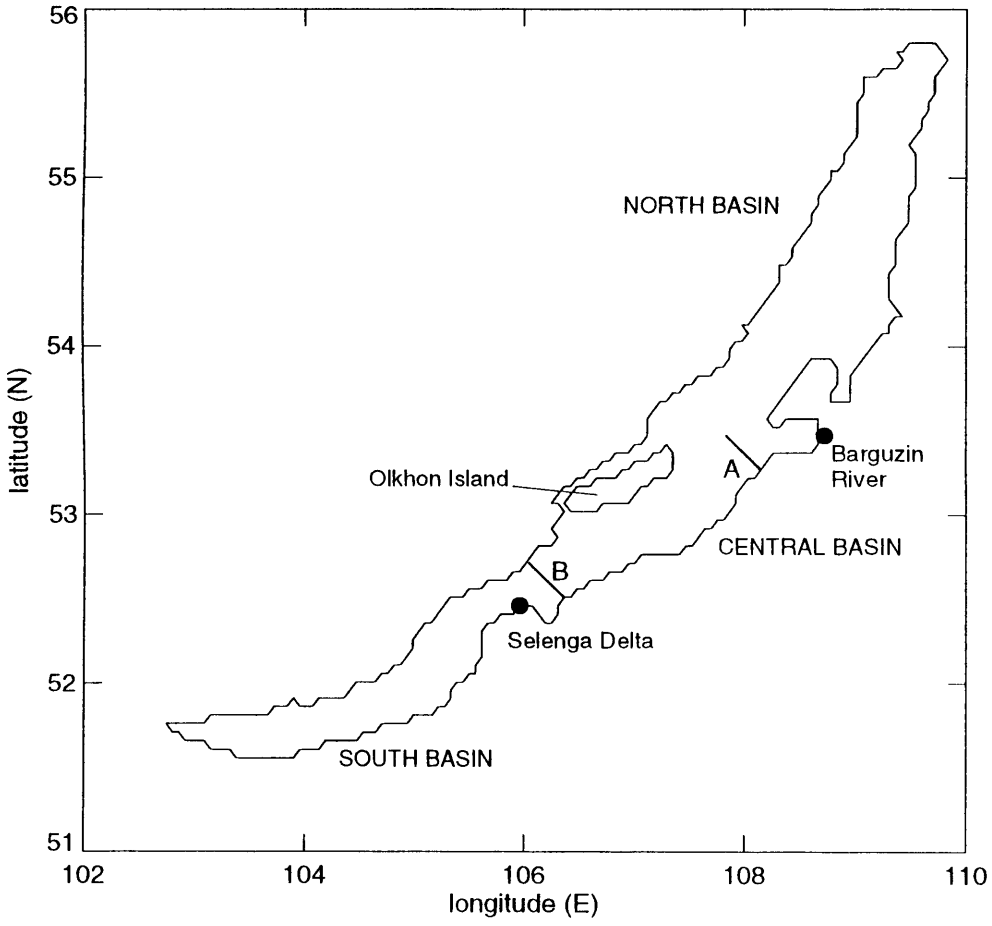

Figure 2.3: Outline of Lake Baikal showing the location of transects A and B in the Central basin.

In Figure 2.4a the temperature across the transect is almost uniform at 276 K. The beginnings of a thermal bar can be seen at the right hand side of the plot (i.e. nearest the south-east coast) where the temperature increases slightly to 277 K. The temperature increase is more noticeable in the forward channels, although this is likely to be due to a slight offset of one kilometre between the nadir and forward channel images, i.e. the forward transects should be shifted one pixel to the right to match up with the nadir channels. The plot for 15th June, Figure 2.4b, shows forward channels only as the nadir data was unavailable for this date. The bar is in approximately the same location as five days previously. By 23rd June (Figure 2.4c), the bar has developed considerably, extending by 3 km into the lake. The open-lake region is still a uniform 276 K, while the water nearest the coast (on the right) has reached 283 K. Two days later (Figure 2.4d), the open-lake water has increased slightly to 276.5 K and the thermal bar has spread further, to about 7 or 8 km from the shore. The near-coast water has reached its peak of 285 K. The following day, 26th June (Figure 2.4e), The maximum temperature has decreased slightly to 283 K, while the open-lake region has now warmed to 277 K, the temperature at which water reaches its maximum density. Ten days later, on the 7th July (Figure 2.4f), the surface temperature along the entire transect is greater than 280 K, the highest temperatures still occurring in the innermost 15 km.

During the first sixteen days shown in the plots (Figure 2.4a to e) the temperature in the open-lake region increases by only one degree. In the next sixteen, between Figure 2.4e and Figure 2.4f, it increases by about four degrees. When the temperature is so close to T_{md}, about 276-277 K, vertical mixing is able to occur relatively easily due to the low stability of the water column. Even small increases in temperature cause the water to sink, and be replaced by cooler water from below. This process continues until the entire water column reaches T_{md}, after which further increases in temperature at the surface result in a density decrease, thus causing the water column to become directly stratified, resulting in a relatively rapid increase in surface temperature once it passes T_{md}.

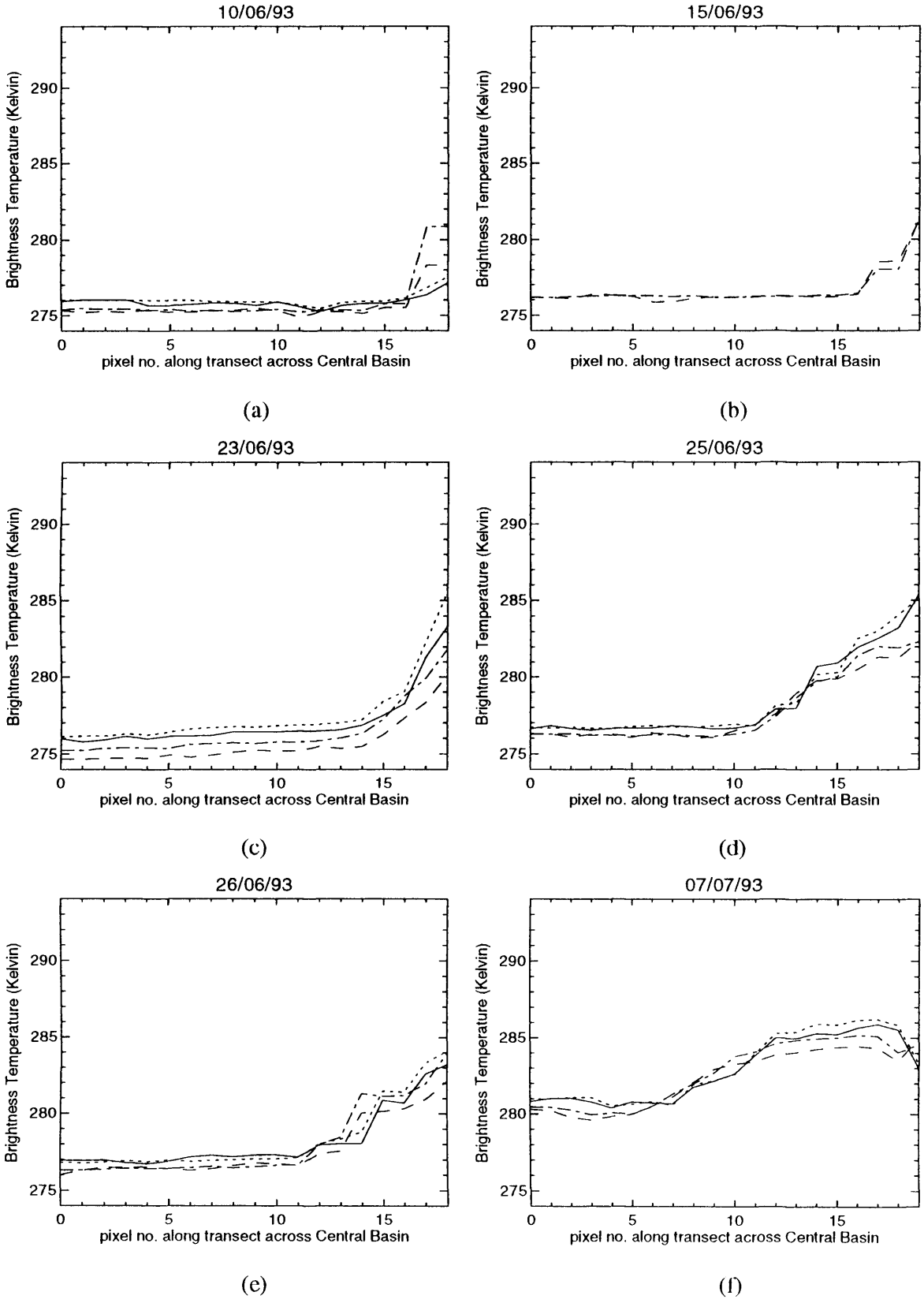

Figure 2.4: Time series of plots from 10/06/93 to 07/07/93 showing brightness temperature along transect A, across the Central Basin, south-west of Barguzin Bay (1 pixel ≈ 1 km). Key: 12μm nadir: solid; 11μm nadir: short dashed; 12μm forward: long dashed; 11μm forward: dot-dashed.

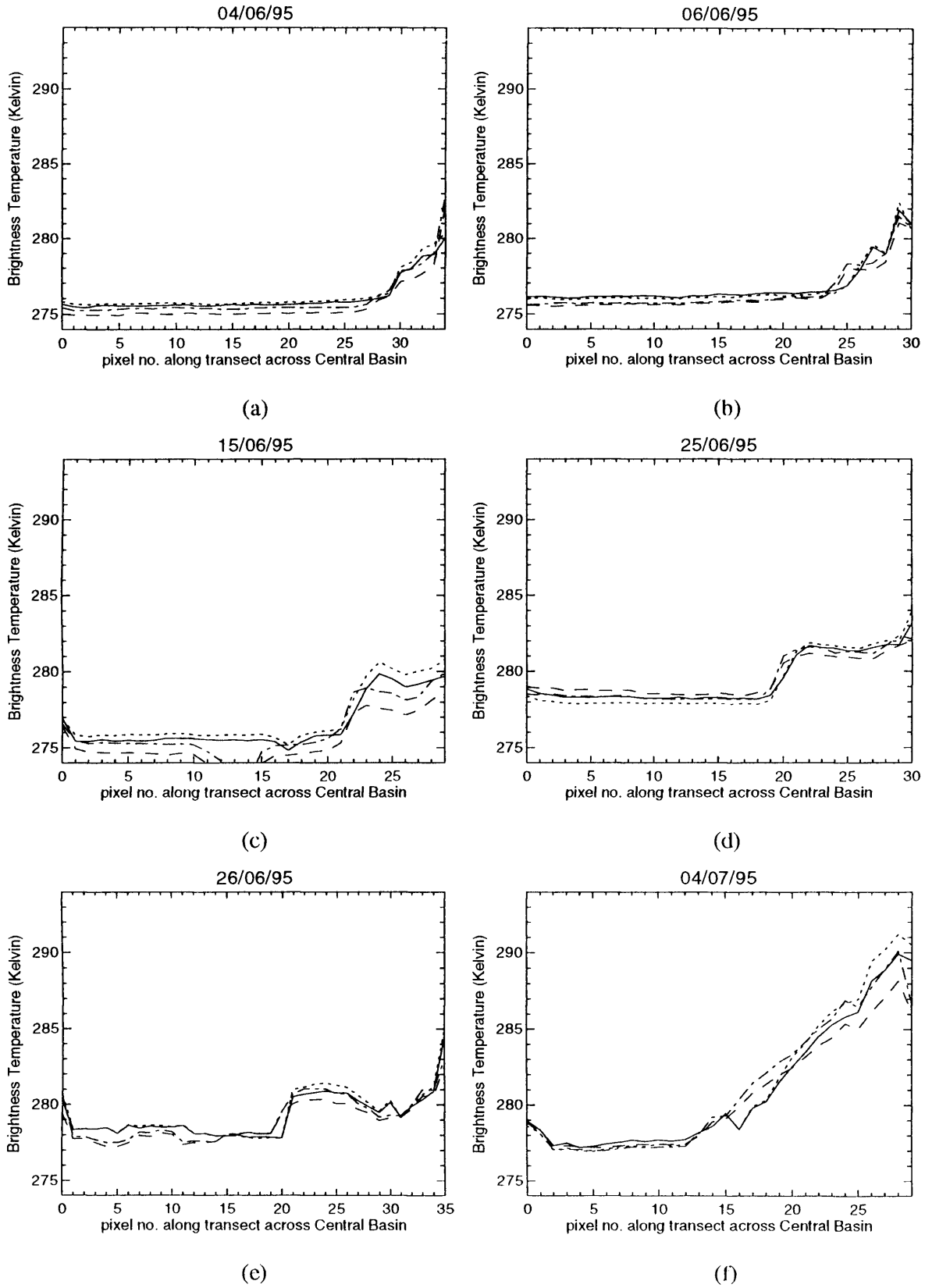

Figure 2.5: Time series of plots from 4/6/95 to 4/7/95 showing Brightness Temperature along transect B, across the Central Basin, north-east of the Selenga Delta (1 pixel ≈ 1 km). Key: 12μm nadir: solid; 11μm nadir: short dashed; 12μm forward: long dashed; 11μm forward: dot-dashed. NB. the variation in pixel no. along transect is due to the different orientation of the descending (day) and ascending (night) images.

Figure 2.5 shows a similar progression of the thermal bar over the period 4th June to 4th July 1995. Transect B, unlike transect A, stretches across the entire width of the Central Basin, from the north-west coast on the left to the south-east coast on the right. The thermal bar is already evident in the 4th June plot (Figure 2.5a), however, suggesting that either initiation of the bar begins earlier nearer the Selenga Delta, or warming of the whole lake began earlier in 1995. The maximum temperature which occurs over the range of dates shown is 290 K on the 4th July (Figure 2.5f), which is warmer by five degrees than the maximum transect A. This could be due to transect B being further south, or its proximity to the Selenga Delta (from which warmer river water flows). Figure 2.5 shows slightly anomalous open-lake temperatures, in that it increases from 275.5 K in Figure 2.5c to 278 K in d and e, and then drops back to 277 K in Figure 2.5f. This is inconsistent with the data from 1993, and may be either a true representation of the surface temperature or an artefact of the surface property. Since the temperatures shown are brightness temperatures, they are dependent on the emissivity of the water. If the emissivity increases, the BT will be apparently higher. Examining the visible wavelength channels of the anomalous dates shows an unusually high level of reflected radiation, which could indicate the presence of diatom blooms (a common occurrence at this time of year). If this were the case, the emissivity would be considerably altered, resulting in the apparent increase in the surface temperature.

2.2.2 Histogram plots

Using a fixed value for T_{md} of 277 K (4°C) to locate the thermal bar is clearly not an ideal method when using BTs, as the value is different for each channel and may vary slightly from day to day depending on surface and atmospheric conditions. Histogram plots of pixel temperature over the lake may be used to determine the BT at which maximum density occurs (BT_{md}). For example, Figure 2.6 and Figure 2.7 below are time series of histograms using the 11 μm nadir BT for the dates used in the transect plots above. The well defined peaks around 276 K are due to the uniform temperature of the open-lake. Above T_{md} a much wider spread of temperatures is possible, as can be seen in the histograms. Between the two regions lies the thermal bar, the temperature of which (i.e. BT_{md}) can be found where the sharp peak drops off and the spread of warmer pixels begins. For example, in Figure 2.6a this occurs at 276.5 K. Table 2.1 gives values of BT_{md} obtained from Figure 2.6 and Figure 2.7. Note the two degree shift in the large peak for 25th and 26th June 1995, and the correspondingly high values of BT_{md}, as seen in the transect plots in the previous section.

Table 2.1: BT_{md} values obtained from Figure 2.6 and Figure 2.7 (11 μm nadir channel data)

Date	10/06/93	15/06/93	23/06/93	25/06/93	26/06/93	07/07/93
BT_{md} (K)	276.50	276.75	276.50	276.75	277.25	277.00
Date	04/06/95	06/06/95	15/06/95	25/06/95	26/06/95	04/07/95
BT_{md} (K)	276.6	277.2	276.5	278.8	278.5	277.5

Using these values for BT_{md} as threshold values, plots can be derived from satellite images showing the extent of the thermal bars. Figure 2.8 and Figure 2.9 are plots for Lake Baikal for the dates used in the transect and histogram analyses, derived using the 11μm nadir BT image and the BT_{md} threshold values given in Table 2.1 above. In each image white represents both land and any cloud which may be present. Lake pixels with a temperature less than the BT_{md} for that date are shown in grey, and those warmer are shown in black. The different orientations of the lake are due to the type of satellite overpass - descending (day) overpasses are more 'vertical' than ascending (night) overpasses.

It is clear from Figure 2.8 and Figure 2.9 that thermal bars occur primarily along the south-east coast, in particular around the Selenga Delta and at the far end of the North Basin. The location of the bar in the plots for 1993 is further out from the shore than at a similar time in 1995. The thermal bars tend to be fairly restricted to the coastal regions and extend out from the coast by only a few kilometres in most cases. As the transect plots in Figure 2.4 and Figure 2.5 suggested, it appears that the lake does not achieve direct stratification by a steady inward progression of the thermal bars, as occurs in many dimictic lakes (Goldman and Horne, 1983), but rather by gradual heating of the bulk of the open-lake water.

While the images do clearly show thermal bars, cloud cover is extensive, particularly at the end of June and beginning of July (hence the lack of images shown for this period), restricting the amount of quantitative information which can be obtained. Also apparent in these figures is the sometimes rather poor spatial coverage of the lake. The ascending passes (e.g. Figure 2.8b, d and f), having a swath width of 512 km, result in parts of the lake being missed. (Data covering the southern lake for the descending passes was also examined, but is not shown here.)

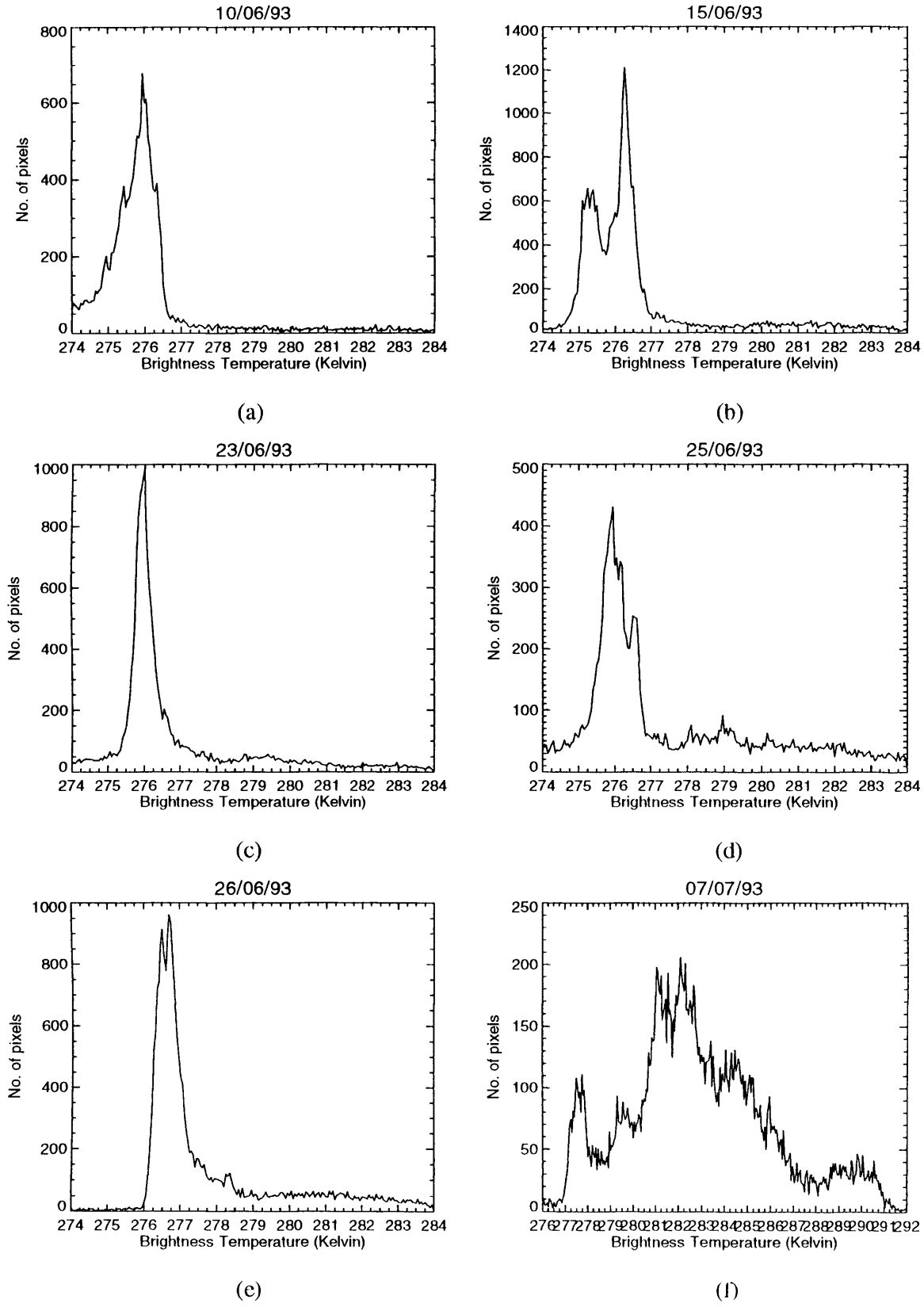

Figure 2.6: Time series plots for 10/06/93 to 07/07/93 showing histogram plots of 11μm Brightness Temperature for lake pixels.

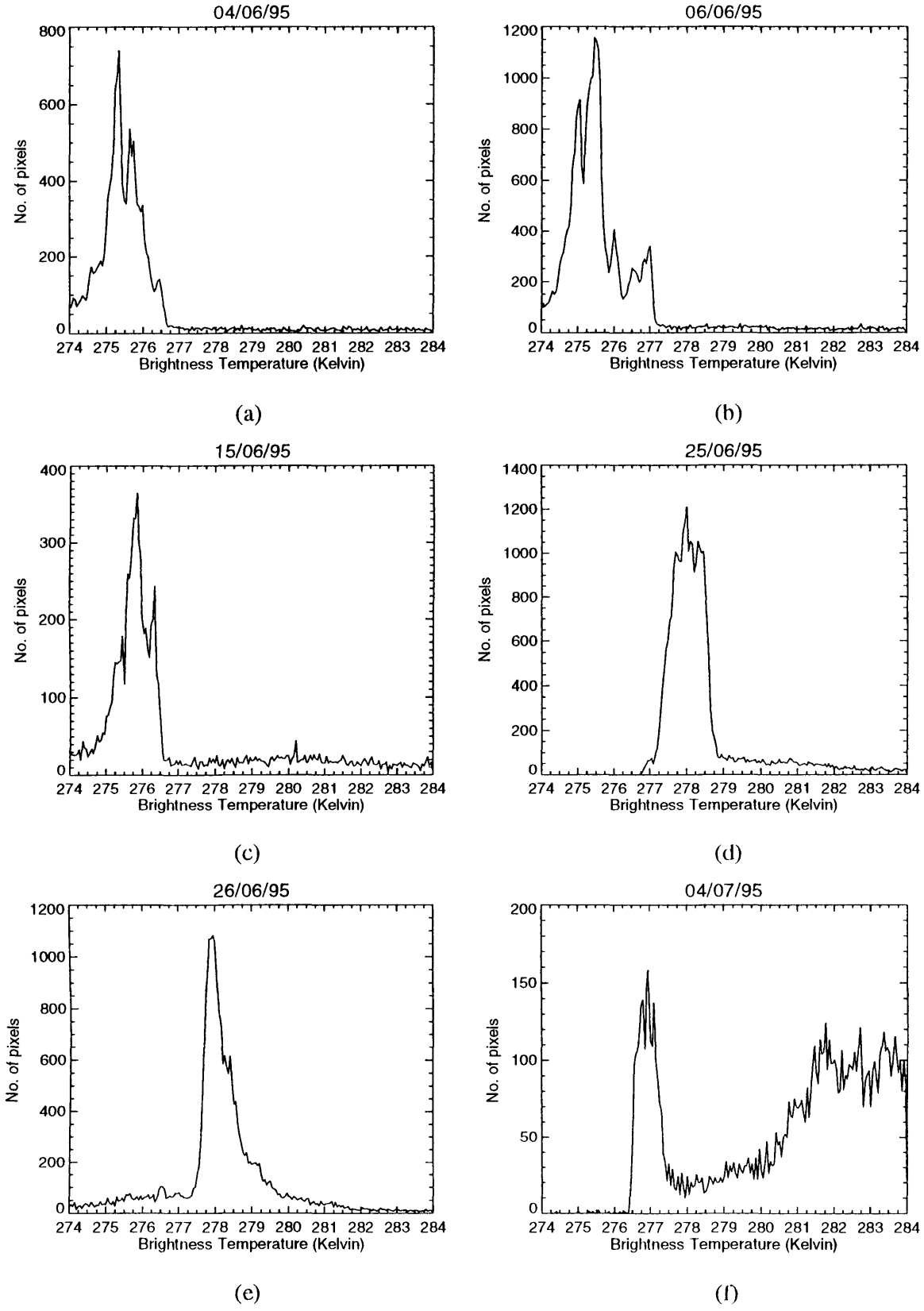

Figure 2.7: Time series plots for 4/6/95 to 4/7/95 showing histogram plots of 11 μm Brightness Temperature for lake pixels.

Figure 2.8: **Plots derived from satellite images using histogram plots to show the location of the thermal bars from 10/06/93 to 07/07/93. Water warmer than T_{md} is shown in black, water cooler than T_{md} is shown in grey, and land (and cloud) is shown in white.**

Figure 2.9: **Plots derived from satellite images using histogram plots to show the location of the thermal bars from 4/6/95 to 4/7/95. Water warmer than T_{md} is shown in black, water cooler than T_{md} is shown in grey, and land (and cloud) is shown in white.**

2.3 Gyres

Figure 2.12 shows a time series of satellite images for 18th to 22nd October 1994. The warm (281 K) circular feature in the region of the Academician Ridge (see Figure 1.1) appears to be a gyre, or large eddy structure, and persists from at least mid-October[1] to mid-November, when the satellite data shows that it has dispersed. A similar but smaller feature is also visible half way along the north-west coast of the North Basin.

Satellite images from 1991 also show an almost identical structure at the same time and location, although due to extensive cloud cover it is only clearly visible on images between 17th and 21st October. Data from autumn 1993 do not indicate the presence of gyres, but the number of cloud-free images is again small for this period of time, so the possibility of gyre formation in 1993 should not be ruled out. A more open spiral feature is, however, present in data for 17th July 1993 (Figure 2.13).

Other images (e.g. 25th August 1992 and 21st August 1993) suggest that warm coastal waters flow around Svyatoi Nos Peninsular (see Figure 1.1) and are turned in a north-easterly direction, sometimes forming a spiral structure in the region between the peninsular and the Academician Ridge.

Gyres in Lake Baikal always occur in the same location, between Svyatoi Nos Peninsular and Academician Ridge. This strongly suggests that major factors in their formation are interaction between coastal currents and lake topography, rather than just Coriolis forcing as occurs in the open ocean. Proximity to the Barguzin River suggests that river inflow could also be a significant influence. The most well developed gyres tend to form in October and November, when the region is subjected to severe storms with north-westerly winds reaching speeds of up to 40 m s^{-1}. Such strong winds are likely to have a considerable impact on current flow, and may be another factor in the formation of gyres in Lake Baikal.

Eddies may be formed from spits of land, as in Figure 2.10. When friction with the land generates current shear this results in the water acquiring relative vorticity. In the case of the Lake Baikal gyre (and that in Figure 2.10) this vorticity is negative, or clockwise. If some other factor, such as the wind, causes the water to gain vorticity in the opposite direction (positive, or anti-clockwise), this may cancel out the negative vorticity so that no rotational motion occurs. Alternatively, the action of the wind could add to the vorticity of the water, resulting in the formation of a gyre, when otherwise it would not be sufficient.

[1] Earlier images are either cloudy or not available

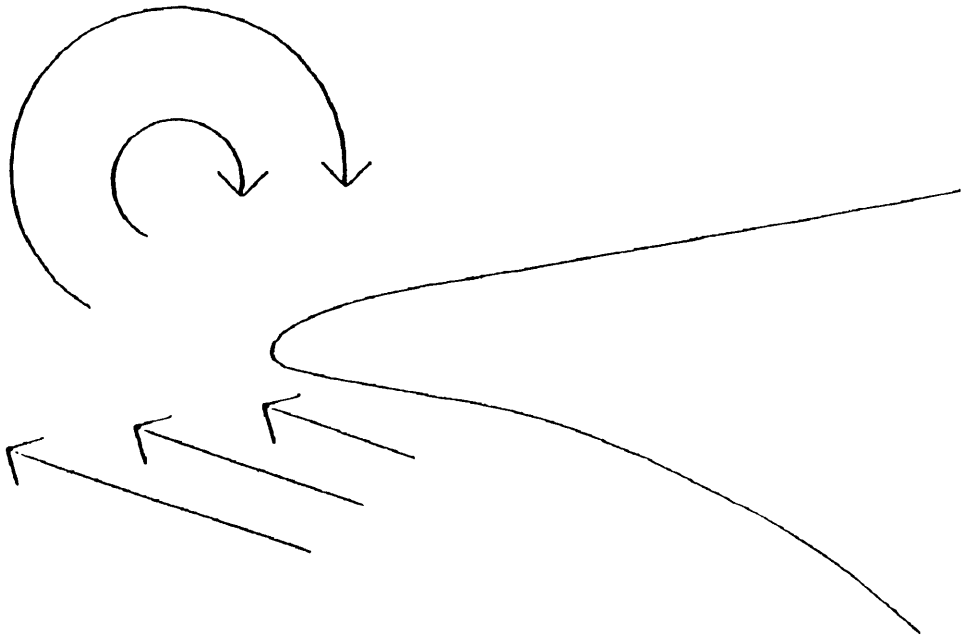

Figure 2.10: Gyre formation off a promontory such as Svyatoi Nos Peninsular. In the situation above, friction with the land causes the water to gain negative vorticity, resulting in a clockwise spiral, or gyre. (After Bearman, 1989)

One of the interesting aspects of gyres is as a possible mechanism for the ventilation of deep waters. In order for this to occur, downwelling of surface waters must take place. From the satellite images the water appears to be spiralling in a clockwise direction towards the centre of the gyre. Therefore, extra mass is being added to the centre of the gyre and the only way in which this can be removed is for there to be a downward flow. The temperature of the upper layer of the lake at this time of year, when gyres tend to be observed, is too high (about 8°C) for deep water ventilation to occur by this method alone, as the density of the surface water will be too low for it to sink very far. However, an increase in the salinity of the water in the gyre, injected by river inflow (e.g. from the Barguzin), may increase the density sufficiently for this process to occur.

The processes which lead to gyre formation will be investigated further in Chapter 4, using numerical modelling techniques. However, it will be seen that lack of detailed wind data prevents quantitative conclusions being drawn.

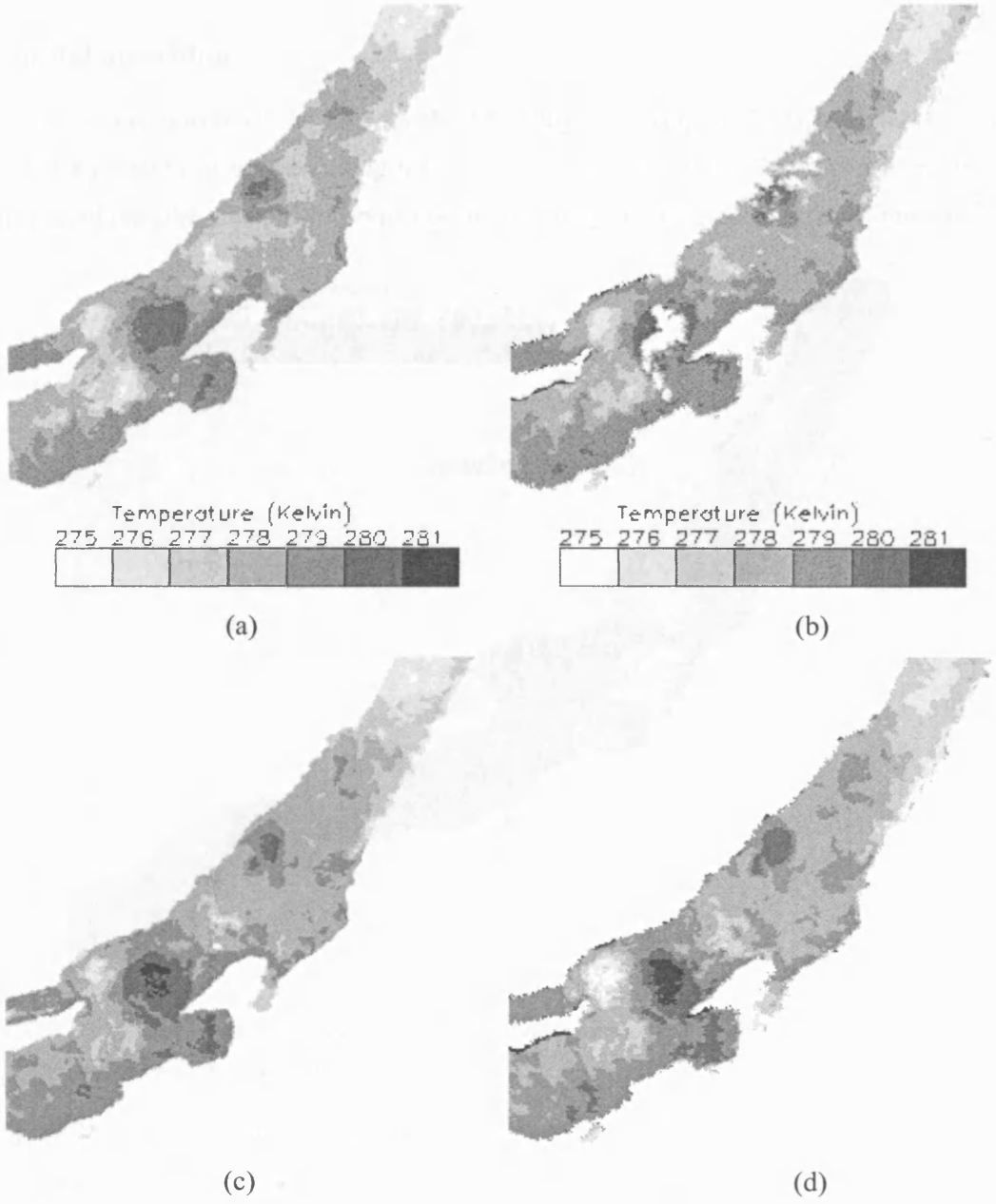

Figure 2.12: **Gyre around Svyatoi Nos Peninsular on (a) 18th October, (b) 19th October, (c) 21st October and (d) 22nd October 1994. 11 μm nadir BT. The white patch over the gyre in (b) is a region of cloud.**

2.4 Coastal upwelling

In the satellite image of the lake for the 17th July 1993 (Figure 2.13), regions of relatively cool (~277 K) water can be seen along the coast of the North Basin. Being considerably cooler than the rest of the lake, this may be evidence of upwelling from the deeper part of the lake.

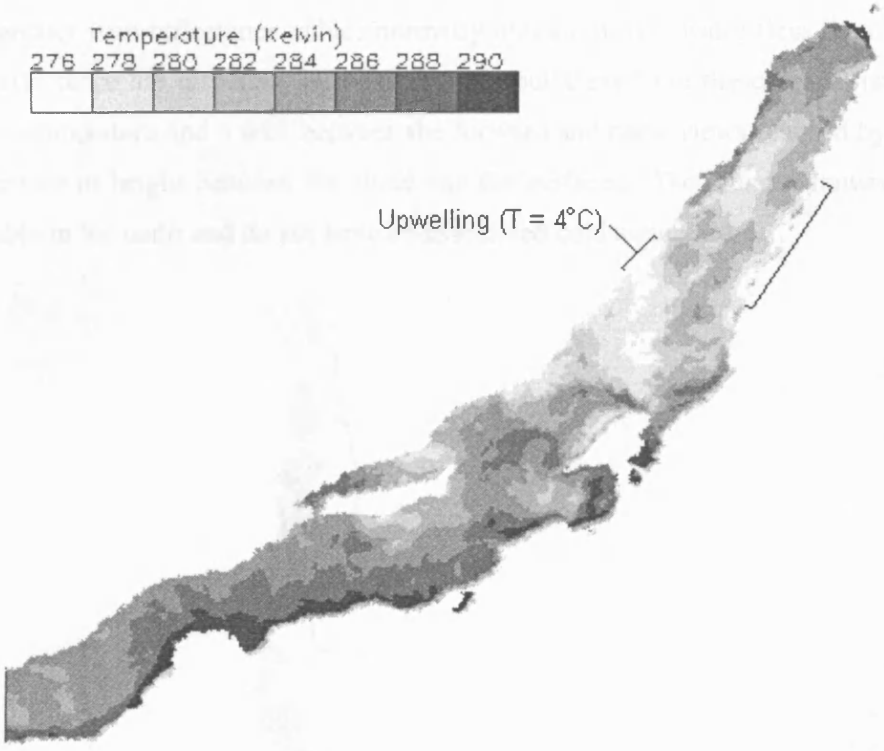

Figure 2.13: Brightness Temperature plot for 17/07/93 showing regions of upwelling of relatively cold (277 K) water along the coasts of the North Basin.

Figure 2.13 illustrates the process of coastal upwelling. Warmer upper layer water is driven to the far shore by strong winds (such as the north-westerlies which occur in Lake Baikal). To maintain mass continuity this water must be replaced by cooler water below, which appears (as in Figure 2.13, for example) as a cool patch on the surface. Upwelling may also arise if resonant internal waves break the surface along the lake boundaries (Goldman and Horne, 1983).

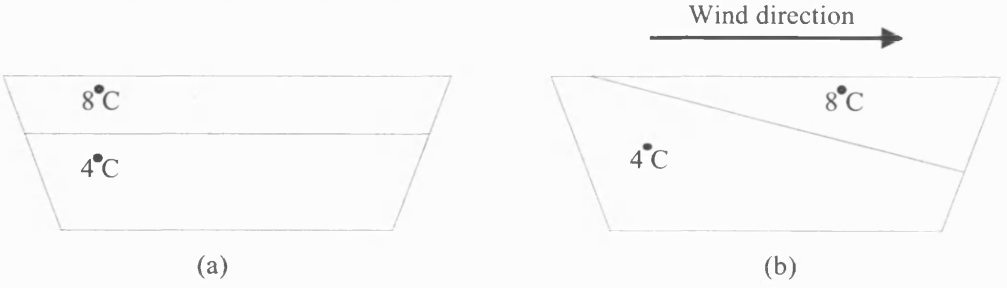

Figure 2.13: Illustration of coastal upwelling. (a) Initially the interface between the upper and lower layers (i.e. the thermocline) is horizontal. (b)When a strong, persistent, wind blows over the surface of the lake, the surface layer (epilimnion) is forced to the far side of the lake, tilting the thermocline and bringing the colder lower layer (hypolimnion) to the surface.

2.5 Suspended sediment plumes

Looking at the 1.6 μm forward channel images for the 19th and 22nd October 1994 reveals regions of water with abnormally high reflectance. These can be seen in Figure 2.14 as three plumes apparently emanating from the mouths of rivers along the south-east coast in the South and Central Basins, as indicated in the figure. Reflectance values within these plumes are up to five times greater than reflectance values normally measured over water (less than 1%). Higher values of reflectance are also seen in these images, but these have the characteristics of cloud, such as low temperature and a shift between the forward and nadir views (caused by parallax due to the difference in height between the cloud and the surface). The plumes, however, are much less noticeable in the nadir and do not have an associated cold temperature.

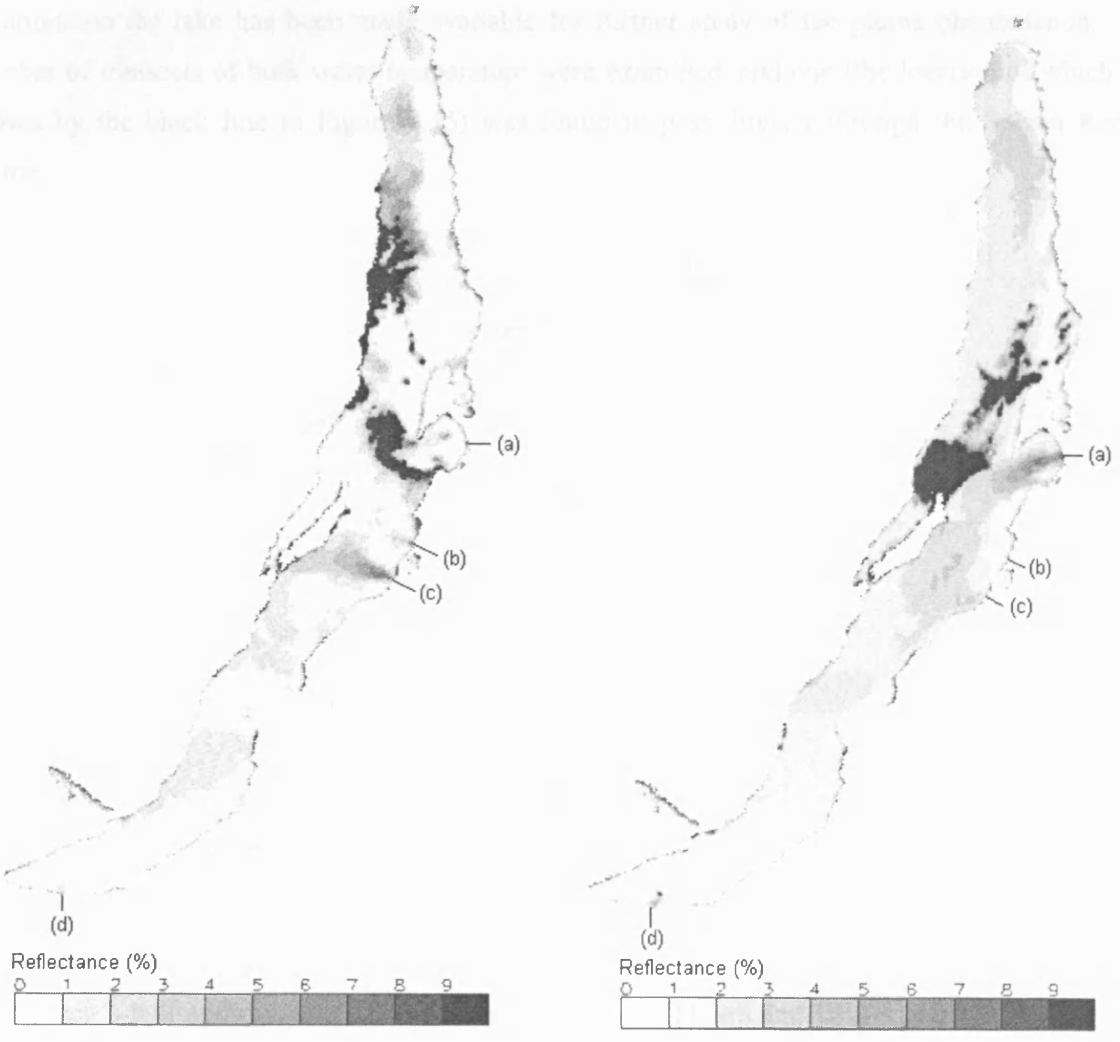

Figure 2.14: **1.6 μm (reflected radiation) forward view satellite data plots for (left) 19th October and (right) 22nd October 1994. The regions of high reflectance in the South and Central Basins occur at the points (a) to (d), where (a) is the Barguzin River, (b) the Turka River, (c) the Kuka River and (d) the Solzan River.**

On the 19th October 1994 (Figure 2.14a) the main plume arises from the south-eastern coast of the Central Basin, from a point coincident with that of the mouth of the Kuka River just south of Lake Kotokel. It extends out to Olkhon Island, the main part of the plume (over 3% reflectance) covering an area over 150 km^2. A smaller plume to the north, coincident with the Turka River mouth, is also visible. By the 22nd October (Figure 2.14b) these plumes have dissipated, but another, coincident with the Barguzin River mouth further north has appeared, also covering a considerable area. A smaller plume is also evident in the South Basin, coincident with the mouth of the Solzan River at Baikalsk, where the pulp and paper mill is located. This plume can also be seen, to a lesser extent, on the 19th October.

During this period of time a scientific expedition was taking place on Lake Baikal by the EAWAG group from ETH, Switzerland. *In situ* temperature data from this cruise for various locations on the lake has been made available for further study of the plume phenomenon. A number of transects of bulk water temperature were examined, and one (the location of which is shown by the black line in Figure 2.15) was found to pass directly through the Solzan River plume.

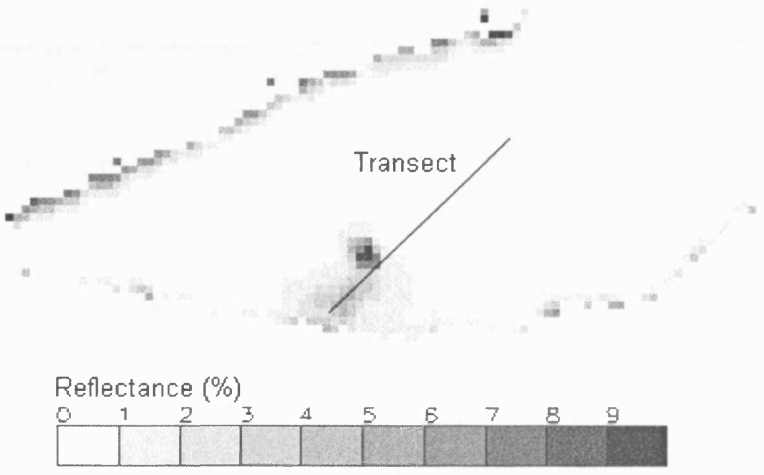

Figure 2.15: Location of the transect used in Figure 2.16, overlaid on the 1.6 μm forward view reflected radiation image for the South Basin.

Figure 2.16a is a plot showing the *in situ* temperature data (obtained from a sensor mounted on the ship's hull approximately 3 m below the surface), 11 μm and 12 μm nadir BTs, and Sea Surface Temperature (SST) data along the transect indicated. The transect begins close to the shore (pixel number 0) and ends approximately in the middle of the South Basin (pixel number 70). The highest reflectance occurs at the end of the plume furthest from the shore, a little less than half way along the transect. The ATSR data transects follow the shape of the *in situ* transect quite closely but are cooler. Temperature differences are approximately 0.5°C, 1.7°C and 2.3°C

for the SST, 11 μm and 12 μm data respectively. The SST is cooler than the *in situ* data due most likely to the skin effect, as discussed in Section 1.2.1. The BTs are cooler due to atmospheric effects. Note the highly variable behaviour of the ATSR data between transect pixel numbers 20 to 30, compared with the *in situ* data.

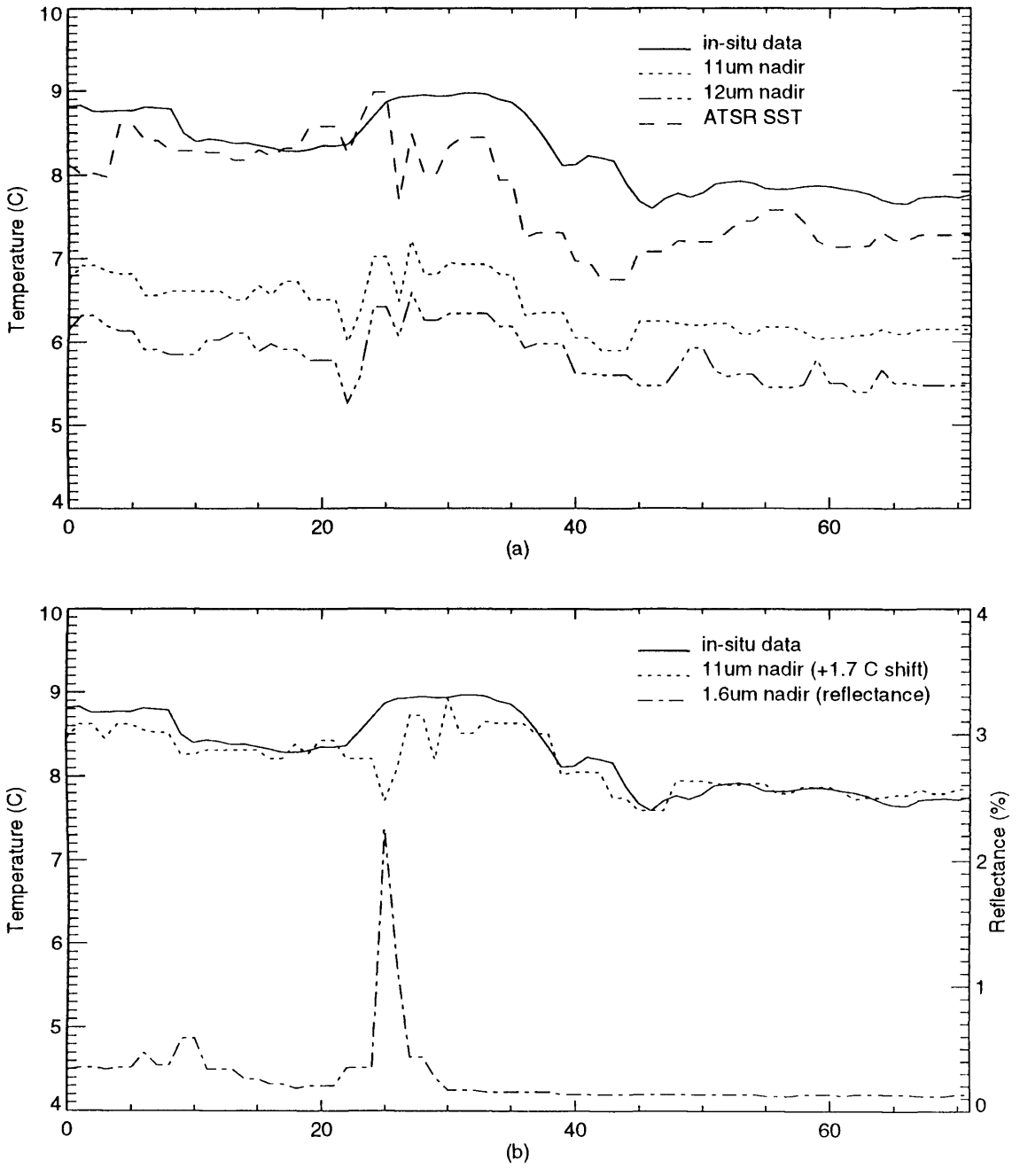

Figure 2.16: ***In situ*** **and satellite data plotted along the transect shown in Figure 2.15. (a)** ***In situ*** **and satellite BT data. (b)** ***In situ*** **and satellite BT and reflected radiation data, showing the apparent decrease in BT in the region of high reflectance.**

Figure 2.16b shows the *in situ* temperature data, the 1.6 μm nadir reflectance data and the 11 μm nadir BT shifted by 1.7°C (so that it can be compared more easily with the *in situ* data). The variation in the 11 μm channel data is now much clearer, and can also be seen to correspond exactly with the region of relatively very high reflectance, seen as a peak of 2.3% (compared with values of 0.2% over pixels 30 to 70). The temperature of the shifted 11 μm channel is 1.2°C cooler than the *in situ* data at this point. Between pixels 0 and 20, where the reflectance is less than the maximum peak but still relatively high, the 11 μm channel is cooler by up to 0.3°C.

From these plots it is clear that the plume observed in the 1.6 μm reflectance channel has caused a substantial decrease in the observed skin temperature (i.e. BT) compared to the bulk temperature (i.e. *in situ* data). This may be caused either by an atmospheric or a surface effect. For example, thin cloud would be visible as a highly reflecting area and would also be likely to result in a reduction in the brightness temperature. Localised effects which may cause a reduction in BT include surface slicks (e.g. from oil) or suspended sediments (e.g. from river run-off). Surface slicks cause the destruction of capillary waves, resulting in a smoother, more highly reflecting, surface. The emissivity of oil tends to be a few percent lower than that of water, which would result in an apparent decrease in the radiative surface temperature (BT) (Robinson *et al.*, 1984). Algal blooms may result in an increase in surface reflectivity, but are accompanied by a thick froth which retards evaporation leading to an *increase* in the apparent surface temperature. Also, being autumn, it is unlikely that the water temperature would be warm enough for algal blooms to occur (Johnson, personal correspondence).

Notes taken by team members of the cruise show that no surface slicks or algal blooms were observed, but that the light transmission of the water along that transect was lower than for other transects. Also, during the previous few days the lake had been subjected to a severe storm. Therefore, it is concluded that the observed regions of high reflectance are due to plumes of suspended sediment from river run-off, caused by the occurrence of a severe storm in the Lake Baikal region.

3. Snow and Ice cover

3.1 Overview

For between four and five months of the year Lake Baikal is completely covered in ice, up to a maximum thickness of about one metre. It is clearly a very important physical feature to understand, as it has a significant impact on the lake system, such as the development of the temperature structure. One particular reason for studying the period of ice cover is to aid numerical modelling of the lake during this time. Ice and snow cover on the lake have the effect of reducing the amount of solar radiation which reaches the water and is, therefore, a major factor in determining heating. Many types of ice occur on the lake (e.g. transparent ice, bubbly white ice, etc.), each with different properties which affect how much of the incident light is transmitted through it. The amount and depth to which solar radiation penetrates depends on factors such as the ice and snow thickness, absorption within the ice, snow and water (a function of extinction coefficients) and the reflectance (albedo) of the surface. In order to obtain realistic results from the model, each of these factors must be known. It is, therefore, not sufficient to say that the lake is covered with a layer of ice and snow for a certain number of months; the type of cover should also be specified to allow heating within the lake to be modelled more accurately. In this chapter, a methodology has been developed to differentiate between different types of cover.

The relatively large spatial coverage of ATSR satellite data compared with *in situ* measurements makes it an essential tool for studying the period of ice cover on the lake. Although snow/ice thickness cannot be determined from thermal or visible channel data, the presence of snow and ice can be detected in the thermal bands and values of reflectance can be obtained from the visible bands of ATSR-2. An average ice thickness, obtained from historical records, could be used as an initial thickness for all pixels classified as ice.

This chapter continues in section 3.2 with a description of ice cover on Lake Baikal, including a remarkable time sequence of satellite images, from the beginning of ice formation in December 1996 through to ice melt in June 1997. Section 3.3 looks in at the differentiation between snow, ice and water, by the analysis of histogram plots of satellite brightness temperature data. Section 3.4 is a similar discussion of snow and ice detection, but uses visible wavelength data. Finally, section 3.5 gives details of how the normalised difference snow index (NDSI) ratio is used as a more accurate means of discriminating between types of ice and snow on the lake. Using this method, classification images of the lake are obtained for a number of dates during the

ice-covered period of 1997. Albedo and extinction coefficient values are assigned to each classification type, which are then integrated into the numerical model discussed in Chapter 5.

3.2 Description of ice cover on Lake Baikal

Satellite images can be used, in conjunction with observations made on Lake Baikal itself, to describe the period of ice cover on the lake. Figure 3.1 below is a time series of ATSR visible wavelength (0.55 μm nadir channel) images spanning the period of ice cover, from December 1996 to June 1997. The complete time series demonstrates particularly well how the excellent spatial and temporal coverage of satellite data can be used to obtain information about large scale processes. The scaling varies between images to produce the optimum contrast, allowing surface features to be detected. The values are uncalibrated counts representing the level of reflected radiation and, therefore, provide an indication of the reflective properties of the surface. For example, it is known that transparent ice reflects very little visible light (about 5%), so it would be expected that this type of surface would appear relatively dark (i.e. low level of reflected radiation) in the satellite images. Conversely, snow reflects a high percentage of visible light (about 70%), and therefore snow-covered regions will appear as relatively bright areas in the satellite images.

The formation of ice cover begins in the North Basin of the lake towards the end of December (Figure 3.1a), and by the beginning of January a relatively uniform sheet of semi-transparent ice stretches from the far north to the mid-point of the Central Basin. At the same time the process of ice formation begins in the South and Central Basins. This takes much longer compared to the north of the lake, and by the 22nd January (Figure 3.1d) a small region of ice-free water remains at the boundary between the South and Central Basins. During February (Figure 3.1e) the pattern of ice remains fairly constant, with regions of clear ice along the north-west coast of the South and Central Basins surrounded by brighter white ice. By mid-March (Figure 3.1f) to the beginning of April (Figure 3.1g), the increase in the level of reflected radiation over the lake suggests that the ice is now snow-covered, although some regions (as before, along the north west-coast) remain snow-free throughout. Mid-April (Figure 3.1h) sees the melt of the snow cover to reveal the white ice beneath, followed a few days (Figure 3.1i) later by the start of ice break-up in the South Basin along the north-west coast. By the end of April (Figure 3.1j) the majority of the south is free of ice, the ice sheet retreating northwards during May (Figure 3.1k), and melting completely by the beginning of June (Figure 3.1l).

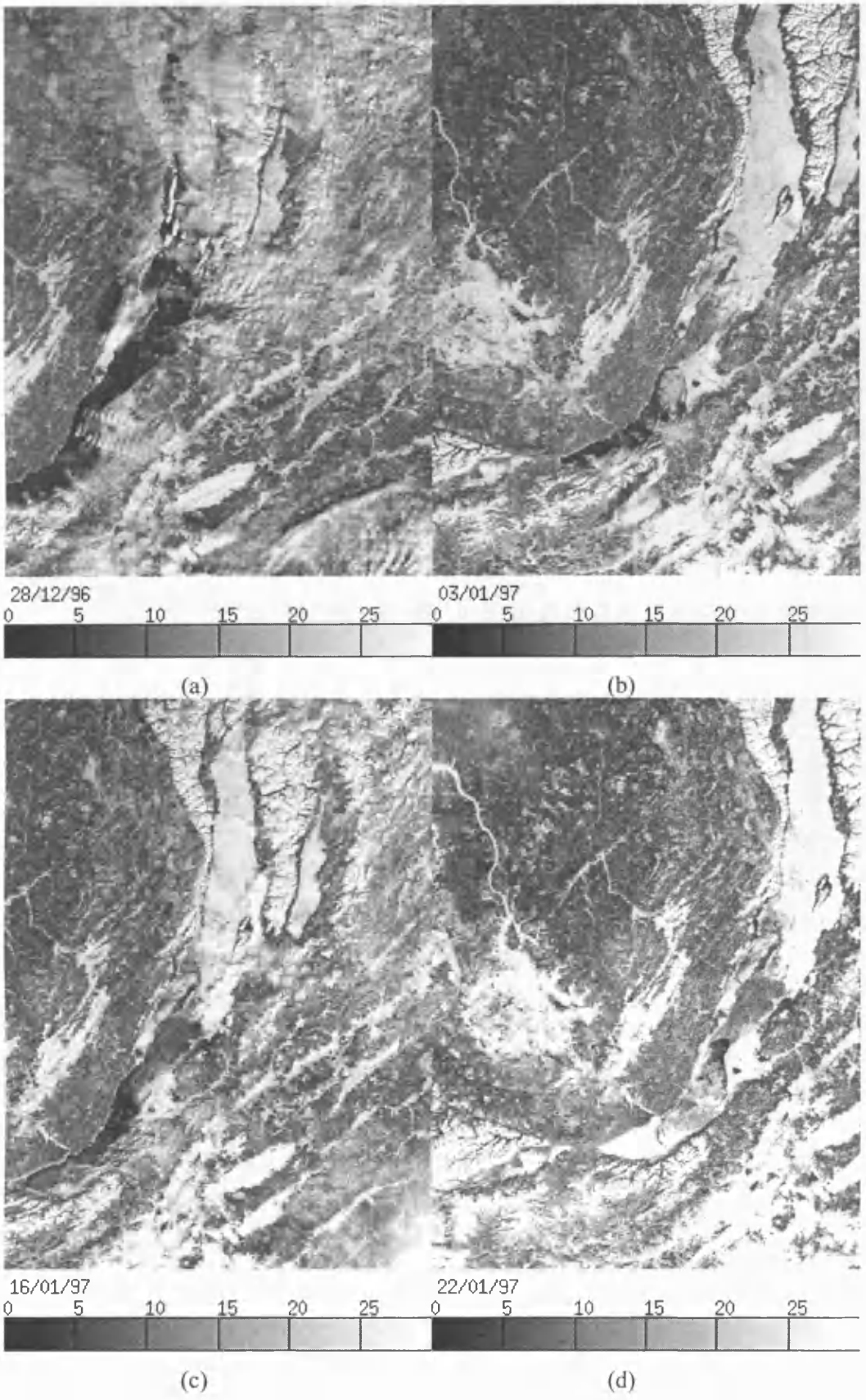

Figure 3.1: **(Page 1 of 3) Time series of visible wavelength satellite data of Lake Baikal between 28th December 1996 and 22nd January 1997. In each image, reflectance is shown as a grey-scale, from the lowest (black) to highest (white) value. The images on this page show the initial formation of the ice, which occurs first in the North Basin (b). Formation of ice in the South Basin is not complete until at least three weeks later (d). (Caption continues on the following pages.)**

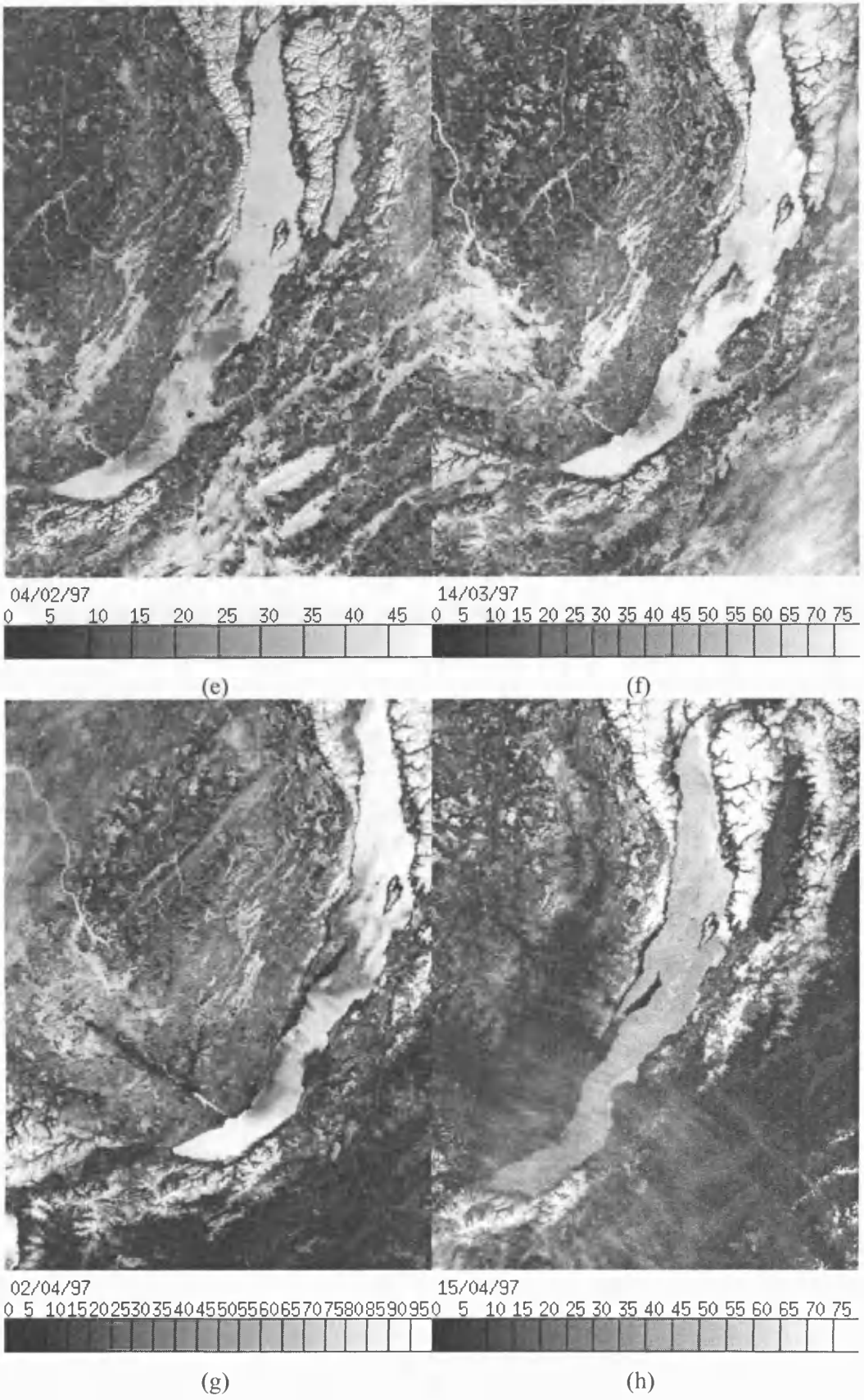

Figure 3.1: **(Page 2 of 3) Time series of Lake Baikal from 4th February to 15th April 1997. In these images the lake is completely ice-covered, and the high reflectivity suggests the presence of snow on the ice. Two regions, on the north-west edge of the South and Central Basins, remain free from snow in images (e) to (g), while (h) shows the whole lake is snow-free.**

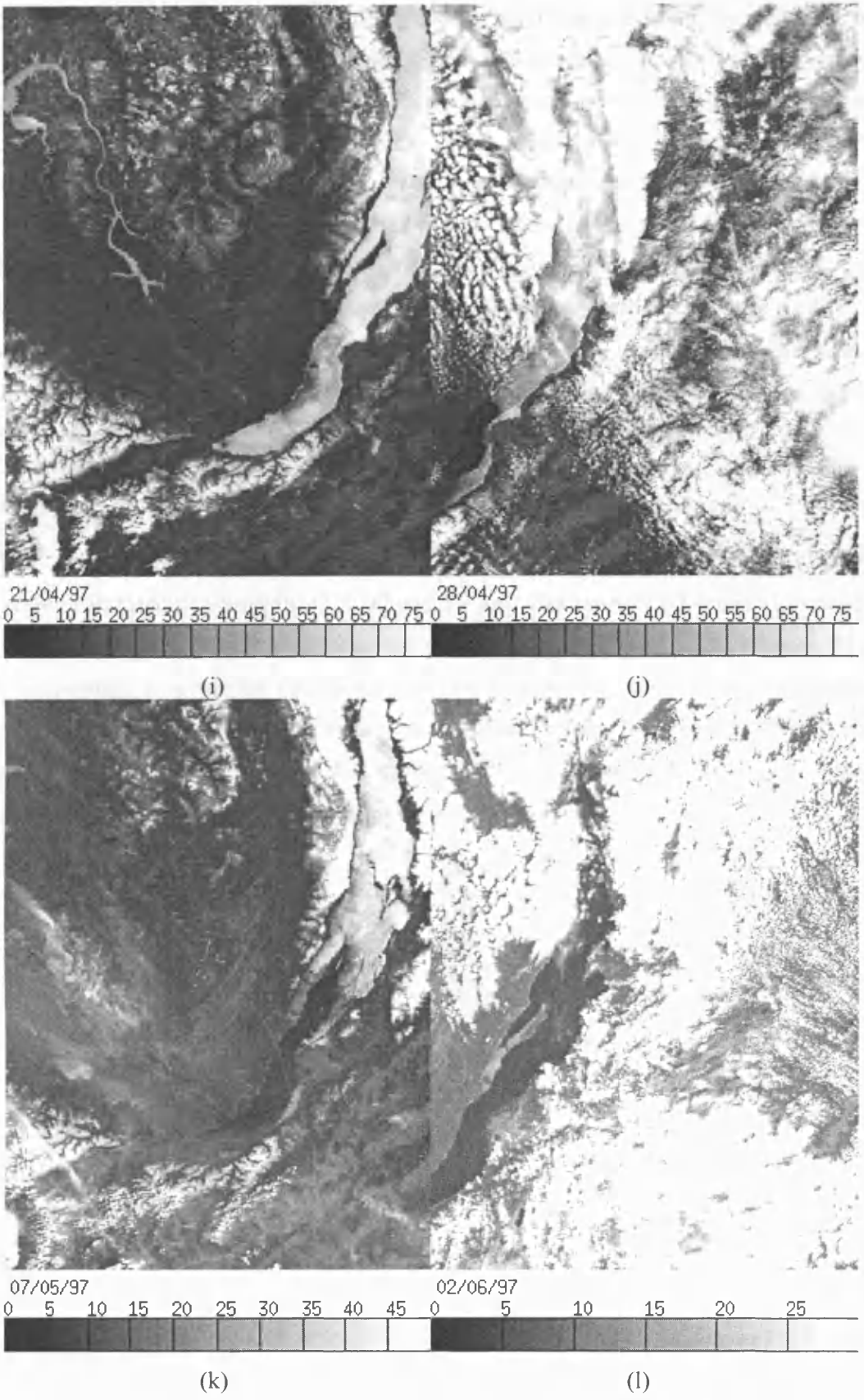

Figure 3.1: (Page 3 of 3) Time series of Lake Baikal from 21st April to 2nd June 1997. In this final set of images the ice can be seen to melt, starting in the South Basin (i). The north of the lake remains covered in ice even when the south is completely free (k). By the beginning of June (l) the entire lake is ice-free.

Observations on the lake show that the ice sheet breaks up due to the formation of 'frazil' ice. Bubbles formed at the surface propagate downwards through the ice, effectively honeycombing it. Eventually, the ice sheet simply becomes a collection of ice 'needles', which can then disintegrate very quickly into slush ice. What seems to be a thick layer of solid ice can therefore disappear rapidly. Another feature which may be observed in the thermal satellite data channels is the formation of ice and snow melt-ponds. These can occur on spring days when the surface melts slightly to produce a thin layer of water overlying the ice, which then re-freezes during the night. As the satellite radiometer measures radiation from the upper surface, large regions of the lake may appear to be completely ice free, having a temperature greater than 0°C. Visible channel data would, however, show these regions to be melt-ponds on thick ice, due to the reflectivity being much greater than that of ice-free water.

3.3 Detection of snow/ice cover using infra-red satellite data

The three thermal infra-red channels of the ATSR instruments measure Brightness Temperatures (BTs) at wavelengths of 11, 12 and 3.7 μm. Examples of BT images can be seen in Figure 3.2, showing the lake during the period of ice cover. The relationship between BTs and actual temperature is given by the Planck function and depends on the wavelength and the emissivity of the surface. For this reason, actual Sea Surface Temperatures (SSTs) can be accurately derived (to better than 0.5 K) because the emissivity of water is known to have an approximately constant value of about 0.99 at 11-12 μm (Zavody *et al.*, 1995).

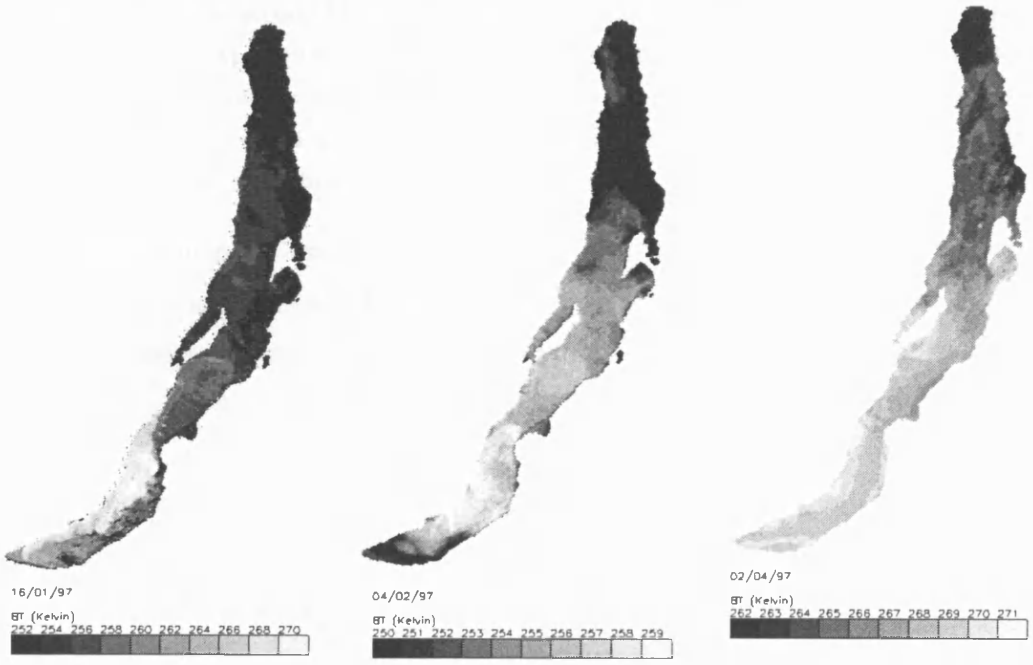

(a) (b) (c)

Figure 3.2: 11 μm nadir BT images of ice covered Lake Baikal for 16th January, 4th February and 2nd April 1997.

Derivation of temperatures over other surfaces (e.g. soil, rock) are much more difficult because the emissivity changes considerably depending on the substance. Since ice and snow both have different emissivities to water (Yu *et al., 1995*) these surfaces will be observed to have different BTs. This effect is quite small at thermal wavelengths (10-12 μm), but is detectable due to the high accuracy (0.1 K) of ATSR BT measurement (Edwards *et al.*, 1990). A change in BT will also be detected if the substances are at different 'actual' temperatures. A histogram plot of lake pixels reveals distinct peaks of Brightness Temperature, corresponding to the different emissivities and temperatures of water, ice and snow (assuming no cloud contamination). Figure 3.3 shows histogram plots of lake pixels for the images in Figure 3.2. Different peaks can clearly be distinguished, corresponding to different surface types, for example snow, ice and water (or an ice/water mix).

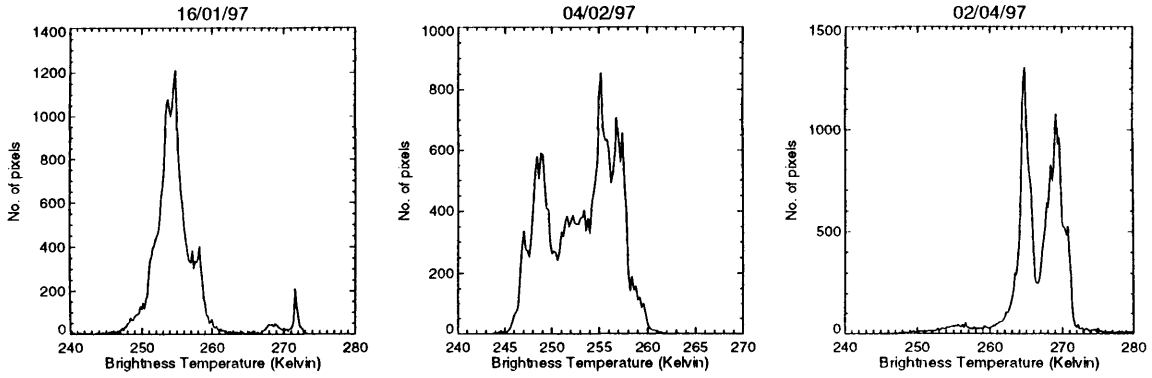

Figure 3.3: Histogram plots of 11 μm nadir BTs over the lake region for (a) 16th January, (b) 4th February and (c) 2nd April 1997. These are used to obtain threshold values, representing interfaces between different surface types, which are then used to produce the classification images in Figure 3.4. Threshold values (i.e. dips between peaks) for each date are: (a) 254K, 257K, 271K; (b) 254K, 256K, 258K; (c) 260K, 266K, 271K.

Although in these images the peaks in the 11 μm BT histograms are separated by several degrees, similar analysis of other images from different times of the year (for example May 1993) generates histograms with peaks separated by only about 0.5 K - 1.5 K, although the peaks are still clearly discernible. Histogram plots of SST products for the same images have only a single peak, since the dependence of temperature on emissivity has effectively been removed from these products. This supports the observation that the peaks are due to differences in emissivity (in addition to differences in actual temperature, SST).

Figure 3.4 shows classification images corresponding to the dates used above, in which the pixels have been classified as being a certain surface type, using BT threshold values obtained from each histogram. Note, however, that there is a considerable degree of uncertainty in determining the actual type of surface (e.g. ice, water or snow) using this method, and some knowledge of ice formation as it occurs on Lake Baikal is necessary.

Summary:

ATSR thermal channel data can be used to differentiate between types of surface cover, in particular ice, snow and water. It is particularly useful for detecting the interface between different surfaces which may not show up clearly in visible images due to a low albedo, but will appear in a Brightness Temperature image as a clear interface because the two surfaces have slightly different emissivities and/or temperatures.

Although useful for detecting the presence of surfaces other than water, this method is insufficiently accurate for determining the actual type of surfaces involved (e.g. whether the interface is water/clear ice, white ice/snow-covered ice etc.), which is necessary if the information is to be incorporated into a numerical model requiring surface albedo (reflectance). This type of analysis would be useful in the absence of visible channels, for example with data obtained prior to the launch of ATSR-2.

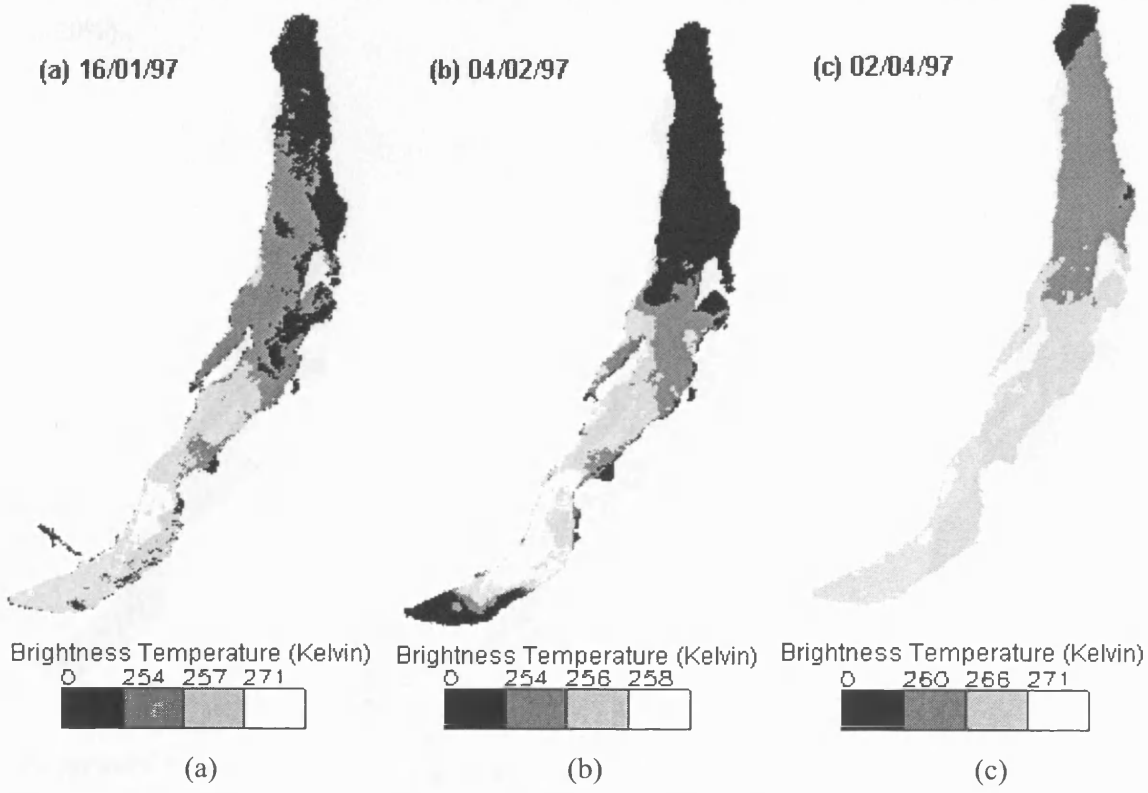

Figure 3.4: Classification images using BT threshold values determined from histogram plots in Figure 3.3, the values of which are shown in the colour key for each image. Four regions are shown in each, which in (a) and (c) may correspond to snow (black), white ice (dark grey), clear ice (light grey) and water (white). In (b) the white region is also likely to be ice, due to the low temperature (258 K). Note that the regions with BT greater than 271 K may be melt ponds (i.e. where only the surface of the ice has melted) rather than completely ice-free areas.

3.4 Detection of snow/ice cover using visible wavelength satellite data

The difference between the emissivities of water, ice and snow is much more pronounced at visible wavelengths than in the infrared, and reflectance increases towards the visible. Absorptance is low, so ice and snow appear white, with fresh snow reflecting more than wet snow, ice and water in that order (Grenfell and Maykut, 1977). Hence the visible channels of ATSR-2 can be used to easily differentiate between these surfaces.

Figure 3.5 shows Lake Baikal, on the three dates used in section 3.3 above, in the visible wavelength (0.55 μm). On 16th January 1997 (Figure 3.5a), the northern half of the lake is reflecting to a much greater extent (20%) compared to the south (5%), with a sharp interface across the middle of the lake. This interface can also be seen in the corresponding thermal image, Figure 3.2a. In Figure 3.5b and c the majority of the lake is reflecting uniformly (30% and 70% respectively), except for regions along the north-west coast of the South and Central Basins (less than 20%).

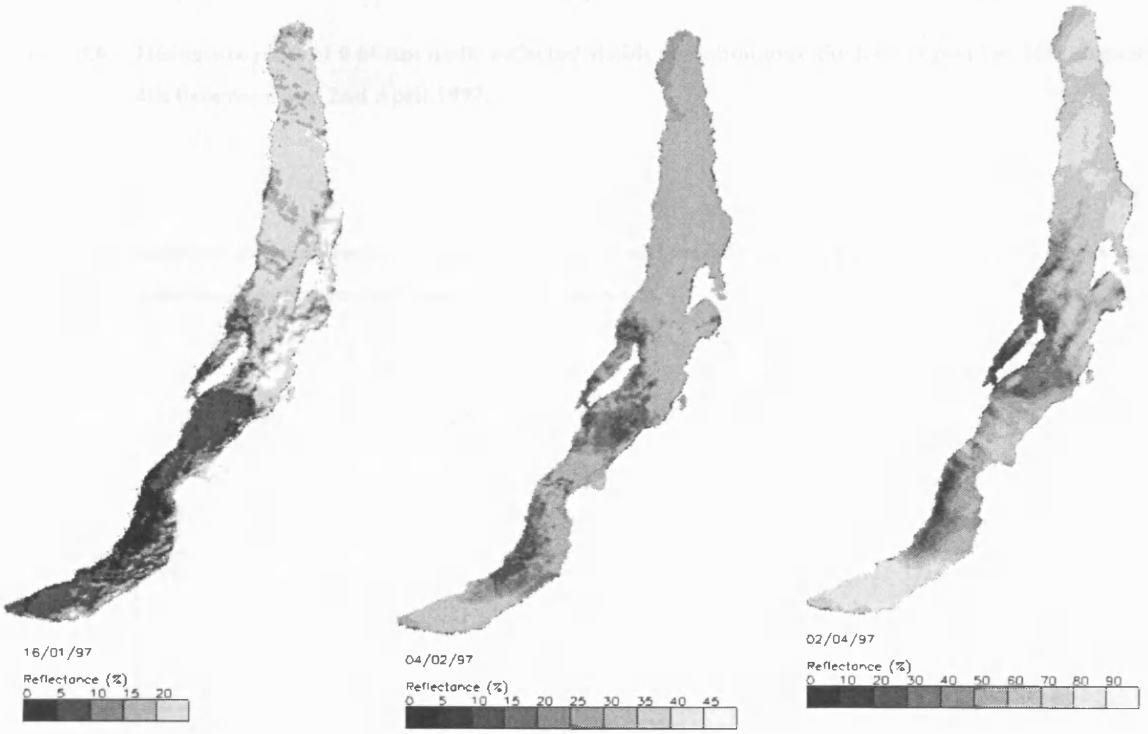

(a) (b) (c)

Figure 3.5: Visible wavelength (0.55 μm) nadir channel satellite images of Lake Baikal for 16th January, 4th February and 2nd April 1997.

Figure 3.6 shows the histograms for the images in Figure 3.5, at the visible wavelength of 0.55 μm. As for the thermal wavelength data, distinct peaks are observed, which are likely to correspond to different surface types. This is due not just to differences in emissivity, but also to the albedo of each type. Typical albedo values recorded for Lake Baikal are: 5% for water; 28% for transparent ice; 50% white ice/old snow; and 70% for snow (Shimaraev *et al.*, 1994). The albedo of snow and ice can vary considerably, however, depending on the condition of the

surface. For example, if the snow is fresh the reflectance is higher than if it is old or wet. Transparent, bubble-free ice has a much lower reflectance than cloudy, 'white' ice (Matthews and Heaney, 1987). Reflectance threshold values can be obtained from the histogram plots in order to classify the image pixels, as given in Table 3.1.

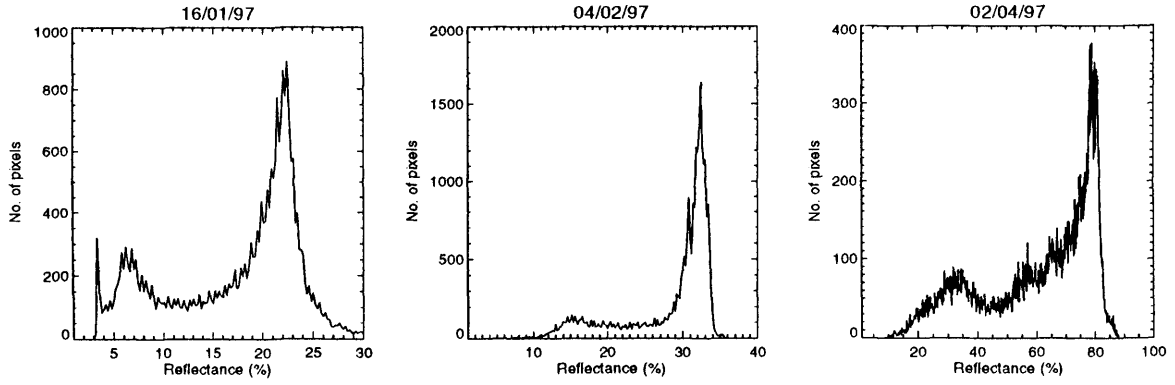

(a) (b) (c)

Figure 3.6: Histogram plots of 0.66 μm nadir reflected visible radiation over the lake region for 16th January, 4th February and 2nd April 1997.

Table 3.1: Threshold reflected radiation values and associated classification types (and assigned colours used in classification images in Figure 3.4) for lake pixels.

16/01/97		04/02/97		02/04/97	
Reflectance thresholds	Classification type; assigned colour scale	Reflectance thresholds	Classification type; assigned colour scale	Reflectance thresholds	Classification type; assigned colour scale
0 - 4	water/ice mix (black)	0 - 18	transparent ice (black)	0 - 45	semi-transparent ice (black)
4 - 9	transparent ice (dark grey)	18 - 27	semi-transparent ice (dark grey)	45 - 60	new white ice (dark grey)
9 - 19	semi-transparent ice (light grey)	27 - 31	new white ice (light grey)	60 - 70	old white ice (light grey)
> 19	white ice (white)	> 31	old white ice (white)	> 70	snow (white)

Using the threshold values given in Table 3.1, classification images similar to those in Figure 3.4 can be obtained, as shown in Figure 3.7. Between January and April the level of reflected radiation increases over the whole lake, indicating the change in surface type from clear ice to snow-covered ice. The increase will also be due in part to the increase in solar inclination from 20

degrees in January to 50 degrees in April. This will cause an increase in the incident solar radiation, and also a greater percentage of that radiation to be reflected into the field of view of the satellite detector. Caution should therefore be used when assigning classification types according to actual reflectance values.

Comparisons between these classification images and those in Figure 3.4 show that there are many coincident features. For example, in Figure 3.7a there is an interface between two surface types (white ice and transparent ice) halfway along the lake, and a patch (water/ice mix) south of the Selenga Delta, which also appears in Figure 3.4a.

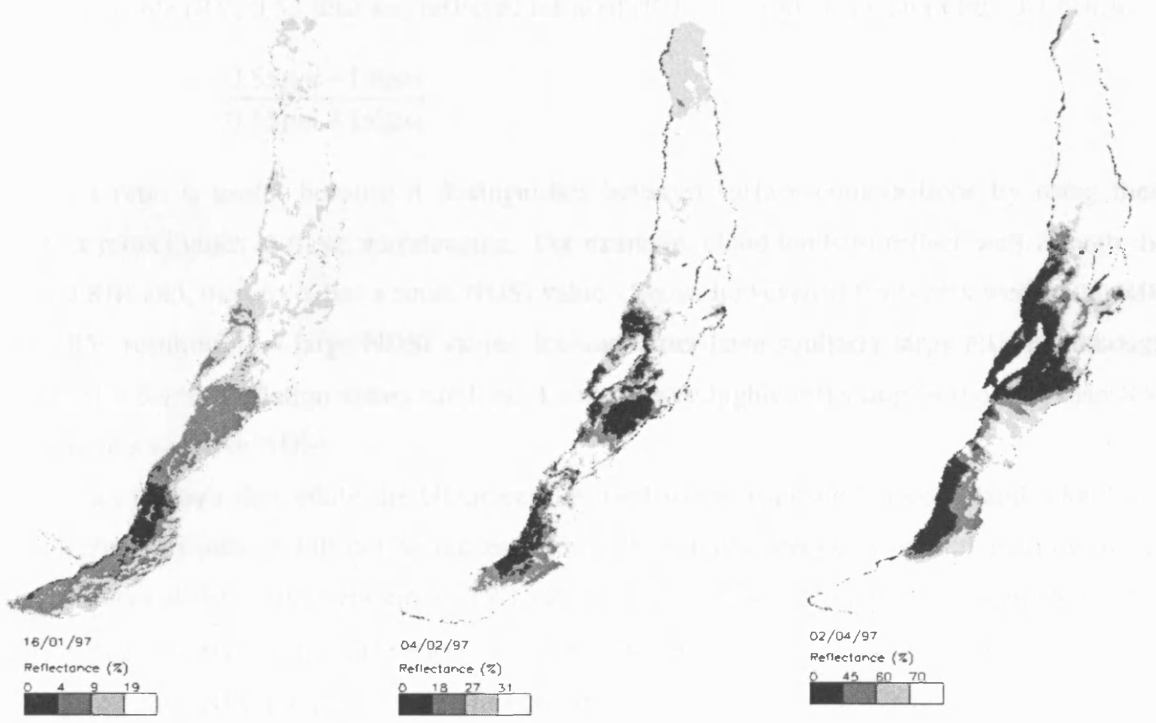

(a) (b) (c)

Figure 3.7: Classification images using visible wavelength (0.66 μm nadir channel) threshold values determined from histogram plots in Figure 3.6, the values of which are shown in the colour key for each image (and given in Table 3.1). Four regions are shown in each, which correspond to different surface types, e.g. transparent ice (black), semi-clear ice (dark grey), white ice (light grey), and snow (white).

Summary:

ATSR-2 visible channel data (at wavelengths 0.87, 0.67 and 0.55 mm) can be used to obtain threshold values for the classification of lake pixels as either water, ice or snow. To some extent, comparison between known albedos and the reflected radiation values can be used to determine the type of surface (e.g. high values, around 70%, suggest snow; low values, around 10%, suggest transparent ice). This information could be used to assign albedo and extinction coefficients to regions of the lake for input to a numerical model. However, histogram analysis of visible wavelength data alone was not thought to be sufficiently accurate, and so an additional method is discussed below.

3.5 Use of NDSI and Near IR to detect ice and snow

One of the problems with using levels of reflected radiation to determine the presence of snow and ice is that of cloud cover, which, due to its low temperature and highly reflecting appearance, can easily be mistaken for snow or ice. An additional method for discriminating between different surface types is one which utilises a ratio known as the Normalised Difference Snow Index (NDSI) (Riggs, 1995), defined as being the normalised difference between the reflected visible (RV, 0.55 μm) and reflected infrared (RIR, 1.6 μm), as given in Eq. 3.1 below:

Eq. 3.1
$$\frac{0.55\mu m - 1.6\mu m}{0.55\mu m + 1.6\mu m}$$

This ratio is useful because it distinguishes between surface compositions by using their different reflectivities at these wavelengths. For example, cloud tends to reflect well in both the RV and RIR and, therefore, has a small NDSI value. Snow, however, reflects less well in the RIR as the RV, resulting in a large NDSI value. Ice and water have similarly large NDSIs, although the actual reflected radiation values are less. Land is more highly reflecting in the RIR than RV, resulting in a negative NDSI.

It can be seen that while the NDSI can be used to discriminate between land, cloud and snow/ice/water pixels, it will not be successful in differentiating between snow, ice and water as these surfaces all have similarly large NDSI values. For this we use the near infrared (NIR, 0.87 μm), as there are significant differences between these surfaces at this wavelength. Scatter plots of NDSI against NIR for pixel values in each image produces characteristic patterns. This is illustrated by the three pairs of NDSI/NIR plots in Figure 3.8 below. On the left are NDSI images of the Selenga Delta area, which show regions of high NDSI (white), e.g. water or ice, and low NDSI (black), e.g. land. On the right are NDSI/NIR scatter plots for the region shown in the left-hand plots. Land pixels tend to form a characteristic curve (particularly well illustrated in Figure 3.8b and c) which stretches from about 20% NIR, -0.5 NDSI to 50% NIR, 0.5 NDSI. Ice and snow pixels form a curve along the top of the plots, from about 10% NIR, 0.8 NDSI (e.g. clear ice) to 90% NIR, 0.8 NDSI (e.g. snow).

Examining NDSI/NIR plots concurrently with visual interpretation of the satellite images for all the available dates during the period of ice cover in 1997 reveals the following characteristics:

Water:

Characterised by a high NDSI (0.6 to 0.9) but low NIR (< 10%). The spread in NDSI values is due to changes in the 1.6 μm channel being more pronounced than in the 0.55 μm channel. i.e. a small increase in the visible (0.55 μm) is accompanied by a larger increase in the 1.6 μm, resulting in a decrease in NDSI. Increases at these wavelengths could be due to turbidity, surface roughness, plankton blooms or thin cirrus cloud.

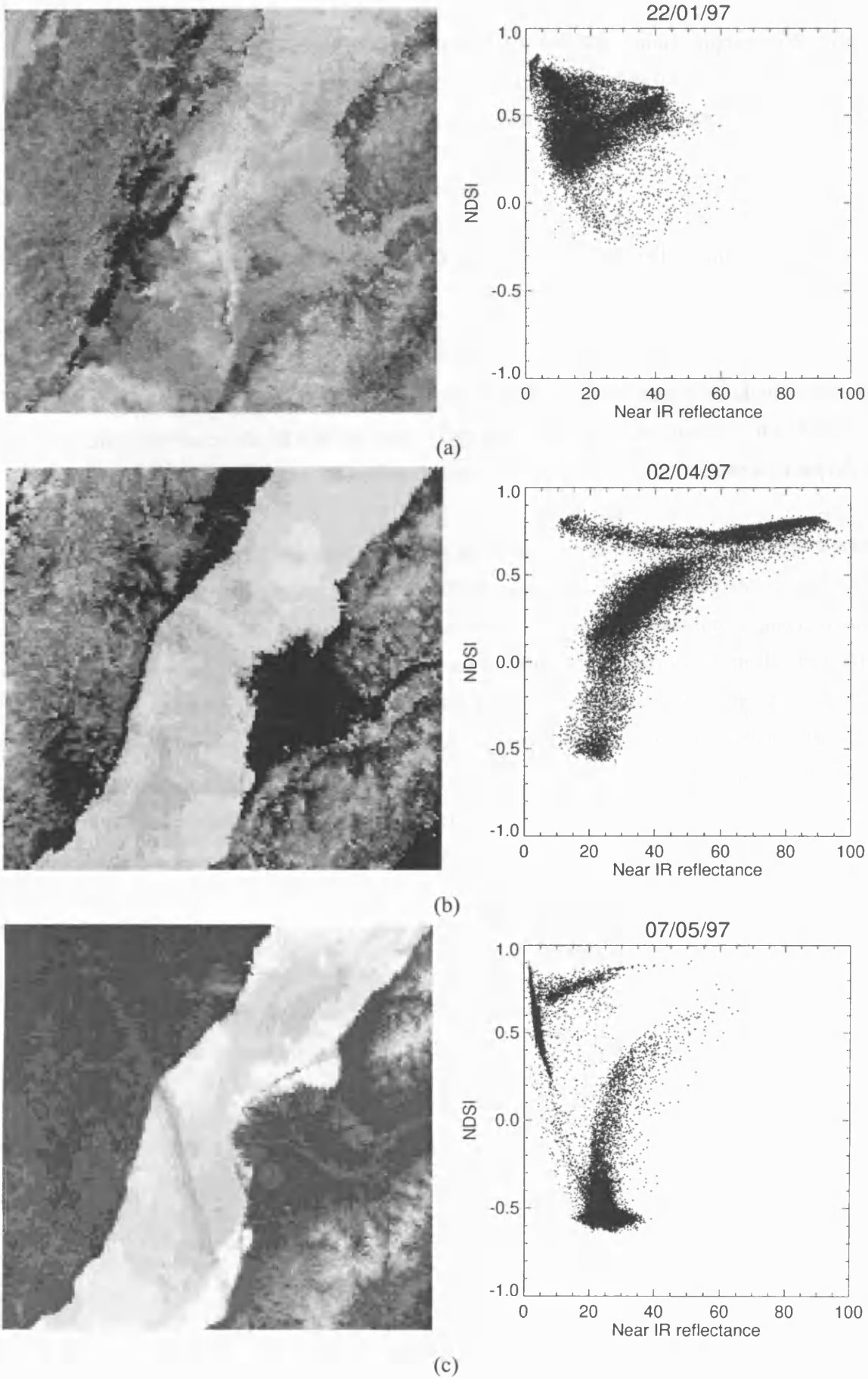

Figure 3.8: **(Left) NDSI images derived from satellite data of the Selenga Delta region on (a) 22nd January, (b) 2nd April and (c) 7th May 1997. (Right) NDSI vs. NIR scatter plot for the regions shown on the left.**

Ice and snow:

Again, characterised by a high NDSI (0.6 to 0.9), but with much higher NIR values, depending on the type of ice or snow. Typical values range from 5% (clear ice), through 40% (white ice) to 80% (snow). The NDSI value for snow tends to be slightly higher than for ice, due to a greater difference between the NIR and RV.

Land:

Characterised by negative NDSI (-0.3) and average (20 - 40%) NIR. Snow covered land will of course have a high NDSI.

Cloud:

Clouds have an extremely complex 'signature' due to the great variety of cloud types, and tend to produce curves on the NDSI/NIR plots. This is thought to be due partly to the changes in the brightness of the reflected light, caused by differences in the angle of reflection at cloud edges.

Figure 3.9 summarises these characteristics, showing regions on an NDSI/NIR plot which correspond to the different 'classes' of surface (land, water, ice etc.). Using this generic plot, threshold values of NDSI and NIR can be obtained, allowing the classification of pixels into the specified surface types. In addition to the reflected radiation data, thermal channels are used to obtain temperature thresholds. This can be useful when differentiating between water and very clear ice (which have very similar NDSI and NIR values), and also to detect melt ponds (which appear to be ice or snow apart from having a relatively high temperature). These threshold values, and the associated classification types, are given in Table 3.2 below. Each pixel in a given satellite image can now be assigned a surface type according to these threshold values, to produce classification images as shown in Figure 3.10. Ideally, co-incident *in situ* data should be used for validation of this procedure. In the absence of this, historical observations are used, along with visual interpretation of the satellite images. For example, frazil ice starts to occur on the lake from the end of March/early April but is most prevalent during ice break-up in May. Transparent ice is most common at the start of ice formation in January.

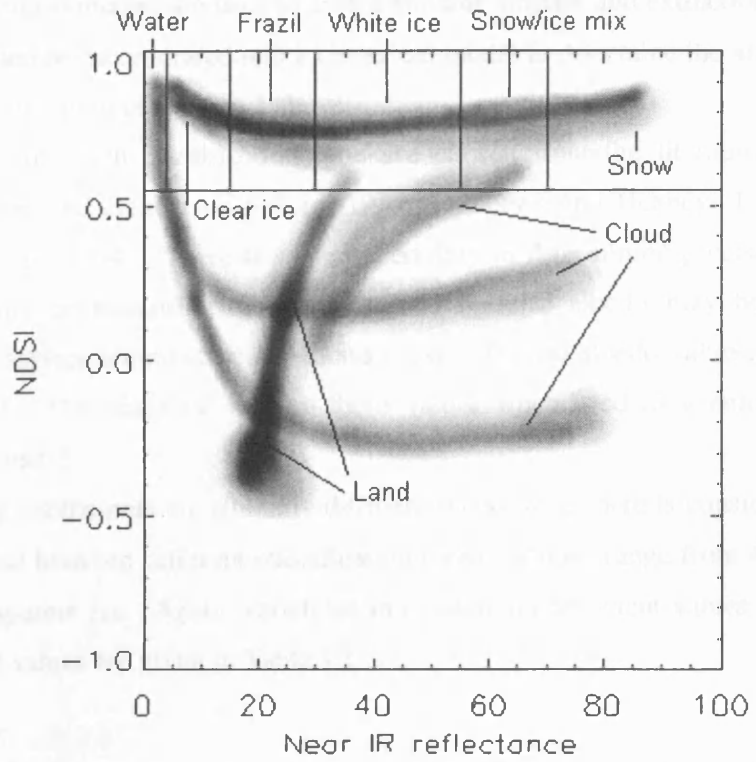

Figure 3.9: **Generic NDSI/NIR plot derived from analysis of satellite data between January and June 1997. The dark bands show the characteristic patterns corresponding to different pixel types. The band along the top, at NDSIs greater than 0.55, is sub-divided into different types of ice and snow, using NIR values as thresholds.**

Table 3.2: Threshold values used to assign classification types to pixels.

Classification type	Thresholds		
	NIR	BT	NDSI
Water	< 4%	> 270 K	> 0.55
Clear (fresh) ice	< 15%	< 270 K	> 0.55
Slush ice	< 15%	> 270 K	> 0.55
Frazil ice	< 30%	> 270 K	> 0.55
Fresh white ice	< 55%	< 255 K	> 0.55
Old white ice	< 55%	> 255, < 270 K	> 0.55
White ice melt pond	< 55%	> 270 K	> 0.55
Clear/white ice mix	< 30%	< 270 K	> 0.55
Ice/snow mix	> 55%, < 70%	< 270 K	> 0.55
Snow melt pond	> 55%, < 70%	> 270 K	> 0.55
Snow	> 70%	< 270 K	> 0.55

These classification images are used to assign suitable albedos and extinction coefficients to pixels, which can then be incorporated into a numerical model to determine the under-ice heating, as discussed at the beginning of Section 3 above.

Albedo values for each classification type are chosen from the literature (Grenfell and Maykut, 1977; Shine and Henderson-Sellers, 1985; Matthews and Heaney, 1987; Morassutti, 1989; Shimaraev *et al.*, 1994). There is some uncertainty in determining precise values, due in part to the difficulty in measuring albedo, and also because albedo may be a function of conditions such as surface temperature and cloud cover. Typical albedo values chosen here are given in Table 3.3. The effect of varying these values when used in a numerical model is investigated in Chapter 5.

The extinction coefficients are similarly difficult to choose as there is considerable variation with wavelength and between different classification types. Values range from 40 m^{-1} for snow, to 0.2 m^{-1} for transparent ice. Again, variations in extinction coefficient values are discussed in Chapter 5. Typical values are given in Table 3.3.

Table 3.3: Albedo and extinction coefficient values* assigned to each classification type, for use in a numerical model.

Classification type	Albedo (%)	Extinction coefficient (m^{-1})
Water	5	0.2
Clear (fresh) ice	25	0.2
Slush ice	20	3.5
Frazil ice	25	3.5
Fresh white ice	45	2.0
Old white ice	40	3.0
White ice melt pond	38	3.0
Semi-transparent ice	30	0.8
Ice/snow mix	50	2.0
Snow melt pond	58	40.0
Snow	60	40.0

* (Grenfell and Maykut, 1977; Shine and Henderson-Sellers, 1985; Matthews and Heaney, 1987; Morassutti, 1989; Shimaraev *et al.*, 1994)

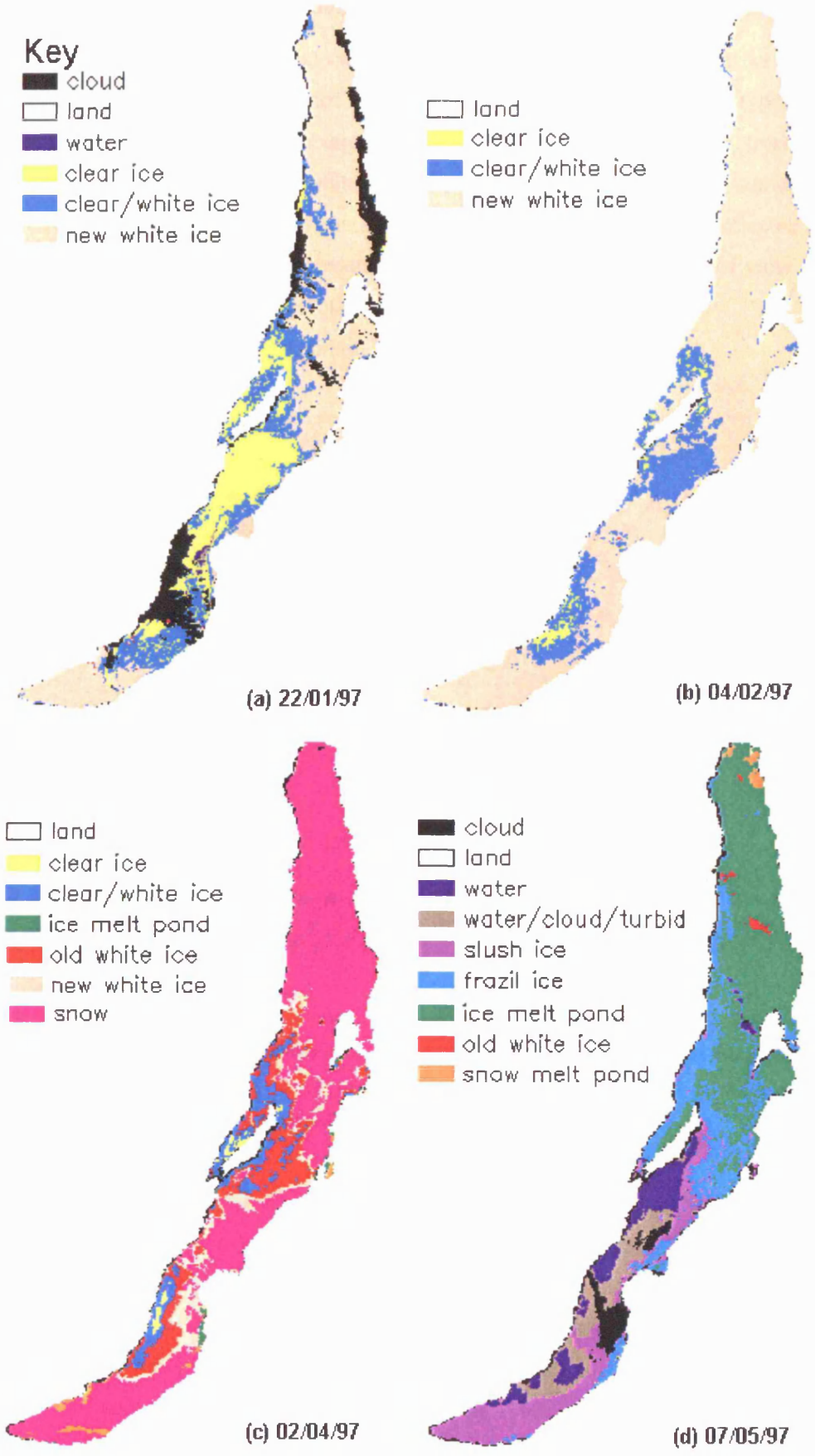

Figure 3.10: Classification images for (a) 22/01/97, (b) 04/02/97, (c) 02/04/97 and (d) 07/05/97.

3.5.1 Quantitative analysis of ice-covered period

The ice and snow covered period can be analysed in terms of percentages of surface type using the classification data. In the plot below (Figure 3.11) the classification types have been grouped together for simplicity. For example: 'ice' includes clear, slush, frazil, fresh white, old white, white ice melt pond and clear/white mix; 'snow' includes ice/snow mix, snow melt pond and snow. To reduce the possibility of contamination of the results, images are selected according to the percentage cloud cover and the percentage of the lake visible in the field of view. In Figure 3.11 these are chosen to be less than 60% and greater than 80% respectively. The values are given as the percentage of cloud-free pixels.

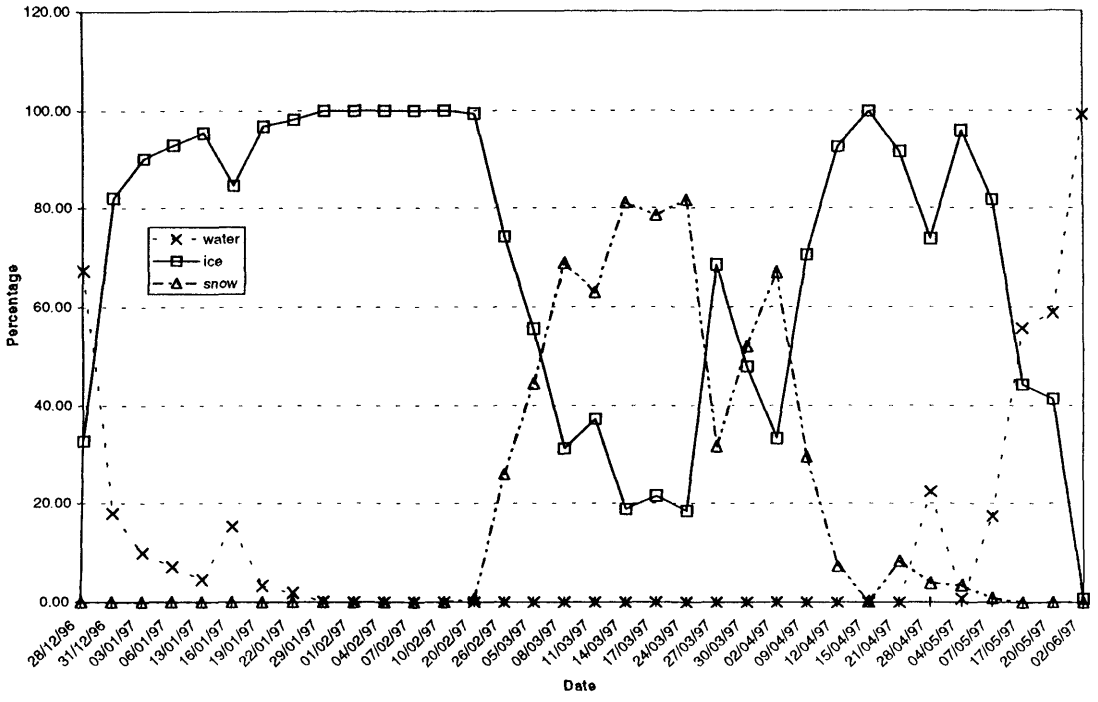

Figure 3.11: Plot of percentage cover for water, ice and snow surface types with time, using classification images between 28th December 1996 and 2nd June 1997. This analysis uses images in which more than 80% of the lake is visible in the field of view and less than 60% of the image is cloudy. Values are expressed as a percentage of cloud-free pixels.

Figure 3.11 clearly shows how different surface types predominate at different times of the year. Between the beginning of January and late February more than 80% of the lake is ice covered, with complete freeze-up occurring on the 1st February. Between the end of February and the beginning of April the ice becomes snow-covered, although 20-30% of the lake remains snow-free. By mid-April the snow has melted almost entirely, and the ice itself melts quickly during May. The lake is completely ice-free by 2nd June 1997.

This analysis using classification data agrees very well with observations made on the lake, the general pattern of ice and snow formation being similar from year to year. This suggests that the classification scheme used produces very good results, and can be incorporated into a numerical model with a high level of confidence.

4. Single layer barotropic model

4.1 Overview

Of the many physical processes which occur in Lake Baikal, deep water renewal is one of the most intriguing and least well understood (Weiss *et al.*, 1991; Shimaraev *et al.*, 1993). There are a number of theories of why the lake is so well oxygenated throughout its depth, including convective overturn in the region of thermal bars, and thermobaric instabilities generated by internal waves. Another possible mechanism involves gyres, which have been observed in many satellite images of the lake (see Fig 2.11). It is possible that these large rotating structures could provide a means of injecting surface water, and thus oxygen, into the deeper parts of the lake. As was noted in chapter 2, gyres have only been observed in the region of the Academician Ridge in the latter half of the year, most frequently in October.

This chapter describes and presents results from a numerical model of Lake Baikal, which was developed in order to generate gyres, and to determine the factors which influence their formation. In section 4.2 the model is described and the equations which define it are given, along with a brief discussion of numerical modelling techniques. The conditions with which the model was initialised are given in section 4.3, and results for each of the model runs are presented in section 4.4. The chapter concludes with a summary and discussion in section 4.5.

4.2 Model description

The model was developed for application to Lake Baikal from an existing barotropic model of the Pacific Ocean (McCreary and Anderson, 1983). The model consists of a single layer, with an equilibrium depth, H. The displacement, η, from this equilibrium (due, for example, to wind stresses on the surface) generates pressure gradients in the fluid, which in turn give rise to current motion. See Figure 4.1 for a schematic representation.

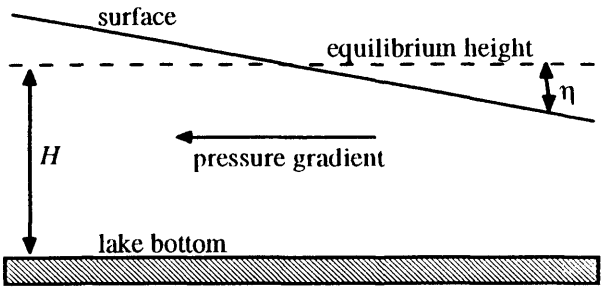

Figure 4.1: Schematic representation of the barotropic model, showing the equilibrium depth H, the surface displacement from the equilibrium, η, and the direction of the pressure gradient for the displacement shown.

The model consists of the Navier-Stokes equation (Eq. 4.1) and the equation of mass continuity (Eq. 4.2). The former of these is derived from Newton's second law and the hydrostatic equation. The result of solving these equations at progressive time steps is the surface height displacement and the flow derived from it. The rate of change of velocity v is given by Eq. 4.1 below:

Eq. 4.1
$$\frac{\delta v}{\partial t} = -g\nabla\eta - 2\Omega\times v + \tau + \mu\nabla^2 v$$

where v is the velocity vector, Ω is the Coriolis parameter, η is the surface displacement (surface height minus equilibrium surface height), g is acceleration due to gravity, τ is the wind stress and μ is the coefficient of viscosity (Gill, 1982). The terms from left to right respectively represent: local inertia force; the pressure gradient force; Coriolis force; wind stress; and viscous force. A term representing convective inertia, $v.\nabla v$, provides a relatively small contribution, and has, therefore, not been included in this model for computational efficiency.

In order to solve Eq. 4.1, η is determined using the equation of mass continuity, which states that the mass of water flowing into a volume element *dxdydz* must be balanced by the mass of water flowing out of that volume and any sources or sinks which, in the case of Lake Baikal, consist of river inflow and outflow. The equation, written in terms of η, is

Eq. 4.2
$$\frac{\partial\eta}{\partial t} = -\nabla(Hv) + Q$$

where η, H, v are as defined previously, and Q represents sources (or sinks) of mass (Gill, 1982).

The equations of motion described above are solved for the speeds u and v, and surface displacement η at regularly spaced intervals lying on a grid with a resolution of 0.05° longitude by 0.05° latitude ($d\lambda$, $d\theta$). Figure 4.2 is a schematic of the model grid showing the boundary of the lake. To reduce computation time the equations are solved only within the region enclosing

the lake cells. The grid cell spacings in kilometres (Δx and Δy) are constant with longitude but vary with latitude, as can be seen in Figure 4.3. Grid cells are approximately 3.2 x 5.6 km.

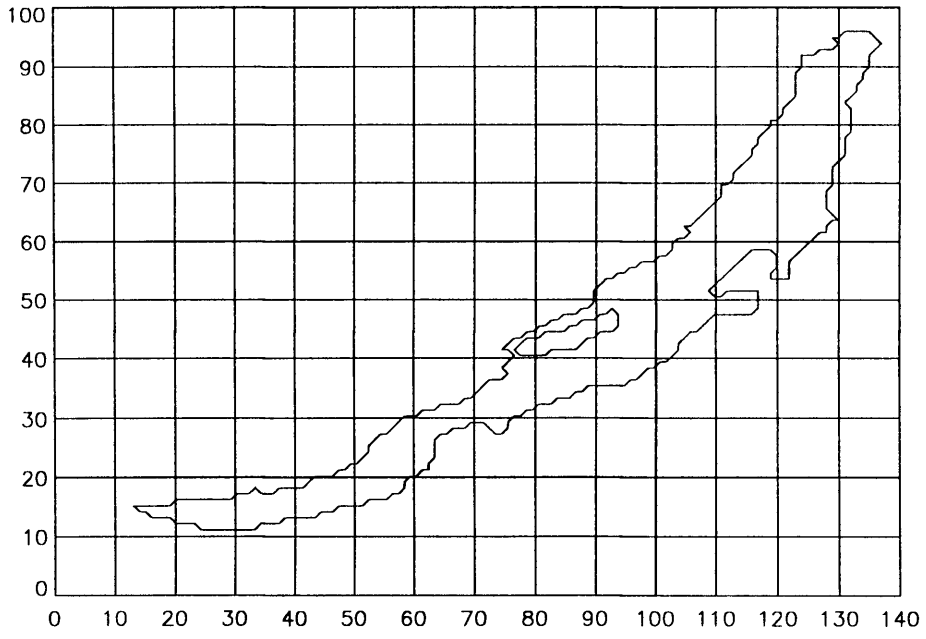

Figure 4.2: Lake Baikal model grid. 140 x 100 cells, 0.05° longitude x 0.05° latitude. Hereafter, the direction of x is defined to be positive in an easterly direction, and y is positive in a northerly direction (i.e. as given by the x and y axes in this figure).

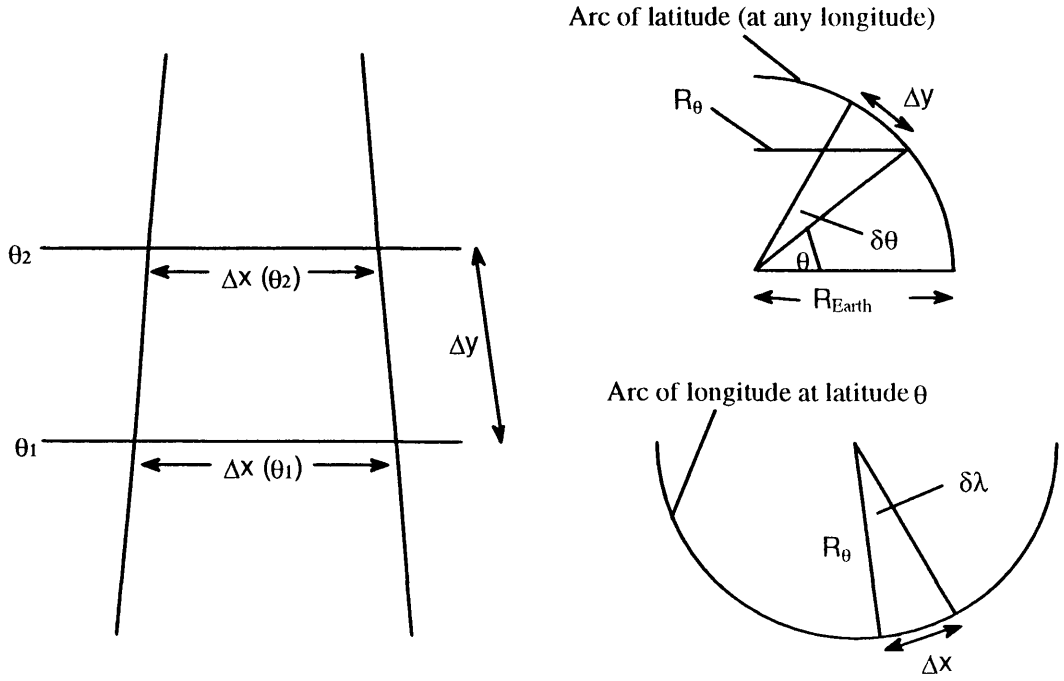

Figure 4.3: Schematic showing how grid cell spacings (in kilometres) are dependent on latitude.

For small angles $\delta\theta$, $\delta\lambda$ (in radians):

$$\Delta x = R_\theta \, \delta\lambda = R_{Earth} \cos(\theta) \, \delta\lambda$$

$$\Delta x = 6371 \text{ x } \cos(55°) \text{ x } 0.05° \text{ x } \pi/180 = 3.2 \text{ km}$$

$$\Delta y = R_{Earth} \, \delta\theta$$

$$\Delta y = 6371 \text{ x } 0.05° \text{ x } \pi/180 = 5.6 \text{ km}$$

For reasons of numerical stability, each variable must be calculated at a different location on the grid box - a technique known as the multi-grid method. Figure 4.4 shows the locations within the grid at which the equations are solved, and the nomenclature used. Heights are calculated at the centre of each grid box (H-point), velocity in the x-direction (denoted by i subscripts) is calculated at the centre of the right hand edge (U-point) and velocity in the y-direction (denoted by j subscripts) is calculated at the centre of the top edge (V-point).

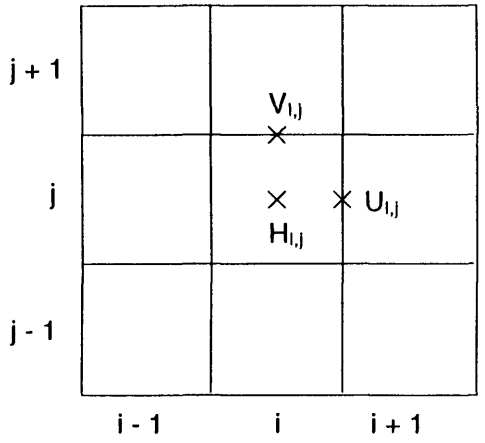

Figure 4.4: Grid layout and nomenclature used in the model

Full details of the numerical methods used will not be described here, as they are well documented in the many texts on the subject (e.g. Keller, 1978; Press *et al.*, 1986; Abbott and Basco, 1989; Hoffmann, 1993). A brief outline of the methods, however, is given below.

The equations to be solved are Partial Differential Equations (PDEs), which are generally difficult to solve exactly. Instead, approximations to the PDEs are made, by substituting the exact partial derivatives within the equation with a Finite Difference Approximation (FDA). The resulting equation is then a Finite Difference Equation (FDE), which can be solved numerically. Before an FDA can be derived, a finite difference grid must be defined, in which each dimension is discretised (see Figure 4.5). A function of x and t at position i, time t, is written $f(x_i, t_n) = f_i^n$. The partial derivative of $f(x_i,t_n)$ is written $f_x|_i$. Expanding the Taylor series at the base point i for f_{i+1} and f_{i-1}, and subtracting f_{i-1} from f_{i+1} gives rise to an exact expression for the first derivative of f at point i. Truncating this infinite expression generates a finite difference approximation, with an error of the same order as the term at which truncation occurred. This method uses points centred around i, and has been truncated at the second-order term. Hence:

Eq. 4.3 $$f_x|_i = (f_{i+1} - f_{i-1})/2\Delta x + O(\Delta x^2)$$

is a second order, centred-difference formula for $f_x|_i$. Many different FDAs can be derived using the Taylor series method, which can then be substituted for the original PDEs to produce solvable FDEs. There are a number of different techniques for producing FDEs, some of which

are more suited to certain types of PDE than others. The issue of 'stability' is an important consideration, which will be examined in Section 4.2.2.

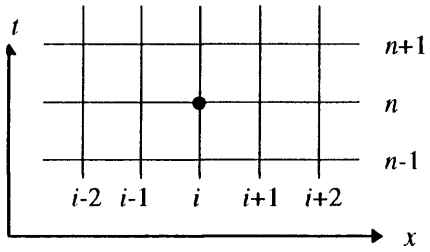

Figure 4.5: Discretisation of x-t space

4.2.1 Finite difference equations used in the model

Eq. 4.4
$$\frac{\partial u}{\partial t} \equiv \frac{u_{i,j}^{n+1} - u_{i,j}^{n-1}}{2\Delta t} \quad \text{(Centred-difference formula)}$$

Eq. 4.5
$$\frac{\partial \eta}{\partial x} \equiv \frac{\eta_{i+1,j}^{n} - \eta_{i,j}^{n}}{\Delta x} \quad \text{(Forward-difference formula)}$$

Eq. 4.6
$$\nabla^2 u = \frac{u_{i+1}^{n-1} - 2u_i^{n-1} + u_{i-1}^{n-1}}{(\Delta x)^2} + \frac{v_{j+1}^{n-1} - 2v_j^{n-1} + v_{j-1}^{n-1}}{(\Delta y)^2} \quad \text{(Centred-difference formula)}$$

Substituting these into Eq. 4.1 and rearranging for u at the next time step (n+1) gives:

Eq. 4.7
$$u_{i,j}^{n+1} = u_{i,j}^{n-1} + 2\Delta t\left[-g\left(\frac{\eta_{i+1,j}^{n} - \eta_{i,j}^{n}}{\Delta x}\right) + f_u \frac{1}{4}\left(v_{i,j} + v_{i+1,j} + v_{i,j-1} + v_{i+1,j-1}\right) + \tau_x + Q + \mu\left(\frac{u_{i+1}^{n-1} - 2u_i^{n-1} + u_{i-1}^{n-1}}{(\Delta x)^2} + \frac{v_{j+1}^{n-1} - 2v_j^{n-1} + v_{j-1}^{n-1}}{(\Delta y)^2}\right)\right]$$

A similar FDE can be found for v. The FDE for Eq. 4.1 is:

Eq. 4.8
$$\eta_{i,j}^{n+1} = \eta_{i,j}^{n-1} - 2\Delta t\left[\left(\frac{1}{2}\left(H_{i+1,j} + H_{i,j}\right)u_{i,j}^{n} - \frac{1}{2}\left(H_{i,j} + H_{i-1,j}\right)u_{i-1,j}^{n}\right)\Big/\Delta x + \left(\frac{1}{2}\left(H_{i,j+1} + H_{i,j}\right)v_{i,j}^{n} - \frac{1}{2}\left(H_{i,j} + H_{i,j-1}\right)v_{i,j-1}^{n}\right)\Big/\Delta y\right]$$

4.2.2 Stability analysis

Assuming the PDE itself has a bounded solution (true for most physical situations), then the FDE is stable if it produces a bounded solution and unstable if it produces an unbounded solution. There are in fact three possibilities:

1. *Unconditionally stable* - the FDE is bounded for all grid spacing values
2. *Conditionally stable* - the FDE is bounded for certain grid spacing values only
3. *Unconditionally unstable* - the FDE is always unbounded, regardless of the grid spacing.

Performing stability analyses on the system of equations used in the model produces two stability criteria (hence, the FDEs are *conditionally stable*). The first of these is the wave equation criterion (Eq. 4.9), derived from analysing the stability of Eq. 4.7, which must be satisfied in order for the model to resolve waves (Press *et al.*, 1986). Its physical meaning is that any waves which occur in the model must not travel the length of a grid box, Δx, faster than the model time step, $2\Delta t$ (factor 2 due to centred-difference scheme), which would imply that the waves were unresolved by the model.

Eq. 4.9 $$\frac{\Delta x}{2\Delta t} > c$$

where c is the phase speed.

The time step, Δt, is chosen such that Eq. 4.9 is satisfied, given the grid size Δx (~3 km) and a maximum phase speed, c. It is possible for barotropic waves to travel at high speeds (approximately 100 m s^{-1}), so Δt is assigned a value of 2 seconds to remove any possibility of instabilities arising.

The second criterion, the diffusion condition (Eq. 4.10), is derived from analysing the stability of the diffusion term $\mu\nabla^2 u$, and must be satisfied in order for the model to resolve diffusion processes across grid cells:

Eq. 4.10 $$\frac{\Delta x^2}{2\Delta t} > \frac{\mu}{\rho}$$

where μ is the diffusion coefficient (viscosity in this case) and ρ is the density. If diffusion is too high, the model is unable to resolve the process and numerical instabilities are likely to occur. Given the values of Δx and Δt, μ can take a wide range of values, from 0 to ~10^5 m^{-2}. Therefore, the choice of μ is dependent on how much viscous drag is required in the model.

The FDA for the diffusion term (Eq. 4.6) uses the time level n-1, as opposed to the more usual method of using level n. The latter scheme is known as the 'leapfrog method' and is unconditionally unstable when used to solve the diffusion equation. However, if n-1 is substituted for n, stability analysis reveals that the scheme is now conditionally stable. This replacement can be justified when diffusion processes take place over time scales small enough for there to be negligible difference between solutions at n and n-1.

In order to eliminate instabilities, the solutions of the system of equations described above need to be 'smoothed' at regular intervals (every NSM time steps). The smoothing takes the form of averaging the solutions between adjacent time levels. e.g. $u^{n+1} = (u^{n+1} + u^{n}) / 2$. As the smoothing frequency increases (NSM decreases) there are fewer irregularities in the solutions. However, if smoothing takes place too often, the solutions become degraded by too much averaging. This is illustrated nicely in Figure 4.6, which shows how the period and amplitude of waves generated in the model change depending on the smoothing frequency NSM. This analysis provides an indication of the upper limit to the smoothing, which in this case should be performed no more than approximately every 10 time steps, or 20 seconds, given by the value of NSM where the period and amplitude curves in Figure 4.6 become flat.

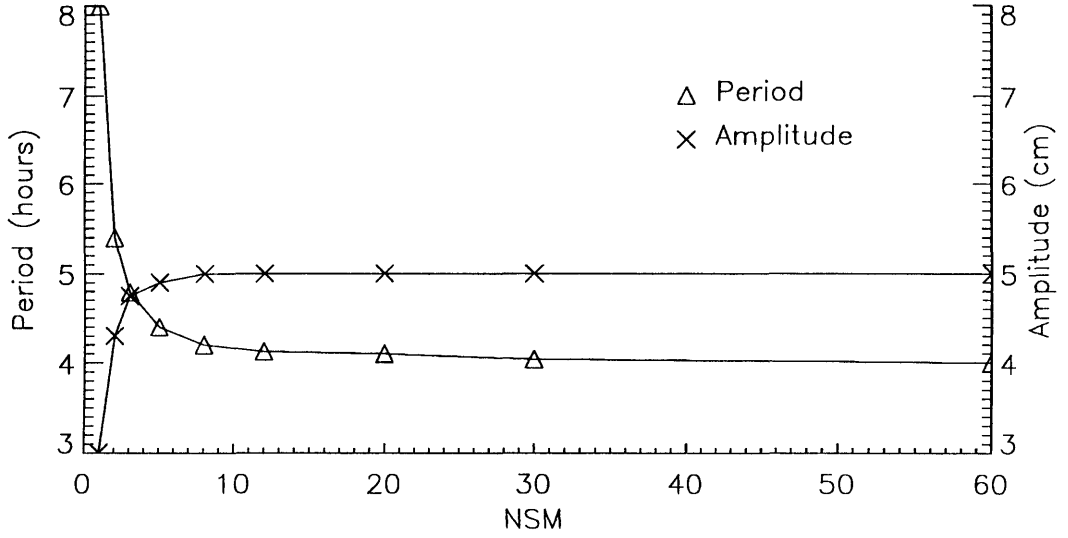

Figure 4.6: Dependency of period and amplitude of seiches on NSM (Number of time steps between smoothing), where one time step = two seconds (temporal resolution used in this model).

4.3 Model initialisation

There are a number of factors which will influence the behaviour of the model, such as wind stress, bathymetry and the presence of sources and sinks. To investigate their effect, each model run varies these parameters. To remove complications due to the irregular shape of the Lake Baikal basin, the model was first run with a simple 130 x 10 rectangular grid. Table 4.1 gives details of each run of the model, and the parameters are described in more detail below:

Wind stress:

Due to the lack of real wind field data for Lake Baikal, the wind forcing analysis in this study is somewhat restricted. In those model runs in which a wind stress is applied, the field is uniform over the whole grid. The strength, direction and duration of the wind is varied in each model run.

Wind stress, $\tau = \rho_{air} \times c_D \times |u| \times u$ Nm^{-2}

where u is the wind speed in ms^{-1}, ρ_{air} = 1.2 Kg m^{-3}, c_D = 1.5 x 10^{-3} and is the drag coefficient. For example, a wind speed of 10 ms^{-1} gives rise to a wind stress on the surface of 0.18 Nm^{-2}.

In the case of 'No wind' model runs the term τ in Eq. 4.7 is set to zero.

Sources/sinks:

There are four major rivers in the Lake Baikal basin; the Upper Angara (UAR), Barguzin (BR), Selenga (SR) and Lower Angara (LAR) rivers. The Lower Angara is the only outflow from the lake, and the other three contribute (in varying proportions) 70% of the water flowing in. Around 300 others contribute the remainder, and are mostly spread along the south-east coast. For simplicity, the annual river input (~$6x10^7$ m^3) is divided between the three major rivers. For use in the model, the volume flux for each river must be converted to a rate of change of height at a specified grid point (i.e. the location of the river mouth). The conversion factor is:

(Percentage contribution x Total input x Conversion to cm^3 s^{-1}) / (Surface area of grid box)

The conversion to cm^3 s^{-1} is required as the model uses cgs units. Sources UAR, BR and SR, when taken to be the only contributories, provide 72%, 19% and 9% respectively (Kozhov, 1963). LAR is 100% sink. An important point to note is that the surface area of each grid box is slightly different, due to the reduction in grid box width Δx with increasing latitude. Use of a constant grid box area results in an overall increase or decrease in the total surface height. In the extreme, this causes the lake to apparently 'fill up' or 'empty'.

For model runs with 'No sources/sinks' the source term Q in Eq. 4.7 is set to zero, so there is no addition or removal of mass from the system.

Viscosity:

The stability criterion Eq. 4.10 restricts the viscosity, μ, to a value between 0 and 10^5 m^{-2}, for the given grid spacing and time step. This provides a wide latitude for studying the effect of varying the viscosity from the actual value of $1.6x10^{-6}$ m^{-2} (Dorsey, 1968). Increasing the viscosity is likely to have a considerable effect on the motion of water.

In addition to varying the viscosity over the whole grid, cells along the boundaries can be given an increased viscosity to simulate friction along the coasts.

For the case of 'No boundary viscosity' model runs a constant viscosity is assigned to the whole grid.

Coriolis force:

The Coriolis force arises due to the rotation of the Earth. It has the effect of turning currents to the right, in the Northern hemisphere, and is likely to have a major impact on the flow of water in Lake Baikal.

The force acting on a water particle with mass m and speed u is given by:

Eq. 4.11 Coriolis force = $2\ \Omega\ sin\ (\Phi)\ m\ u$

where Ω is the angular velocity of the Earth and Φ is the latitude. The term $2\ \Omega\ sin\ (\Phi)$ is referred to as the Coriolis parameter, f.

In the case of 'No Coriolis force' model runs the Coriolis parameter is set to zero to remove the effect of the Earth's rotation on the current flow.

Bathymetry:

A realistic bathymetry was obtained from a contour map of the lake, by overlaying the model grid onto the map and finding the depth at the H-points, at a resolution of 100 m (as shown in Figure 1.1).

In each model run, the equilibrium depth, H, was specified as being either the realistic bathymetry ('Baikal') described above, or a constant depth ('Flat'), to investigate how the flow of water is affected by different topographies. The calculated mean depth of the model 'Baikal' bathymetry is 705 m (close to the mean depth of the real lake, 680 m).

4.4 Results

4.4.1 Wind stress

When the surface of the lake is forced with a wind stress (model runs Tn and Wn), a standing wave along the length of the lake is observed. These oscillations, known as seiches, are naturally occurring phenomena, and have been observed frequently in Lake Baikal (Kozhov, 1963; Dean and Dalrymple, 1984). The theoretical period of these seiches depends on the length and depth of the basin, and is given by the Merian formula (Dean and Dalrymple, 1984):

Eq. 4.12 $$T_{th} = \frac{2l}{\sqrt{gh}}$$

where l is the basin length, h is the basin depth and g is acceleration due to gravity.

Table 4.1: Details of each model run, to investigate the effect of varying different parameters, such as wind strength, direction and duration, basin bathymetry and depth, and viscosity.

Run name	Details
Test run with simple rectangular basin (56 x 455 km):	
T1	Winds, no sources/sinks, no boundary viscosity, no Coriolis force. τ = 0.5 Nm^{-2}, W, 2 hours. μ = 0. Bathymetry = 'Flat', depth = 407 m.
T2	Winds, no sources/sinks, no boundary viscosity, no Coriolis force. τ = 0.5 Nm^{-2}, W, 6 hours. μ = 0. Bathymetry = 'Flat', depth = 407 m.
T3	Winds, no sources/sinks, no boundary viscosity, no Coriolis force. τ = 0.5 Nm^{-2}, W, 4 hours. μ = 0. Bathymetry = 'Flat', depth = 407 m.
T4	Winds, no sources/sinks, no boundary viscosity, no Coriolis force. τ = 0.5 Nm^{-2}, W, 2 hours. $\mu = 10^5$ m^{-2}. Bathymetry = 'Flat', depth = 407 m.
T5	Winds, no sources/sinks, no boundary viscosity, Coriolis force. τ = 0.5 Nm^{-2}, W, 2 hours. μ = 0. Bathymetry = 'Flat', depth = 407 m.
T6	Winds, no sources/sinks, no boundary viscosity, Coriolis force. τ = 0.5 Nm^{-2}, S, 2 hours. μ = 0. Bathymetry = 'Flat', depth = 75 m.
Investigation of the effect of wind stress (Lake Baikal land mask):	
W1	Winds, no sources/sinks, no boundary viscosity, no Coriolis force. τ = 0.4 Nm^{-2}, SW, 2 hours. $\mu = 1.6x10^{-6}$ m^{-2}. Bathymetry = 'Baikal'.
W2	Winds, no sources/sinks, no boundary viscosity, no Coriolis force. τ = 0.4 Nm^{-2}, SW, 4 hours. $\mu = 1.6x10^{-6}m^{-2}$. Bathymetry = 'Flat', depth = 200 m.
W3	Winds, no sources/sinks, no boundary viscosity, no Coriolis force. τ = 0.4 Nm^{-2}, SW, 2 hours. $\mu = 1.6x10^{-6}$ m^{-2}. Bathymetry = 'Flat', depth = 705 m.
W4	Winds, no sources/sinks, no boundary viscosity, no Coriolis force. τ = 0.8 Nm^{-2}, SW, 2 hours. $\mu = 1.6x10^{-6}$ m^{-2}. Bathymetry = 'Flat', depth = 705 m.
W5	Winds, no sources/sinks, no boundary viscosity, no Coriolis force. τ = 0.4 Nm^{-2}, SW, 4 hours. $\mu = 1.6x10^{-6}$ m^{-2}. Bathymetry = 'Flat', depth = 705 m.
W6	Winds, no sources/sinks, no boundary viscosity, no Coriolis force. τ = 0.1 Nm^{-2}, NW, 2 hours. $\mu = 1.6x10^{-6}$ m^{-2}. Bathymetry = 'Flat', depth = 705 m.
W7	Winds, no sources/sinks, no boundary viscosity, Coriolis force. τ = 0.1 Nm^{-2}, NW, 2 hours. $\mu = 1.6x10^{-6}$ m^{-2}. Bathymetry = 'Flat', depth = 705 m.
W8	Winds, no sources/sinks, no boundary viscosity, no Coriolis force. τ = 0.1 Nm^{-2}, NW, 2 hours. $\mu = 1.6x10^{-6}$ m^{-2}. Bathymetry = 'Baikal'.
W9	Winds, no sources/sinks, no boundary viscosity, Coriolis force. τ = 0.1 Nm^{-2}, NW, 2 hours. $\mu = 1.6x10^{-6}$ m^{-2}. Bathymetry = 'Baikal'.
Investigation of effect of varying the viscosity (Lake Baikal land mask):	
V1	Winds, no sources/sinks, no boundary viscosity, no Coriolis force. τ = 0.4 Nm^{-2}, SW, 2 hours. $\mu = 10^8$. Bathymetry = 'Baikal'.
V2	Winds, no sources/sinks, boundary viscosity, no Coriolis force. τ = 0.4 Nm^{-2}, SW, 2 hours. μ = 0.016; 10^8 (edge). Bathymetry = 'Baikal'.
Investigation of the effect of adding sources and sinks (Lake Baikal land mask):	
S1	No winds, sources/sinks, no boundary viscosity, no Coriolis force. $\mu = 1.6x10^{-6}$ m^{-2}. Bathymetry = 'Baikal'.
S2	No winds, sources/sinks, no boundary viscosity, Coriolis force. $\mu = 1.6x10^{-6}$ m^{-2}. Bathymetry = 'Baikal'.
S3	No winds, sources/sinks, boundary viscosity, no Coriolis force. $\mu = 1.6x10^{-6}$ m^{-2}; 10^4 m^{-2} (edge). Bathymetry = 'Baikal'.
S4	No winds, sources/sinks, boundary viscosity, Coriolis force. $\mu = 1.6x10^{-6}$ m^{-2}; 10^4 m^{-2} (edge). Bathymetry = 'Baikal'.
Combinations of the above (Lake Baikal land mask):	
C1	Winds, sources/sinks, no boundary viscosity, Coriolis force. τ = 0.4 Nm^{-2}, NW, 2 hours. $\mu = 1.6x10^{-6}$ m^{-2}. Bathymetry = 'Baikal'.

Although Eq. 4.12 applies to the simple case of a rectangular basin of constant depth, Lake Baikal can be approximated to be a rectangular basin of length 640 km with a mean depth of 700 m (Kozhov, 1963). Using these parameters the theoretical period of Lake Baikal is 4.29 hours, which is considerably different to the observed periods of 4.64 hours (Dean and Dalrymple, 1984) and 4.85 hours (Kozhov, 1963). This discrepancy could be attributed to the irregularity in the shape of the lake and the topography of the basins, and is investigated here.

In order to study the seiches generated by the model, plots of the surface height at points at each end of the lake were analysed. To begin with, the model was run using a simple rectangular basin, 455 km east to west and 56 km south to north, with a depth chosen so that the period of oscillations was 4 hours, for simplicity. Eq. 4.12 gives a depth of 407 m for l = 455 km and T_{th} = 4 hours. After this simple basin was analysed, the Baikal land mask was applied, using both flat basin and realistic bathymetry (see Table 4.1 for details of each model run).

Figure 4.7 shows the results for model runs T1-T5 (rectangular basin). It is evident from these plots that for a seiche to develop, the wind stress, τ, must be applied to the surface for a time equal to at least half the period of oscillations, T, which is the time taken for the initial wave to travel the length of the basin. If the wind stress stops at this point oscillations continue with period T and amplitude A. However, if τ continues after this time the surface continues to oscillate as before, but around an equilibrium height of $A/2$. i.e. surface displacement over a range h = 0 to A. If τ stops after a time $t = nT$ (where n is an integer) there is a cancelling effect between the wave generated directly by the wind stress and the wave returning from the opposite end of the basin. The amplitude of the oscillations is then reduced to the level at which the stress stopped (approximately zero in the case of model run T3). If τ stops at $t = (n + 1/2)T$, a normal seiche develops with oscillations continuing with period T and amplitude A (T2). A wind stress which is applied for a time other than this will result in a seiche with an amplitude less than A (approximately the amplitude of the wave at the time the wind ceased). As the viscosity, μ, is increased (T4) the seiche oscillations are damped, becoming progressively weaker with time. Model run T5 has the Coriolis force included, but this has no apparent effect on the seiche motion. However, when a basin aligned in a south-north direction is used, with a southerly wind stress, the Coriolis effect causes a rotation of the seiche wave. This is known as a Kelvin wave, and would not be as noticeable for a basin with its long axis aligned in the direction of the Earth's rotation. The period, T, remains constant at 4 hours for all model runs. The excellent agreement between T_m and T_{th}, and the appearance of Kelvin waves, is good validation that the model is working correctly.

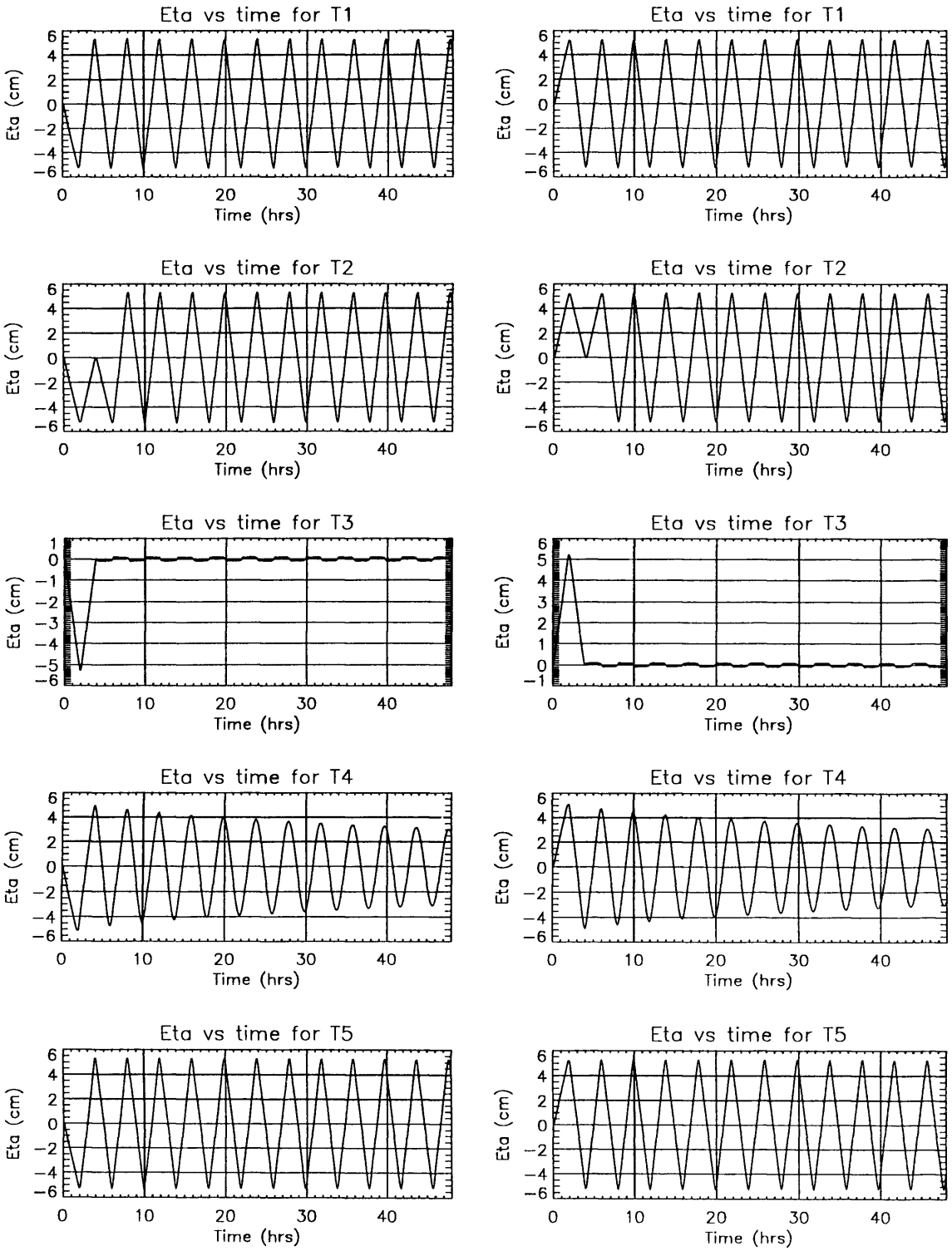

Figure 4.7: Plots of surface displacement, η, for model runs T1 - T5. Left: at a grid point at the west end; Right: at a grid point at the east end of the basin.

Table 4.2 gives the results obtained for model runs Wn, with the measured model period (T_m), theoretical period (T_{th}) for the depth used (as given by Eq. 4.12) and the maximum amplitude at a grid point (40,15) in the South basin. The model lake is approximately 640 ± 10 km in length. The error in the length is due to the uncertainty in knowing exactly how the length should be measured, since a straight line cannot be made along the irregularly shaped lake. This gives rise

to a small uncertainty (about 0.1 hours) in the theoretical period. The error in the measured period is due to the data output frequency of 0.05 hours.

Table 4.2: Results from model runs investigating seiche oscillations.

	W1	W2	W3	W4	W5
T_m (hours)	4.65 ± 0.05	8.0 ± 0.05	4.25 ± 0.05	4.25 ± 0.05	4.27 ± 0.05
T_{th} (hours) (l=640 ± 10 km)	4.28 ± 0.08	8.03 ± 0.12	4.28 ± 0.08	4.28 ± 0.08	4.28 ± 0.08
Max amp (cm) at (40,15)	5.0 ± 0.1	16.0 ± 0.1	4.7 ± 0.1	9.5 ± 0.1	0.9 ± 0.1

Plots of surface displacement at two grid points (South and North basin of the lake) can be seen in Figure 4.8. The results for model runs W2 to W5 show that there is excellent agreement, within error, between the measured (T_m) and theoretical (T_{th}) seiche periods. However, T_m and T_{th} for W1 (which uses the realistic bathymetry) are considerably different, as expected given the observed data on the lake. Since Eq. 4.12 is strictly only valid for rectangular basins with a uniform depth, as noted above, some discrepancy is to be expected. The agreement between T_m for W1 and measurements of Lake Baikal itself (4.64 - 4.85 hours) are, however, extremely good.

A secondary oscillation, with a period of about 30-35 hours, can also be seen in Figure 4.8. This behaviour is not seen in the results for the model runs T*n*, which have a regular, rectangular basin. It is therefore likely to be due to the irregular shape of the lake causing reflections from different boundaries.

The amplitude of the oscillations is clearly affected by the strength and duration of the wind stress. A factor two increase in wind stress results in a two-fold increase in amplitude (model runs W3 and W4). Decreasing the basin depth also has the effect of increasing the maximum amplitude. As with the rectangular basin model runs (T*n*), the effect of wind stress duration on the oscillations is dramatic. If the wind stress ceases after a time equal to T_{th}, a seiche is still generated but at a much reduced amplitude, caused by the cancellation between the wind-induced wave and the wave returning from the opposite end of the basin. Thus the amplitude of a seiche only increases with the strength of the wind, not its duration, although there is an optimum duration, equal to T_{th}, required for seiche generation.

Looking at the plots for W1 and W10, the inclusion of the Coriolis force has no clear impact on the model results. Contour plots of the surface do, however, show some indication of rotation of the seiche, although not as clearly as in the T*n* model runs.

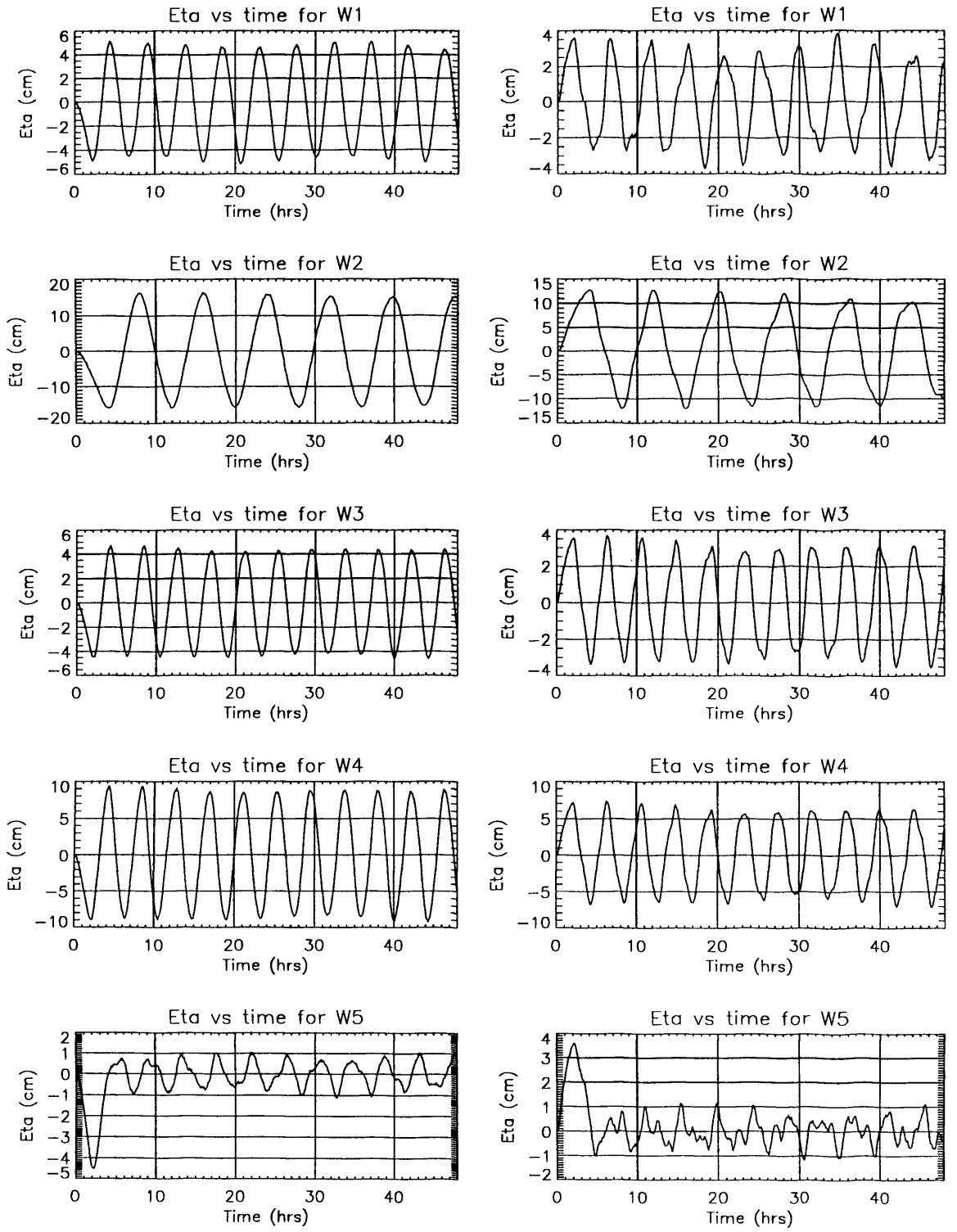

Figure 4.8: Plot of surface displacement, η, at two grid points, for model runs W1 - W5. Left: South basin; Right: North basin.

4.4.2 Viscosity

Increasing the viscosity of the model fluid damps wind-induced seiches, as can be seen in the results for the V*n* model runs (Figure 4.9). Increasing the viscosity over the whole lake to 10^4 m^{-2} (V1) damps out the oscillations after about 2 days. Introducing an increased boundary viscosity (V2) also damps the oscillations, but takes a few hours longer than V1 to damp them out completely.

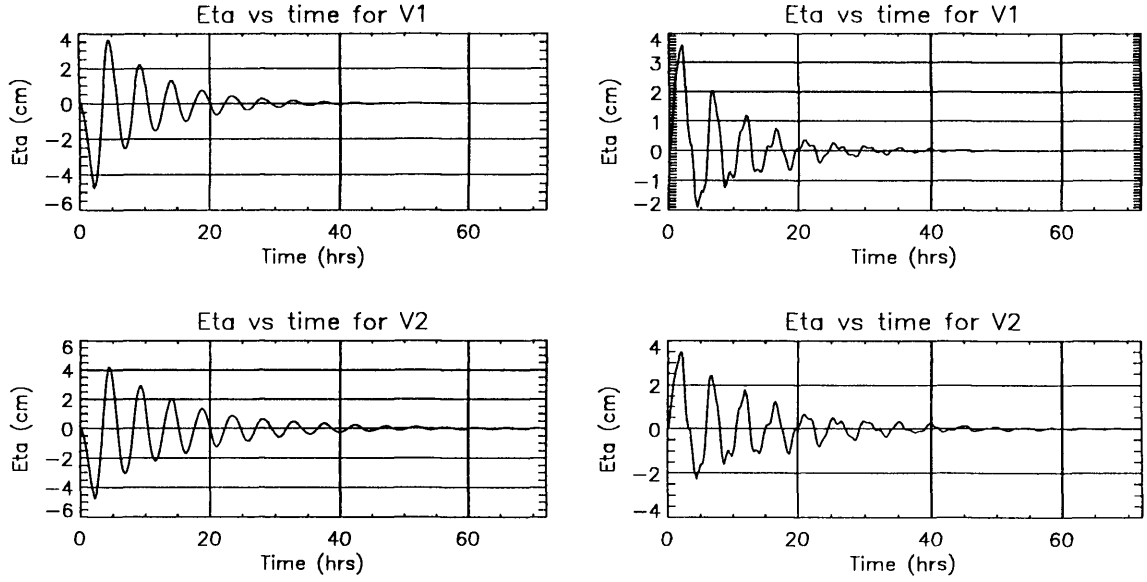

Figure 4.9: Plot of η at two grid points, for model runs V1 - V2. Left: South basin; Right: North basin.

4.4.3 River inflow/outflow

To investigate how the current flow is affected by different conditions (Coriolis force, viscosity etc.), results were compared for each of the model runs (see Table 4.1 for details).

S1:

Currents flow directly from the Selenga River source to the Lower Angara River sink, with speeds of around $3x10^{-5}$ ms^{-1} (see Figure 4.10). Currents in the Central and North Basin have no predominant direction and are relatively weak compared to the flow in the South Basin. Low amplitude ($3x10^{-3}$ m) waves formed along the southern edge of the South Basin. Note that in Figure 4.10 and the following figures showing current flow in the model, arrows indicate relative speed and direction of mass transfer at each grid point, and those which appear to show flow over land are an artefact of the plotting method.

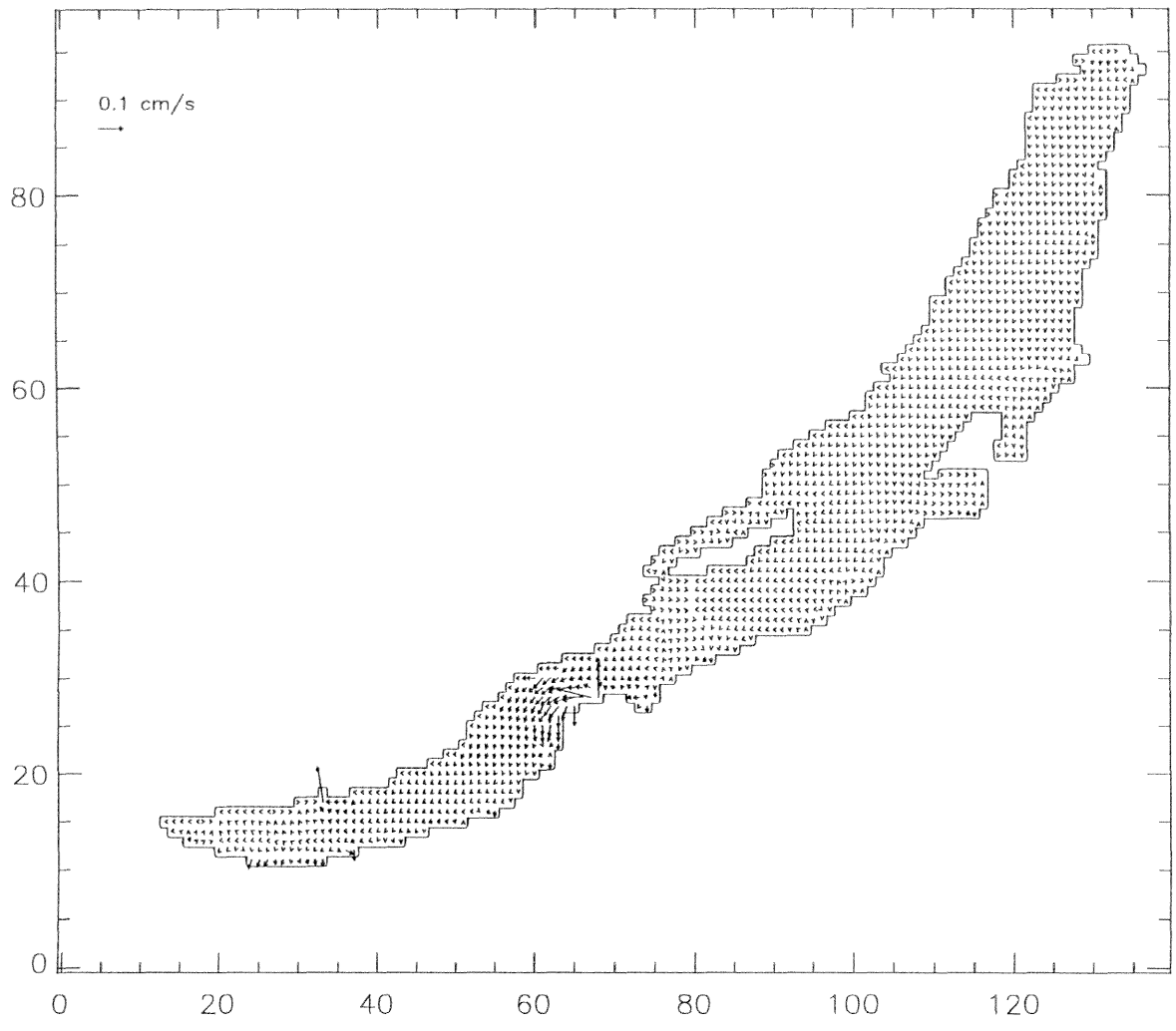

Figure 4.10: Velocity field for model run S1 after 6 hours. Current flow is primarily in a south-west direction from the Selenga Delta towards the Lower Anagara River outflow. Current speeds in this region are of the order 10^{-3} ms^{-1}, decreasing to 10^{-5} ms^{-1} further from the Delta.

S2:

With the Coriolis force included there is a considerable change in the pattern of current flow. There is now not such a direct flow from the Selenga to the Lower Angara, with some flow from the Selenga turning to the north-east (see Figure 4.11). Typical current speeds in the region of the Selenga are about $2x10^{-3}$ ms^{-1}, similar to those in S1.

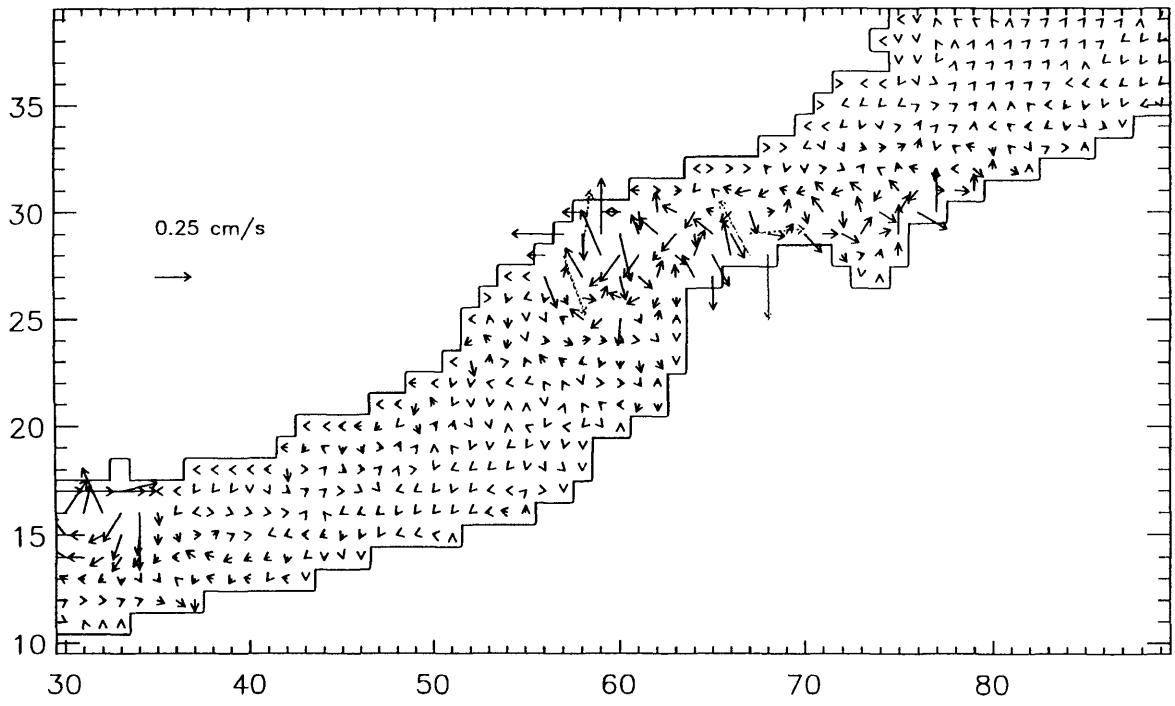

Figure 4.11: Velocity field in the Selenga Delta region for model run S2 after 28 hours. Grey arrows denote grid boxes where current speed is in excess of $4x10^{-3}$ ms^{-1}, given a fixed length for clarity.

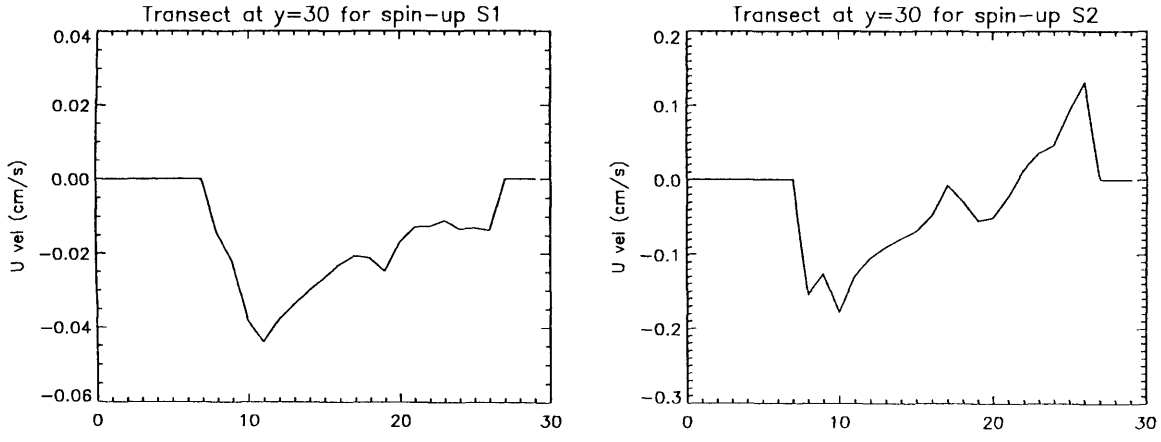

Figure 4.12: Transect of *u* velocity at y = 30 (Selenga Delta region) after 10 hours for S1 and S2. The *x*-axis represents grid-cell number along the transect, from west (left) to east (right).

Figure 4.12 shows a plot of the *u* velocity along a transect just to the north of the Selenga (y=30) for S1 and S2, clearly showing flow to both the east (positive *u*) and west (negative *u*) for S2 but flow wholly to the west for S1.

S3:

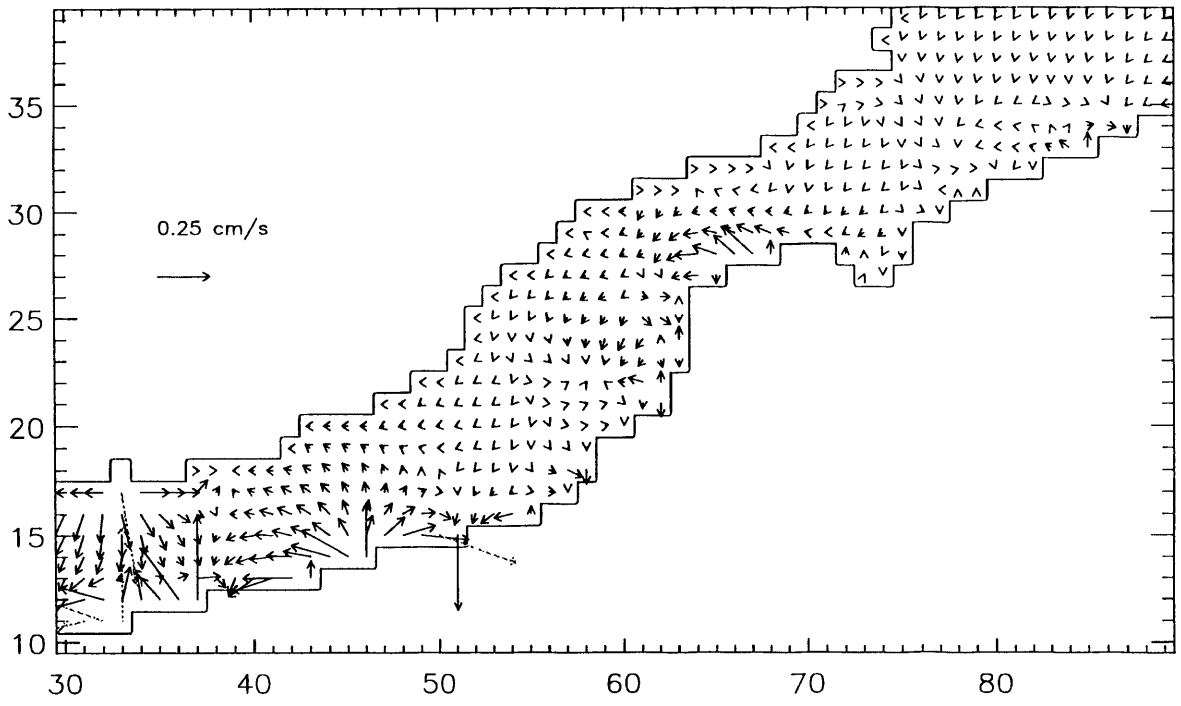

Figure 4.13: Velocity field in the Selenga Delta region for model run S3 after 28 hours. Grey arrows denote grid boxes where current speed is in excess of $4x10^{-3}$ ms^{-1}, given a fixed length for clarity.

There is little difference between S1 and S3 (which has an increased boundary viscosity), except that the waves along the southern edge in the S3 model run grow in amplitude over time (which can be seen at the lower left edge of Figure 4.13). This may be a numerical instability caused by the difference in viscosities, and suggests that this may not be a suitable method to use. Current speeds are similar to those in S1.

S4:

Although this model run includes the Coriolis force, there is no flow to the right from the Selenga as was observed in S2. This run most closely resembles S3, and also develops waves along the southern coast which grow with time.

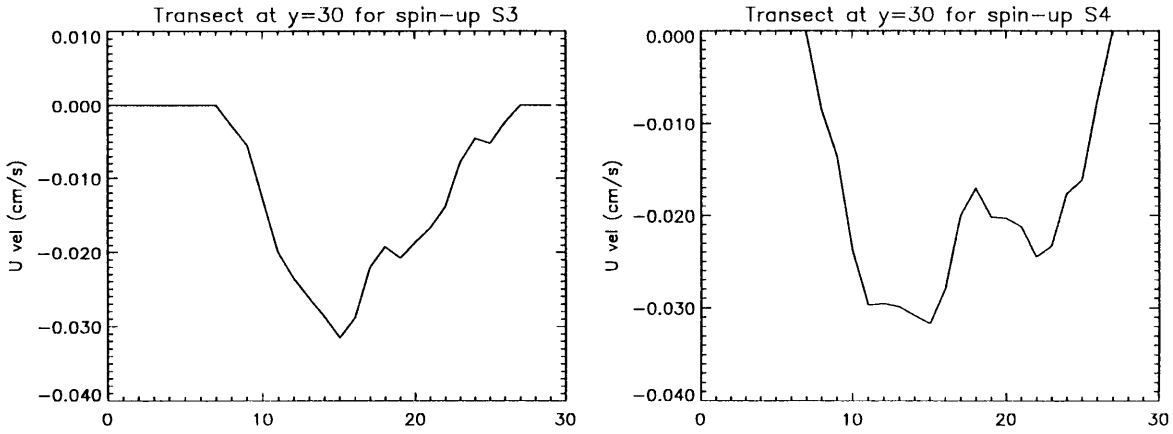

Figure 4.14: Transect of *u* velocity at y = 30 (Selenga Delta region) after 10 hours for S3 and S4. The *x*-axis represents grid-cell number along the transect, from west (left) to east (right).

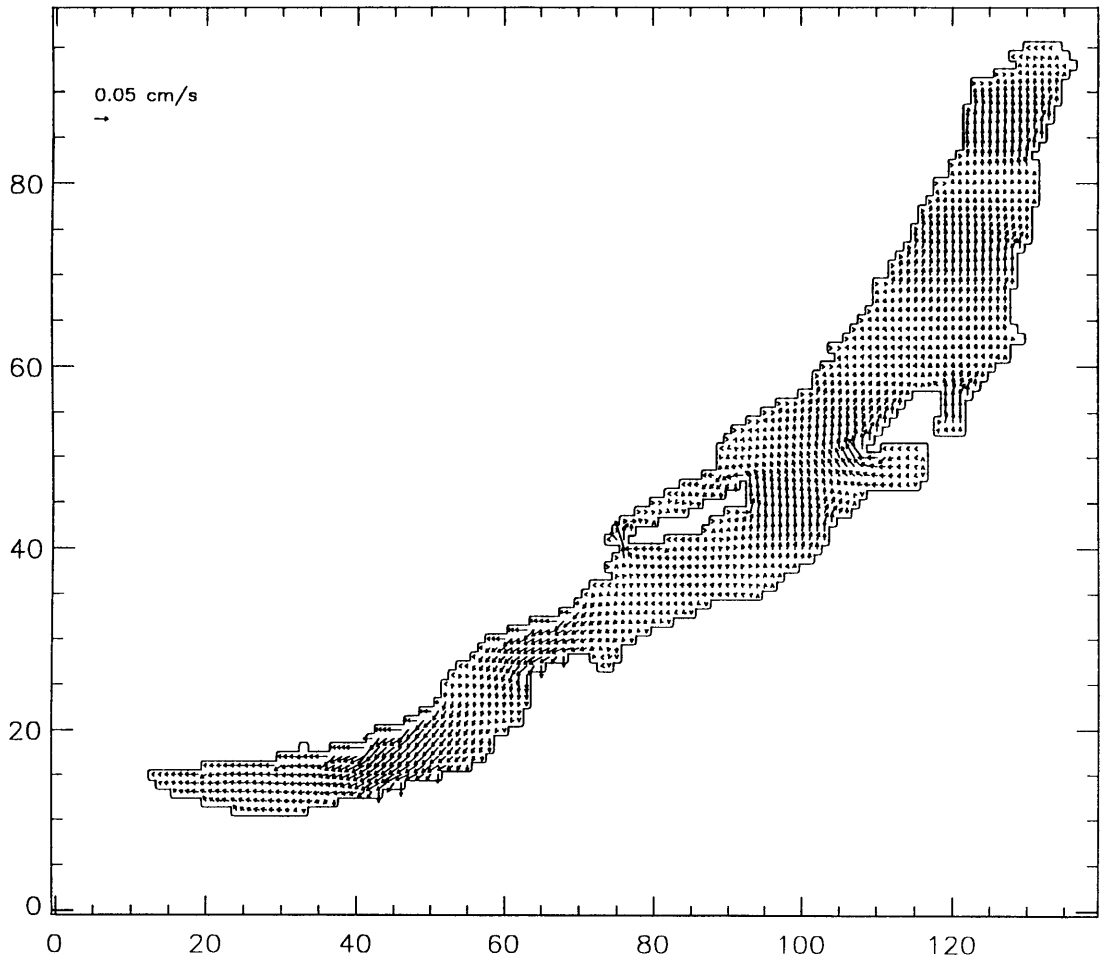

Figure 4.15: Velocity field for model run W6 after 2 hours. Current speeds are of the order 5×10^{-4} ms^{-1}.

W6 and W7:

The applied north-west wind stress results in oscillations of the surface, but a seiche does not develop as in the model runs where the wind direction was aligned along the long axis of the basin. Current speeds are of the order 10^{-4} ms^{-1}, and depend on the surface displacement. The addition of the Coriolis force (W7) causes no apparent difference between the two model runs.

W8:

Changing the flat basin topography to a realistic one dramatically influences the flow patterns. Current speeds are increased where the basin becomes shallow, such as along the coasts, at the Selenga Delta and above the Academician Ridge (Figure 4.16).

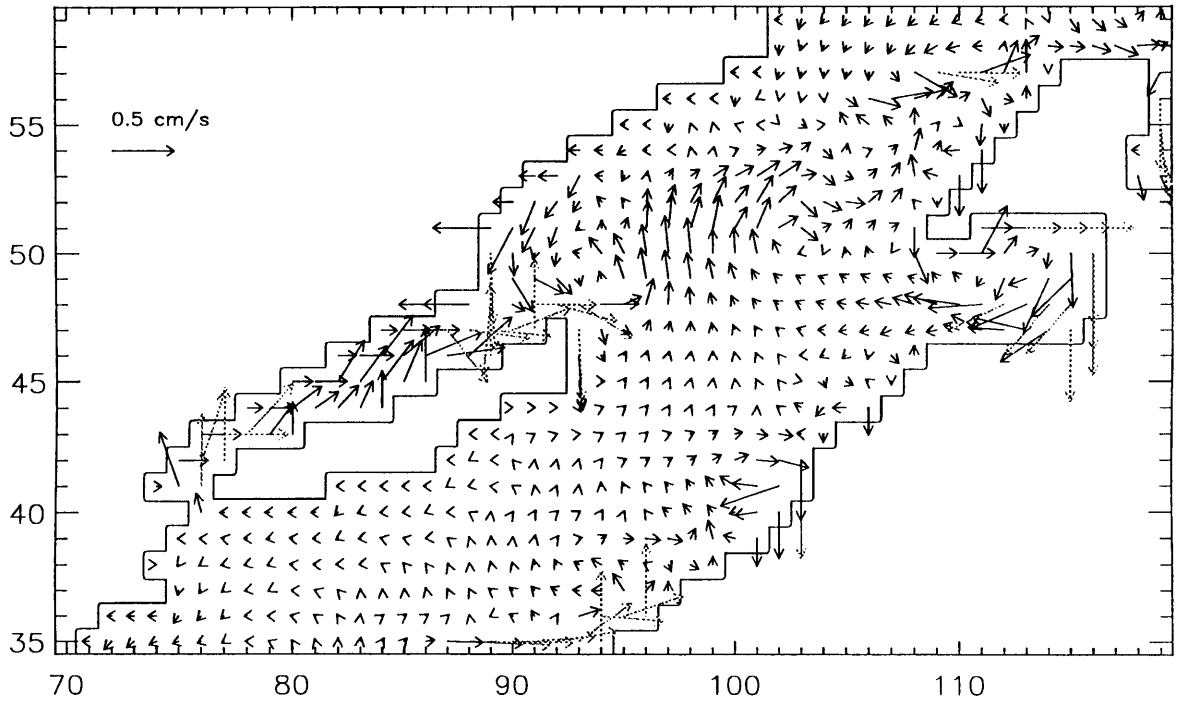

Figure 4.16: Velocity field for W8 in the region of the Academician Ridge after 55 hours. Grey arrows denote grid boxes where current speed is in excess of $5x10^{-3}$ ms^{-1}, given a fixed length for clarity. Current speeds are fastest in regions where the basin depth is shallow, such as along the Academician Ridge, in Barguzin Bay and around Olkhon Island.

W9:

With the inclusion of the Coriolis force a very interesting effect occurs. The flow above the Academician Ridge, which was fairly constant over time for W8, has developed an eddy-like nature. Figure 4.17 clearly shows a clockwise circular flow pattern above the middle of the ridge. This moves over time in a south-westerly direction from just to the north-west of Svyatoi Nos Peninsula to the north-east end of Olkhon Island.

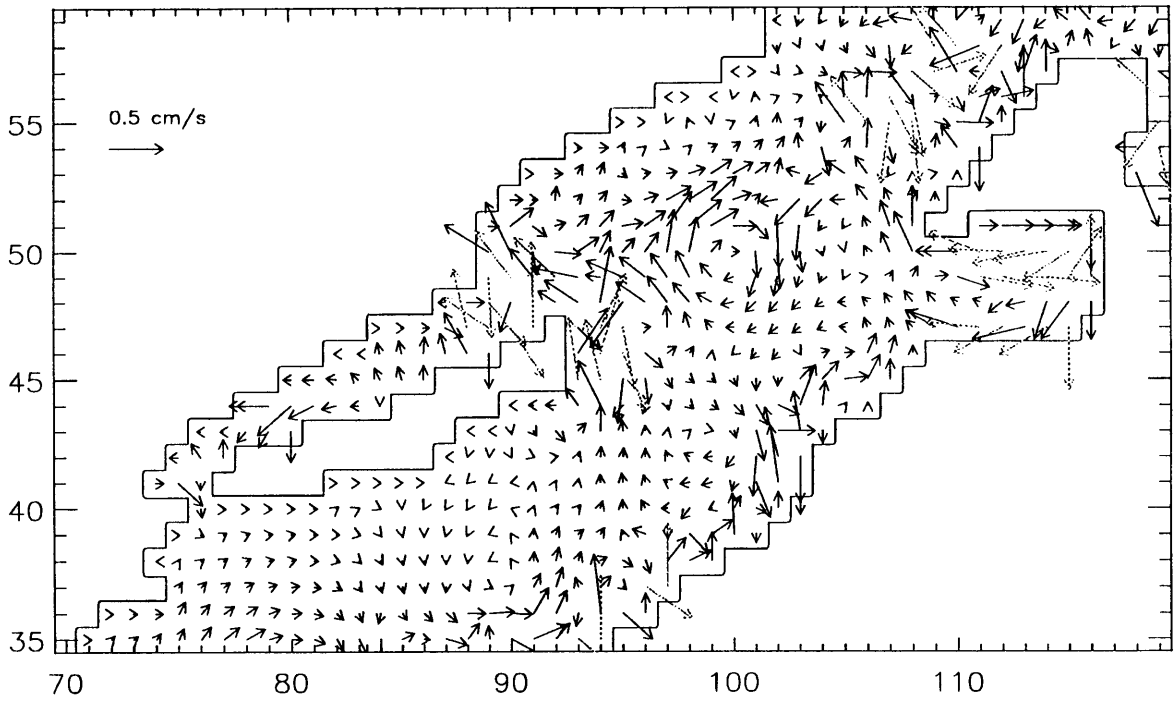

Figure 4.17: Velocity field for W9 in the region of the Academician Ridge after 55 hours. Grey arrows denote grid boxes where current speed is in excess of $5x10^{-3}$ ms^{-1}, given a fixed length for clarity. Currents between Olkhon Island and the Svyatoi Nos Penninsula flow in a spiral manner due to the introduction of the Coriolis force in this model run.

C1:

Flow in this model run is mostly due to the effect of the wind stress, rather than the sources and sinks. Current speeds due to river inflow in the model are one to two orders of magnitude smaller than currents due to wind-driven motion. There is therefore very little difference between C1 and W9, the only modification to the current being in the immediate vicinity of the sources and sinks. Eddy structures above the Academician Ridge are also observed, as in W9.

4.5 Summary and discussion

Results from model runs T1-6 and W1-5 reproduce wind-induced seiches, with periods of oscillation in excellent agreement with those predicted by theory when the model basin has a flat bathymetry. When the realistic topography is introduced the period differs from theory, but agrees with the observations made on Lake Baikal itself. This suggests that bottom topography is an important factor in seiche oscillations, and confirms that the Merian formula cannot be used to predict the period of seiches in non-flat basins, as expected. The non-rectangular shape of the lake does not have a significant effect on the seiche period, although it does introduce a secondary oscillation. This analysis is good evidence that the model is working correctly.

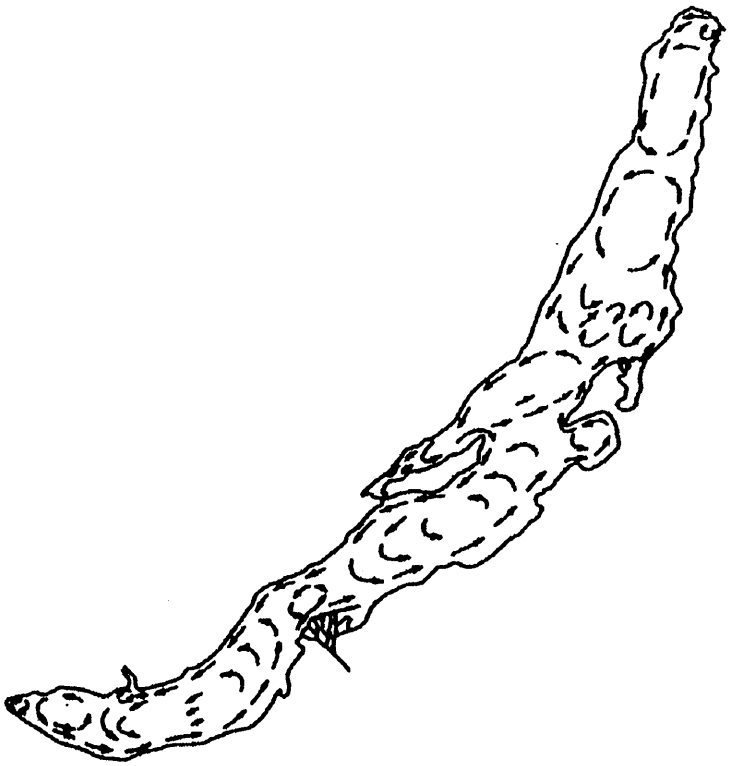

Figure 4.18: Mean water circulation in Lake Baikal, according to automatic recorder data in the 10-15 m layer. Arrows represent current directions. (Shimaraev *et al.*, 1994)

An example of circulation patterns occurring in Lake Baikal can be seen in Figure 4.18. Each basin tends to contain one or more cyclonic (anti-clockwise) circulation cells. Model runs with the Coriolis force absent (forced by sources and sinks only) failed to reproduce these flow patterns, the water flowing directly from the three sources to the Lower Angara River sink. Introducing the Coriolis force shows an improvement, with some flow to the north-east, but the circulation cells are still not reproduced. The Coriolis force clearly has a strong influence on current flow, however. Current speeds are about two orders of magnitude smaller than those observed in the lake.

Eddy-like flow patterns were observed in the region of the Academician Ridge, between the Central and North Basins. These were only observed in model runs which included an initial north-westerly wind stress, realistic bottom topography and the Coriolis force. The first stage in their formation is the flow of water over the ridge in a perpendicular direction, caused by the wind stress. As the water moves from a deep part of the lake over the relatively shallow (~300 m) ridge, the flow is compressed thus moving at a faster speed. This is observed in model run W8, where currents flow more quickly in the shallower parts of the lake. The 'curled' shape of the flow is due to the gradient in the surface height displacement giving rise to a pressure gradient which forces the flow away from the boundary of the lake. The Coriolis force acts in a direction

perpendicular and to the right (in the Northern Hemisphere) of the flow. This results in the formation of the observed eddy structure.

The eddies are unlike the gyres observed in satellite data, however, as they are constantly moving along the ridge, rather than remaining in the same place for many weeks. Analysis of the value of each term in Eq. 4.1 reveals that the Coriolis term is considerably smaller than the pressure gradient term, which suggests that geostrophic equilibrium ($du/dt = 0$) is not occurring, as it would if the structure were a 'true' gyre. What the model does show is the tendency for eddy-like structures to form in the region of the Academician Ridge, and that the primary factor in their generation is the steep ridge between the North and Central basins.

5. Multi-layer baroclinic model

5.1 Overview

In this chapter a three-dimensional numerical model is introduced, developed for the purpose of investigating hydrodynamic processes in Lake Baikal. Particular emphasis is given to the four to five month period when the lake is completely ice-covered. During this time observed currents can be unusually strong (around 0.1 m s^{-1}), considering the absence of river inflow (due to freeze-up of the rivers) and the restricted influence of wind stresses on the surface due to ice cover (Jewson, personal correspondence). The model is used to determine whether density driven flow caused by non-uniform solar heating through the ice and snow could be sufficient to generate the observed current strengths.

The generation of a thermobaric instability (as discussed in Chapter 1) is also investigated. This is thought to be one of the processes involved in deep water ventilation, and may arise due to the formation of baroclinic internal waves on the interface which occurs at the mesothermal temperature maximum, at a depth around 250 m.

These problems are discussed in more detail in section 5.2 below, followed by an overview, in section 5.3, of the numerical model used to investigate them. Section 5.4 gives details on the methods by which certain physical processes in the lake are parameterised, or represented, in the model. These include solar heating, the ice and snow layer, and convective and turbulent mixing. Initialisation conditions for the vertical structure of the model are described in section 5.5, followed by details of the different model runs investigating under-ice currents in section 5.6. Results from these runs are presented in sections 5.7 to 5.11. An investigation into the generation of internal waves in the model is given in section 5.12.

5.2 Introduction to the problems

Current flow affects diatom suspension and the distribution of nutrients within the lake. Resuspension of diatoms is governed by mixing processes in the upper 100-200 m, due to the non-motile nature of the diatoms. Temperature profiles provide an indication of the extent and depth of mixing, which is highly sensitive to variations in snow and ice thickness. Diatom populations beneath snow-covered ice are known to be considerably lower than beneath snow-free ice where convective mixing due to solar heating can occur. The model is used in conjunction with satellite data of Lake Baikal (from Chapter 3) to determine the effect of variations in snow

and ice cover on temperature profile development, which could be used as an indication of diatom population levels.

The generation of thermobaric instability is investigated, as this is thought to be one of the processes involved in deep water ventilation, and may arise due to the formation of baroclinic internal waves on the interface which occurs at the mesothermal temperature maximum, T_{mm} (Carmack and Weiss, 1991). These waves can be caused by strong winds and have been observed in the lake. In order to generate the instability, however, the amplitude of the internal wave must be considerable. The depth to which the interface must be depressed can be determined as follows:

The temperature of maximum density at depth z is given by:

Eq. 5.1 $$T_{md} = -0.0021\, z + 3.98\ ^{\circ}C$$

The compensation depth, H_c, is the depth at which the water column becomes neutrally stable, allowing the thermobaric instability to occur. At this depth the temperatures of the upper and lower layers (T_1 and T_2 respectively) are equidistant from the temperature of maximum density, giving rise to Eq. 5.2 below:

Eq. 5.2 $$T_2 - T_{md} = T_{md} - T_1$$

Combining Eq. 5.1 and Eq. 5.2 results in the following expression for the compensation depth:

Eq. 5.3 $$H_c = (0.5(T_2 + T_1) - 3.98) / -0.0021 \text{ m}$$

Assuming an upper layer temperature of 3°C and a lower layer temperature of 3.35°C, the compensation depth H_c is 384 m. Given that the interface occurs at around 200-300 m, this requires the internal wave to have an amplitude of between 80 and 180 m. However, waves of this amplitude have never been observed in the lake, even after prolonged storms with high winds. The numerical model is, therefore, used to determine whether large amplitude waves are actually possible.

5.3 Overview of the model

The model described in this chapter has been developed from a two-layer baroclinic 'intermediate level' model of a geophysical fluid system (McCreary and Anderson, 1991). It has been extended to N layers, where N is an integer (limited only by considerations of computation time). The barotropic mode has also been introduced.

As with the barotropic model described in the previous chapter, the equations of motion are solved at grid points specified by a 'lake mask', with a spatial resolution of 0.05° x 0.05° (approximately 3.5 x 5.5 km, dependent on latitude). The form of these equations is, however, slightly different. The pressure gradient equation is now determined by changes in density, in addition to surface height displacement, so that the baroclinic mode can be resolved. The original

McCreary and Anderson (1991) model effectively removes the barotropic mode by calculating density *perturbations*, rather than the absolute density. The barotropic mode is re-introduced here, which produces more realistic results, albeit at the expense of a increased computation time (see below). This method is therefore unsuitable for model runs requiring a long integration time (e.g. more than a few months), but is not prohibitive for the shorter runs which will be discussed here.

5.3.1 Stability requirements

Values of the time step and viscosity in the model are chosen in order to satisfy the numerical stability criteria (Press *et al.*, 1986), as discussed in Chapter 4. The wave equation criterion (Eq. 5.4) must be satisfied in order for the model to resolve waves.

The time step, Δt, is chosen such that Eq. 5.4 is satisfied, given the grid size Δx (~4 km) and a maximum wave speed, c.

Eq. 5.4 $$\frac{\Delta x}{2\Delta t} > c$$

It is possible for barotropic waves to travel at high speeds (~100 ms^{-1}), so Δt is assigned a value of 20 seconds to remove any possibility of instabilities arising. If only the baroclinic mode was to be resolved, the time step could be much longer, as baroclinic waves are considerably slower than barotropic waves. Hence the increase in computation time required when using this method.

The second criterion, the diffusion condition (Eq. 5.5), must be satisfied in order for the model to resolve diffusion processes across grid cells:

Eq. 5.5 $$\frac{\Delta x^2}{2\Delta t} > D$$

where D is the diffusion coefficient (either viscosity, μ, or thermal diffusivity, κ). If diffusion processes are too fast, the model is unable to resolve the motion and numerical instabilities are likely to occur. Given the values of Δx and Δt, D can take a wide range of values, from 0 to ~10^5 m^{-2}. The values of viscosity and thermal diffusivity chosen will be discussed further in Section 5.4.4.

5.3.2 Equations of motion

The non-linear equations of momentum and heat transfer solved in the model are given below:

Eq. 5.6 $$\left(\frac{\partial \boldsymbol{v}}{\partial t} + \boldsymbol{v} \cdot \nabla \boldsymbol{v}\right) = -\frac{1}{\rho_0}\nabla \boldsymbol{p} - 2\Omega \times \boldsymbol{v} + \tau + \mu \nabla^2 \boldsymbol{v}$$

Eq. 5.7 $$\frac{\partial T}{\partial t} + \boldsymbol{v} \cdot \nabla T = Q + \kappa \nabla^2 T$$

where $\boldsymbol{v}$ is the velocity vector, $\boldsymbol{p}$ is the pressure, Ω is the Coriolis parameter, τ is the wind stress, μ is the coefficient of viscosity, κ is the coefficient of thermal diffusivity and Q represents solar heating. In Eq. 5.6, terms on the left hand side represent local and convective inertia forces. These are balanced by the pressure gradient, Coriolis, wind stress and viscous forces on the right hand side.

5.3.3 Adaptations to fresh water lake

The original model on which this version is based was implemented for the Pacific Ocean, and therefore utilised a linear equation of state such that the maximum density, ρ_{max}, occurs at T = 0°C and decreases linearly with increasing temperature. This model of a freshwater system incorporates a quadratic equation of state, where ρ_{max} is reached at the temperature of maximum density, T_{md}. The density at depth z is given by Eq. 5.8 below:

Eq. 5.8 $$\rho(z) = \rho_{\max}\left(1 - \lambda(T(z) - T_{md}(z))^2\right)$$

where $T(z)$ is the temperature at depth z in degrees centigrade, T_{md} decreases with pressure at a rate of 0.021°C bar^{-1}, λ = 8 x10^{-6} °C^{-2} and the maximum density of water, ρ_{max}, is assumed to be constant with depth at 998 Kg m^{-3}. This approximation to the equation of state has only a few percent error over the temperature range 0 - 8°C (Matthews and Heaney, 1987).

5.3.4 Conversion to *N* layers

A significant development from the original model has been the conversion from two layers to any number of layers, N. As the temperature at any grid point is constant within a given layer, the increase in the number of layers allows for a much more realistic temperature structure. There is no theoretical limit on N, but the N-fold increase in computation time over a single layer is clearly a major consideration.

5.4 Parameterisation of physical processes

Certain physical processes would be too complex and use too much computation time to model explicitly. They can, however, be adequately parameterised in such a way as to produce realistic results and retain the predictive capability of the model. A description of the parameterisations used in this model follows.

5.4.1 Solar heating

During ice cover, when wind stress can be neglected, the model is driven solely by surface heat fluxes. The intensity of radiation at depth decreases exponentially with depth at a rate dependent on the extinction coefficient, ε, of the medium through which it passes. Penetration of radiation through the surface is also dependent on the albedo, α. If the lake is ice-covered, heating will be significantly reduced due to both the increase in albedo and to the high extinction coefficient of the ice/snow layer. To model this complex process some parameterisation is necessary. An adequate scheme is to allow the intensity of solar radiation, I_z, to decrease exponentially with depth z, as given by:

Eq. 5.9 $$I_z = I_0(1-\alpha)\exp(-\varepsilon_s d_s - \varepsilon_i d_i - \varepsilon_w z)$$

where I_0 is the incident solar radiation, α is the surface albedo, $\varepsilon_{s,i,w}$ are the extinction coefficients of snow, ice and water respectively, and $d_{s,i}$ is the thickness of snow and ice (Matthews and Heaney, 1987). It can be seen that as the surface albedo increases or the thickness of ice increases, the amount of solar radiation penetrating to depth z decreases.

The incident solar radiation, I_0, is taken to be solar radiation in the spectral range 400-700 nm, referred to as Photosynthetic Available Radiation (PAR), which is the primary source of heating within the lake. PAR varies with month due to the change in solar inclination, as illustrated in Figure 5.1 (calculated from observations for Lake Baikal (Shimaraev *et al.*, 1993)).

The rate of temperature increase at depth z (term Q in Eq. 5.7) is then given by:

Eq. 5.10 $$\frac{\partial T}{\partial t} = \frac{I_z \varepsilon_w}{\rho C_p}$$

where ρ is the density of water and C_p the specific heat capacity, 4.2 x 10^3 J kg^{-1} $°C^{-1}$.

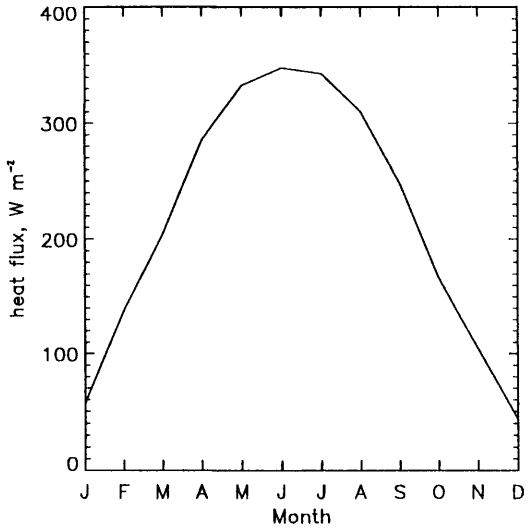

Figure 5.1: Values of I_0 used in the model (direct PAR) (After Shimaraev *et al.*, 1993).

Although the values of extinction coefficients vary considerably over the visible wavelength range (e.g. 0.05 m^{-1} at 500 nm to 0.3 m^{-1} at 600 nm for water in Lake Baikal (Shimaraev *et al.*, 1994)), constant values are assumed here for simplicity. The effect of varying the extinction coefficient values is investigated in section 5.10. Values of ε_i and ε_s are taken from the literature (Matthews and Heaney, 1987), and will be discussed further in Section 5.4.2.

5.4.2 Ice and snow layer

In addition to the layers representing water, two layers of ice and snow are also included. From Eq. 5.9 above it can be seen that both albedo and extinction coefficient play an important role in determining heating in the lake. The distribution of snow and ice on the lake will, therefore, be a major factor in the development of density-driven flow, caused by differential heating under regions of snow-free and snow-covered ice. The albedo, extinction coefficient and spatial distribution of ice and snow are derived from satellite data of the lake for the period March to June 1997, as described in Chapter 3. As noted above, extinction coefficient values vary over the wavelength range 400-700 nm, and so the effect of varying these values is investigated in Section 5.10.

The ice layer is given an initial thickness of 0.8 m, and decreases with time at a constant rate, such that the thickness reduces by half over a period of 60 days. The layer representing snow has a uniform thickness (e.g. 0.025 m), the value of which can be varied to investigate the effect of different snow conditions (see section 5.9). A new 'ice mask' is read in to the model at specific days, updating each grid cell surface type accordingly. This allows the 'disintegration' of relatively thick ice (~0.4 m) at specific locations (determined from the satellite data), a process which occurs in the real lake.

5.4.3 Wind stress

During the period of ice cover, wind stresses on the surface are effectively zero. However, once the ice melts, wind stress can be applied to the surface by specifying the speed and direction of the wind. This translates to a force, τ, (see Eq. 5.6) according to Eq. 5.11 below:

Eq. 5.11 $$\tau = \rho_{air} \times c_D \times |u| \times u \ \mathrm{Nm^{-2}}$$

where u is the wind speed in $\mathrm{ms^{-1}}$, ρ_{air} = 1.2 Kg $\mathrm{m^{-3}}$, c_D (the drag coefficient) = 1.5 x 10^{-3}. For example, a wind speed of 10 $\mathrm{ms^{-1}}$ gives rise to a wind stress on the surface of 0.18 $\mathrm{Nm^{-2}}$.

5.4.4 Convective mixing

As surface water cooler than 4°C is warmed its density increases. If this causes it to become denser than the water below, it will sink until it reaches a depth where the surrounding water has the same density. The surface water is in turn replaced by less dense water from below. In the model this is parameterised by 'swapping' adjacent layer temperatures when the upper layer becomes denser than the lower layer. The new temperature of the two layers is adjusted according to the relative thicknesses of the layers involved, in order to retain the correct heat content, as given by the algorithm in Eq. 5.12 below. The process begins at the top layer, continues to the lowest, and the entire sequence repeated until a stable profile is achieved.

$$T_n = T_{n+1}$$

Eq. 5.12 $$T_{n+1} = (1-H_n / H_{n+1}) \times T_{n+1} + (H_n / H_{n+1}) \times T_n$$

where n represents the layer number, T is the temperature and H is the layer thickness. (Note that this formulation of the algorithm applies to the case when H_{n+1} is greater than or equal to H_n).

For example, consider a two-layer system in which the upper layer is 1 m thick, the lower layer is 2 m thick and the temperature of both is a uniform 3°C. If the upper layer (layer 1) is warmed to 4°C it becomes denser than layer 2 and convective mixing will occur until the system becomes stable. From Eq. 5.12 the temperature of layer 1 becomes 3°C and layer 2 becomes 3.5°C. i.e. water in layer 1 is replaced by cooler upwelling water from layer 2, but water in layer 2 is only partially replaced by the warmer water from layer 1 due to its greater thickness. The new temperature profile is now stable again.

5.4.5 Turbulent mixing

Mixing due to turbulence takes place in both horizontal and vertical directions. The transfer of heat and momentum is modelled by the eddy thermal diffusivity term, $\kappa\nabla^2 T$, and viscosity term, $\mu\nabla^2 u$ in Eq. 5.6 and Eq. 5.7 above. The coefficients of eddy thermal diffusivity (κ) and viscosity (μ) have components in the horizontal and vertical. In order to maintain numerical stability, the horizontal components κ_h and μ_h must have values between 0 and 10^5 $\mathrm{m^2 s^{-1}}$, and 10^4 and 10^5 $\mathrm{m^2 s^{-1}}$ respectively. They are chosen to have the constant values:

$\kappa_h = 1\ m^2s^{-1}$; $\mu_h = 10^4\ m^2s^{-1}$.

A lower value for κ_h than might normally be used (e.g. $5 \times 10^3\ m^2s^{-1}$, (Stockdale, 1992)) has been chosen here to parameterise the reduction in horizontal turbulent mixing when the lake is ice covered. A higher value is used when the lake becomes ice-free. The value of μ_h is chosen to be the minimum possible while still satisfying the numerical stability criteria.

Turbulent mixing in the vertical direction occurs to a lesser extent than in the horizontal and is dependent on the stability of the water column. Turbulence and, therefore, mixing will be suppressed when the water column is well stratified, with density increasing rapidly with depth. The scheme to parameterise vertical mixing implemented in this model has been derived from existing methods (described below), combining the vertical density gradient with a fixed profile to determine the vertical coefficients of eddy thermal diffusivity, κ_v, and viscosity, μ_v.

In *fixed profile mixing* κ_v, and μ_v, are given a value which depends on depth, according to a fixed profile, κ_{prof}, such as that in Figure 5.2 (Stockdale, 1992). Mixing is generally strongest near the surface, decreasing with depth as the temperature approaches T_{md} where convection is minimal.

Eq. 5.13 $\mu_v = \mu_0 \kappa_{prof}$, $\kappa_v = \kappa_0 \kappa_{prof}$

Measurements in the lake (Shimaraev *et al.*, 1994) suggest that a suitable maximum value of κ_0 is $10^{-4}\ m^2\ s^{-1}$. Pacanowski and Philander (1981) propose that μ_0 should have a value of around $10^{-2}\ m^2\ s^{-1}$.

Since κ_0 is actually variable, and dependent on the stability of the water column, the *fixed profile* method is not ideal for use in Lake Baikal, where the vertical density gradient varies a great deal with time.

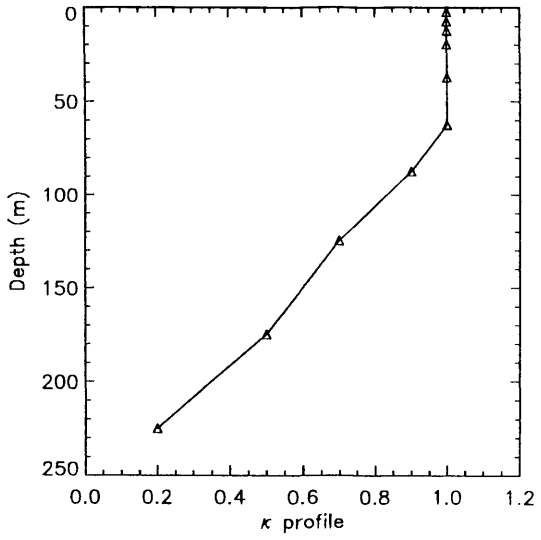

Figure 5.2: Depth profile used in the *fixed profile* method

Another method of parameterising mixing was originally described by Pacanowski and Philander (1981) (hereafter referred to as *PP mixing*). Vertical components of κ and μ are

determined by considering the Richardson number, R_i. This number is the ratio between buoyancy and horizontal current shear, and therefore parameterises vertical mixing in terms of turbulence at layer interfaces. A low value of R_i implies a low buoyancy compared to horizontal shear, and hence maximal vertical mixing. The Richardson number is used to modify background values of thermal diffusivity and viscosity to obtain the vertical components, κ_v and μ_v, as given by Eq. 5.14 and Eq. 5.15 below.

Eq. 5.14 $$\kappa_v = \frac{\mu_0}{(1+aR_i)^3} + \kappa_b$$

Eq. 5.15 $$\mu_v = \frac{\mu_0}{(1+aR_i)^2} + \mu_b$$

where κ_b is the background diffusivity, μ_b is the background viscosity and μ_0 is the maximum viscosity.

Pacanowski and Philander (1981) recommend the following values for the parameters in Eq. 5.14 and Eq 5.15 above:

$$a = 5, \quad \mu_0 = 10^{-2}\ \mathrm{m^2\ s^{-1}}, \quad \kappa_b = 10^{-5}\ \mathrm{m^2\ s^{-1}}, \quad \mu_b = 10^{-4}\ \mathrm{m^2\ s^{-1}}$$

R_i is given by:

Eq. 5.16 $$R_i = -\frac{bg\,\partial\rho/\partial z}{\left(\frac{\partial u}{\partial z}\right)^2 + \left(\frac{\partial v}{\partial z}\right)^2 + c}$$

where $b = 8 \times 10^{-6}$, $c = 10^{-10}$, g is the acceleration due to gravity, ρ is the density, u and v are the horizontal components of velocity at depth z. The term c is required to prevent numerical problems from occurring in the model when u and v are zero.

As discussed above, this scheme is a parameterisation of turbulent mixing caused by current shear. Therefore, in cases where the current shear approaches zero (zero vertical velocity gradient), R_i tends to infinity[1] (regardless of the density gradient) and the mixing coefficients reduce to the background values. This often occurs under ice cover when there are no wind-induced currents, and, therefore, *PP mixing* alone is not a suitable scheme for parameterising vertical mixing.

The scheme incorporated into this model combines the most relevant aspects of those discussed above, and will be referred to as *PP variant mixing*. It is an improvement on the *fixed profile* scheme, as it introduces a dependency on the density gradient as used in *PP mixing*, but does not require current shear to increase the mixing coefficients. Physically, this scheme

[1] This is actually prevented in the model by the addition of the term c in Eq. 5.16.

parameterises the effect of convective mixing when the density gradient is small but positive (i.e. a stable temperature profile), which can occur due to the small amounts of vertical momentum required to mix water when the water column approaches neutral stability. This process would not be resolved by the simple parameterisation of convective mixing described initially, and removes the problems caused by low current shear. The terms κ_v and μ_v are now obtained as follows:

Eq. 5.17 $$\kappa_v = \frac{\mu_0 \kappa_{prof}}{\left(1+\beta\frac{\partial\rho}{\partial z}\right)} + \kappa_b$$

Eq. 5.18 $$\mu_v = \frac{\mu_0 \kappa_{prof}}{\left(1+\beta\frac{\partial\rho}{\partial z}\right)} + \mu_b$$

where κ_{prof} is given by a fixed profile as described above, $\beta = 10^{11}$, $\kappa_b = 10^{-5}$ m^2 s^{-1}, $\mu_b = 10^{-4}$ m^2 s^{-1} and $\mu_0 = 10^{-2}$ m^2 s^{-1}. It can be seen that the form of these terms is very similar to those used by the *PP mixing* scheme; the term (β x density gradient) is simply the Richardson number (Eq. 5.16) when current shear is zero.

The vertical coefficients reach a maximum when the water column is neutrally stable (zero vertical density gradient), during which time κ_v has a value of around 10^{-2} m^2 s^{-1} (Shimaraev *et al.*, 1994). When the density gradient is large (e.g. in the thermocline), mixing is suppressed and the coefficients tend to the background values.

5.5 Vertical structure

Before the model can be run, certain initial conditions need to be set. These include the number of layers, their thickness and temperature. The region of interest of this study is the upper few hundred metres, where diatom re-suspension by convective mixing occurs. Deep water exchange processes between the upper and lower regions of the lake are localised and infrequent, and, therefore, can be neglected in this model of the upper layers. For this reason, only the upper 250 m are modelled, thus removing the need for unnecessary computation at greater depths.

The implementation of Eq. 5.9 in the model is such that changes to the vertical resolution (i.e. the initial layer thicknesses) do not affect the heat content of the system. An adequate resolution of the temperature profile of the lake is required in order to resolve the physical processes being studied. It was decided that ten layers, initialised with thicknesses varying between 5 m at the surface to 50 m at the bottom, satisfactorily reproduces the temperature structure, while retaining a manageable computation time. See Figure 5.3 for a schematic showing the initial layer thicknesses.

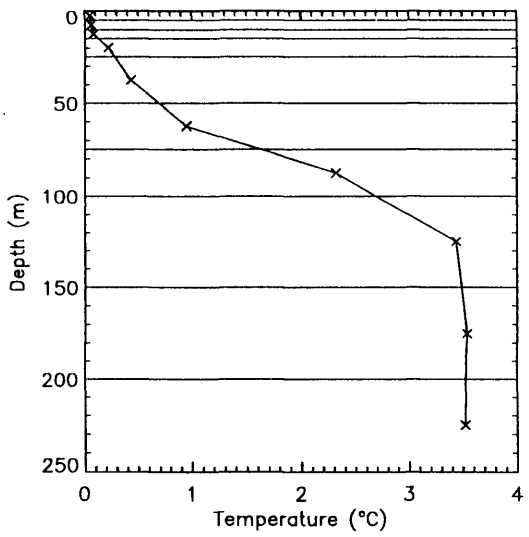

Figure 5.3: **Schematic showing the initial layer thicknesses and temperature profile, given by *in situ* measurements at a point in the South Basin, mid-way between Listvyanka and Tankhoy, made on 13th March 1997 (Jewson, personal correspondence).**

In situ temperature profile data is limited to one location on the lake due to the difficulties in obtaining data during the period of ice cover. The time period to be investigated is primarily Spring, from the time of maximum ice thicknesses, up to complete ice-melt. Each layer is therefore initialised to a uniform temperature, as measured in the lake during March 1997, when the ice was at its thickest. Figure 5.3 also shows the initial temperature profile.

5.6 Model runs investigating under-ice flow

The primary aim of running the model is to investigate current flow and temperature profile development during the period of ice cover on Lake Baikal. Additional runs can be used to determine the effect of varying some of the model parameters, such as increasing the albedo values and decreasing the thickness of the snow layer. These results can then be compared with the original 'control' run, R1. The parameters which are to be changed are discussed in more detail below. Table 5.1 gives a summary of the setup in each model run.

Table 5.1: Summary of model runs

Model run	Details	Main purpose
R0	No mixing, 10 layers, 100 days, $albedo_1$, $epsilon_1$, t_{snow} = 0.025 m	Effect of using no mixing
R1	PP Variant mixing, 10 layers, 100 days, $albedo_1$, $epsilon_1$, t_{snow} = 0.025 m	Control run
R2	PP Variant mixing, 10 layers, 100 days, $albedo_2$, $epsilon_1$, t_{snow} = 0.025 m	Effect of increasing the albedo by 20%
R3	PP Variant mixing, 10 layers, 100 days, $albedo_1$, $epsilon_1$, t_{snow} = 0.01 m	Effect of reducing the snow thickness
R4	PP Variant mixing, 10 layers, 100 days, $albedo_1$, $epsilon_1$, t_{snow} = 0.04 m	Effect of increasing the snow thickness
R5	PP Variant mixing, 10 layers, 100 days, $albedo_1$, $epsilon_2$, t_{snow} = 0.025 m	Effect of using different epsilon values
R6	Fixed profile mixing, 10 layers, 100 days, $albedo_1$, $epsilon_1$, t_{snow} = 0.025 m	Effect of using fixed profile mixing

5.6.1 Mixing schemes

The effect of using different mixing schemes is investigated in model runs R0, R1 and R6. Comparisons are made between runs using the simple scheme which parameterises convective mixing by 'swapping' layer temperatures (R0), the *PP Variant* mixing scheme (R1), and one which uses a *fixed profile* (R6).

5.6.2 Albedo and extinction coefficients

There is some discrepancy in the literature over the values of albedo and extinction coefficient measured for particular types of ice and snow. This is to be expected, as it is impossible to define precisely each surface type - rather, there is a gradual transition from one type to another. For example, 'new white ice' *gradually* becomes 'old white ice', with many degrees in between.

An increase in surface albedo will cause a greater percentage of the incident solar radiation to be reflected, thus reducing the amount of energy available to heat the water. By increasing the albedo of each surface type in one model run, compared to the control run, this effect may be observed and the importance of determining precise albedo values gauged. Similarly, as the extinction coefficients, ε, are increased, the opacity of the surface cover (e.g. the ice layer) increases, also leading to a reduction in the amount of solar radiation reaching the water (as shown

by Eq. 5.9). Model runs using an increase in albedo (R2) and ε (R5) are compared with the control run (R1). The sets of values used are given in Table 5.2 below.

Table 5.2: Albedos and extinction coefficients for each classification type.

Classification type	Assigned albedo		Extinction coefficient (m^{-1})	
	$albedo_1$	$albedo_2$	$epsilon_1$	$epsilon_2$
Water	0.05	0.06	0.2	0.2
Clear (fresh) ice	0.25	0.30	0.2	0.3
Slush ice	0.20	0.24	3.5	3.5
Frazil ice	0.25	0.30	3.5	3.5
Fresh white ice	0.45	0.54	2.0	3.5
Old white ice	0.40	0.58	3.0	3.5
White ice melt pond	0.38	0.46	3.0	3.5
Semi-transparent ice	0.30	0.36	0.8	1.0
Ice/snow mix	0.50	0.60	2.0	3.5
Snow melt pond	0.58	0.70	40.0	40.0
Snow	0.60	0.72	40.0	40.0

5.6.3 Snow thickness

An increase in the thickness of the layer of snow will clearly reduce the amount of solar radiation reaching the water below (as shown by Eq. 5.9). The snow thickness is likely to vary considerably over the area of the lake, and cannot be measured *in situ* (except in a small number of locations) or by using thermal and visible wavelength satellite data. It is therefore important to determine what effect increasing or decreasing the initial snow thickness will have on the model results. Three model runs, using a snow layer thickness (t_{snow}) of 0.01 m, 0.025 m and 0.04 m, are used to investigate the impact on the development of the temperature structure in the lake.

5.7 Results from R1

Model run R1 was run for 100 days, from 13th March to 21st June, using the *PP Variant* scheme to parameterise vertical mixing. Results from the model are described below.

5.7.1 Temperature profile development

Figure 5.5a is a temperature-depth plot of *in situ* measurements made between 13th March and 21st June 1997, at a boundary between snow-free and snow-covered white ice in the South Basin (Jewson and Granin, personal correspondence). Figure 5.5b shows model results at point B (See Figure 5.4 for location), corresponding to the location of the *in situ* measurements. The profiles in Figure 5.5c are located at point C (See Figure 5.4 for location), under snow-free semi-transparent ice.

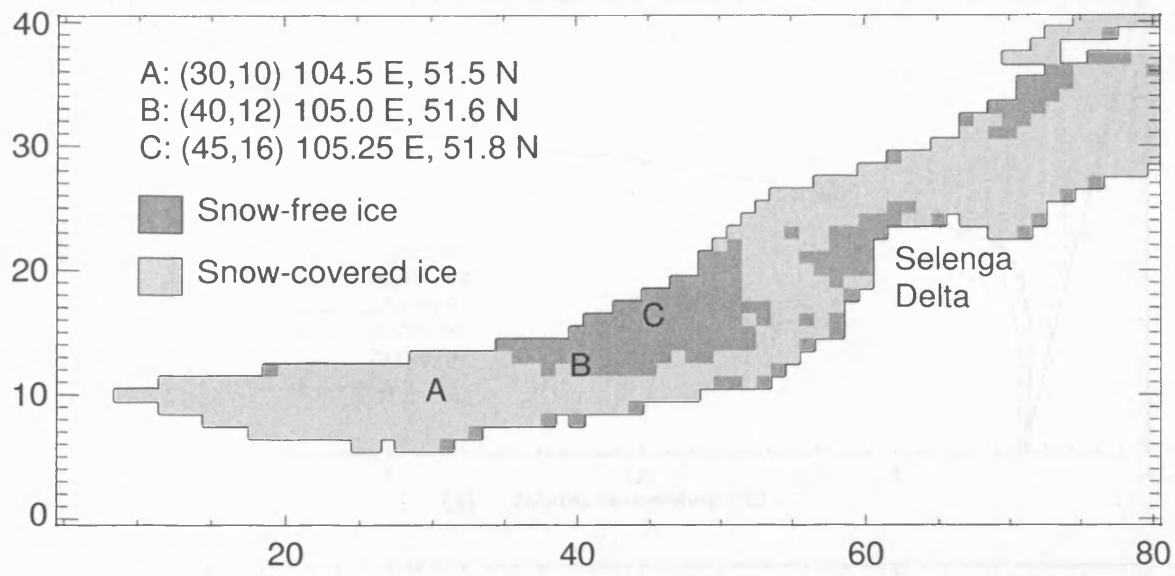

Figure 5.4: Locations of model generated temperature-depth profiles discussed in this chapter. Point A, at model grid point (30,10), is located at a region initially (on 13th March) under snow-covered ice. Point B, at model grid point (40,12), is at the boundary between snow-covered and snow-free ice. Point C, at model grid point (45,16), is initially under snow-free, semi-transparent ice.

After 100 days of model integration time (equivalent to 21st June) the model in Figure 5.5b has reached a temperature of 3.7°C and is well mixed down to 200 m, having an almost constant temperature with depth. This compares well with the *in situ* profile for this date, which is also well mixed, with a temperature of 3.7°C. The model has also been successful in reproducing the deepening of the mixed layer observed in the *in situ* data, seen as a shift to the left below 120 m (i.e. cooling) of the temperature profile, most noticeable for 23rd May and 6th June. The model profile for 2nd April does not appear to agree closely with the *in situ* data for this date, particularly in the depth region 50 to 200 m. However, this is in fact due to a change in location for the *in situ* measurement on this date. A different site, closer to the shore, was required due to the partial break up of ice preventing measurements being made from the usual site. This profile is included in the plots to give an approximate idea of the temperature structure at that time, but caution should be applied when validating the model results with this *in situ* data.

For each date shown there is good agreement between the model results in Figure 5.5b and the *in situ* profiles shown in Figure 5.5a. By contrast, Figure 5.5c shows considerably more warming (about 0.5°C) than in Figure 5.5b. This is due to a lower extinction coefficient (the ice being more transparent), allowing more solar radiation to be transmitted through the ice which results in the water being heated more quickly. The strong similarity between the two plots Figure 5.5a and b indicates that the parameterisations used in the model are an adequate representation of the physical processes involved. Further studies using this model can therefore be undertaken with a good degree of confidence.

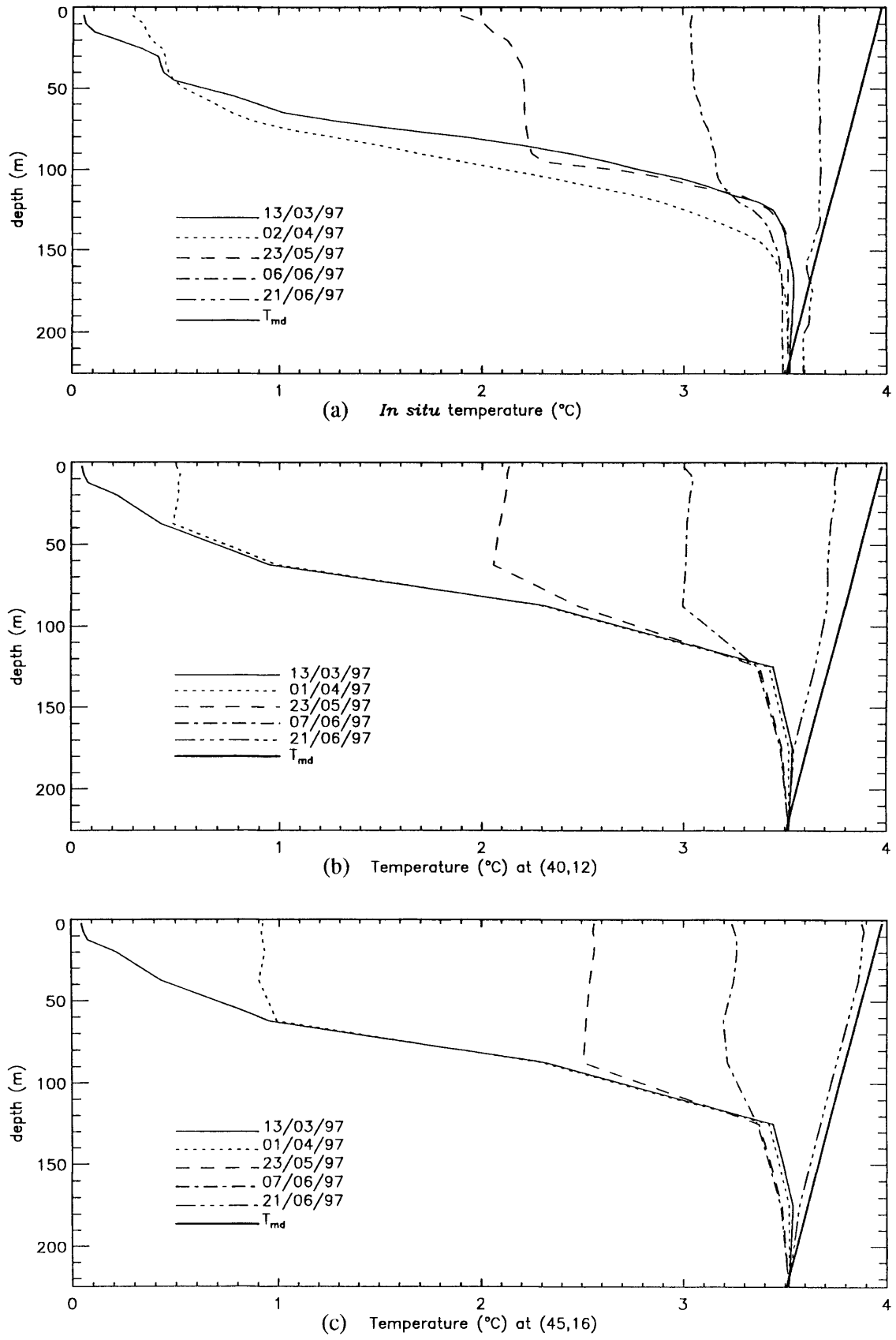

Figure 5.5: Plots of (a) *in situ* and (b) model generated temperature profiles at the mid-point between Listvyanka and Tankhoy in the South Basin (point B). Also (c) model generated temperature profile at point C. The profiles shown are for the dates 13th March, 2nd April, 23rd May, 7th June and 21st June 1997 (see key), for model run R1.

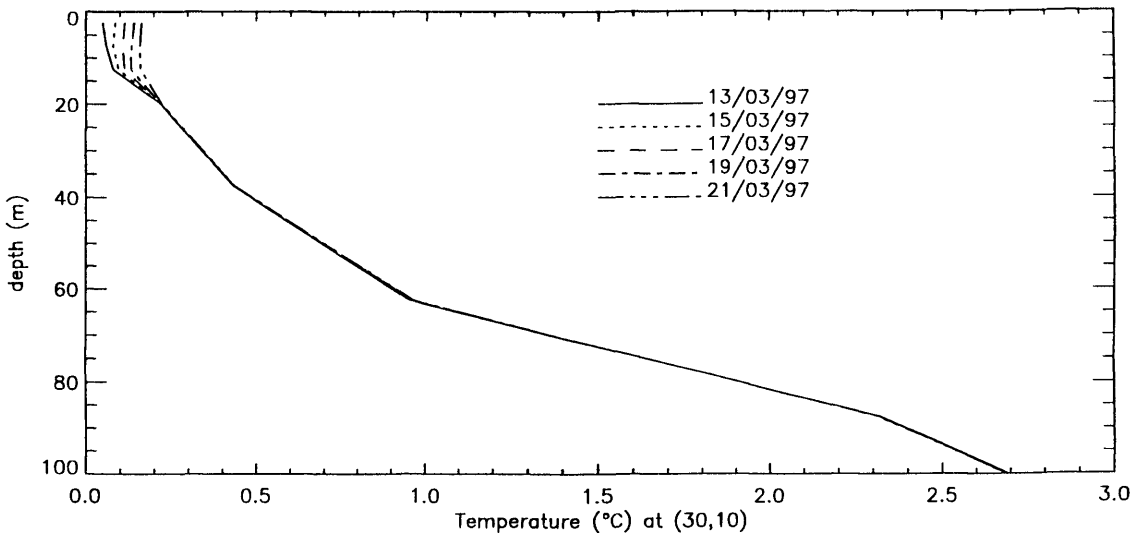

(a)

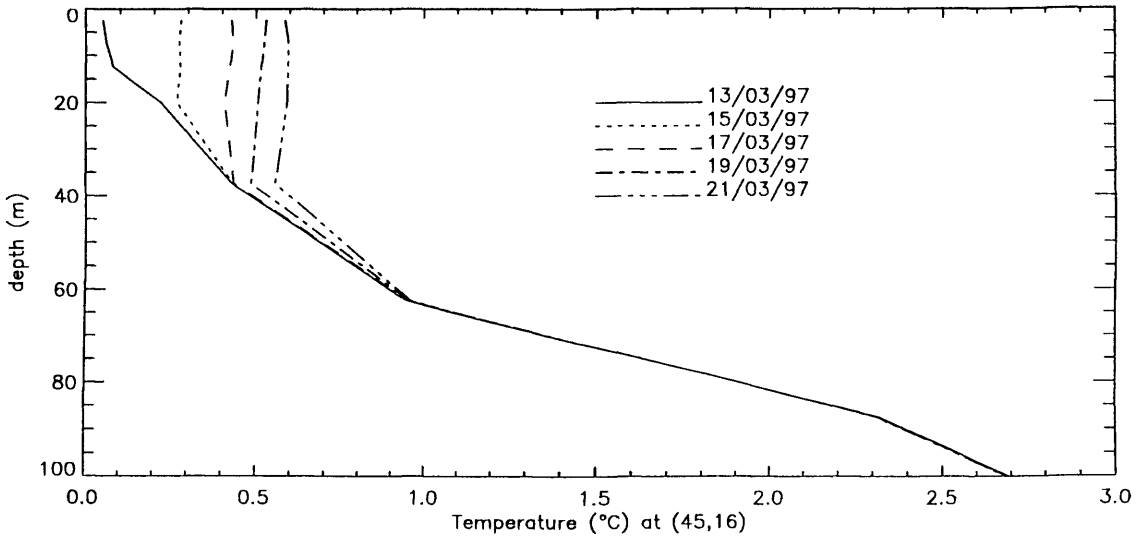

(b)

Figure 5.6: Plots of model-generated temperature profiles between 13/03/97 and 21/03/97 (see key) using an initial profile (solid line) given by *in situ* measurements on Lake Baikal for 13/03/97 at the mid-point between Listvyanka and Tankhoy in the South Basin (point B). Results shown are for model grid points: (a) point A - snow covered white ice and (b) point C - snow-free semi-transparent ice.

Figure 5.6 shows model-generated temperature profiles at points with different snow and ice conditions. In each plot, the temperature at a grid point is shown at the initial time (using *in situ* measurements for 13th March 1997; solid line) and at four subsequent dates at two-day intervals. Figure 5.6a is located at point A (see Figure 5.4) in the South Basin, initially under 0.8 m of white ice and 0.025 m of snow. Figure 5.6b is located at point C initially under 0.8 m of semi-transparent ice, with no snow cover. The water column in Figure 5.6b shows the most warming, the temperature in the top layer being 0.45°C greater than in Figure 5.6a. Clearly the presence of snow, and the opacity of the ice, has had a strong impact on heating. Under snow, the mixed layer has remained at a depth of about 10 m. This increases to 40 m under semi-transparent ice (indicated by the isotropic region of the profiles in Figure 5.6).

5.7.2 Surface temperature

The temperature field for the top layer of R1 (i.e. at a depth of 2.5 m) is shown in Figure 5.7. In Figure 5.7a, the plot for 1st April, the highest temperatures occur beneath snow-free semi-transparent and white ice, in the region of the north-west coast of the South Basin and around Olkhon Island in the Central Basin. Initially, there is little mixing of heat due to a low value of the coefficient of thermal diffusivity, κ_H, which parameterises reduced turbulent mixing under ice-cover. By 23rd May (Figure 5.7b), the ice has begun to melt (again, along the north-west coast, close to the Selenga Delta), resulting in a sharp increase in temperature in that region. The pattern of temperature is now also more diffuse, due to an increase in κ_H in regions where the ice has melted. By June (Figure 5.7c and d), the whole lake is ice-free and the temperature in the South of the lake has increased to nearly 4°C. The North Basin is coolest at around 3°C, as the ice remains here longer than in the South.

5.7.3 Under-ice currents

Figure 5.8 is a time series of plots focusing on the South Basin, showing the top layer model fields representing temperature and velocity, where the arrows indicate the direction and relative speeds of the current flow. It can be seen, particularly in Figure 5.8b, that the fastest current speeds (around 6×10^{-3} ms^{-1}) occur where the temperature gradient is strongest (corresponding to the boundary between snow and snow-free ice). Water flows towards regions of higher density (temperature), which results in the formation of an anti-clockwise circulation cell by 21st June (centred around grid point (57,20) in Figure 5.8c).

The velocity field for the top layer over the whole lake is shown in Figure 5.9, for 1st April and 21st June. Initially (Figure 5.9a), there is very little motion except in the South Basin (as in Figure 5.8b). However, by 21st June (Figure 5.9b) circulation cells have been set up to the west of the Selenga Delta and, to some extent, Ushkany Island. The strongest currents flow northwards along the south-east coast, and return along the north-west coast and central regions of the North Basin.

The profile plot in Figure 5.10 shows how the velocity in the y-direction (South to North) varies with depth and time for point B. The vertical velocity gradient is zero below about 100 m, with the velocity increasing to a maximum at the surface. Currents are strongest, and most variable with depth, for 1st April and 23rd May. By the 7th and 21st June the velocities are almost constant with depth at around 10^{-3} ms^{-1}. The negative velocities below 100 m indicate the presence of a vertical circulation cell; water flows towards a region of higher density (temperature) where it sinks to about 50 m, generating return flow in the opposite direction at that depth and below. This can be seen more clearly in Figure 5.11, a cross-section of temperature and velocity in the y-direction at x=40.

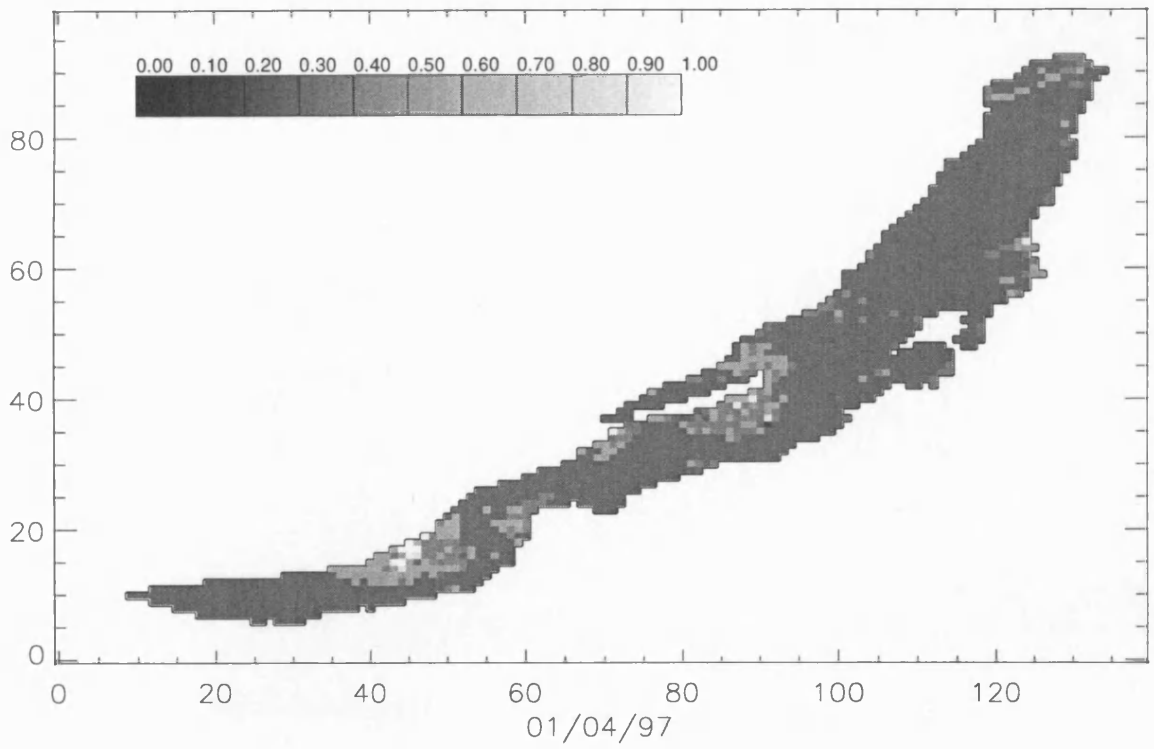

(a)

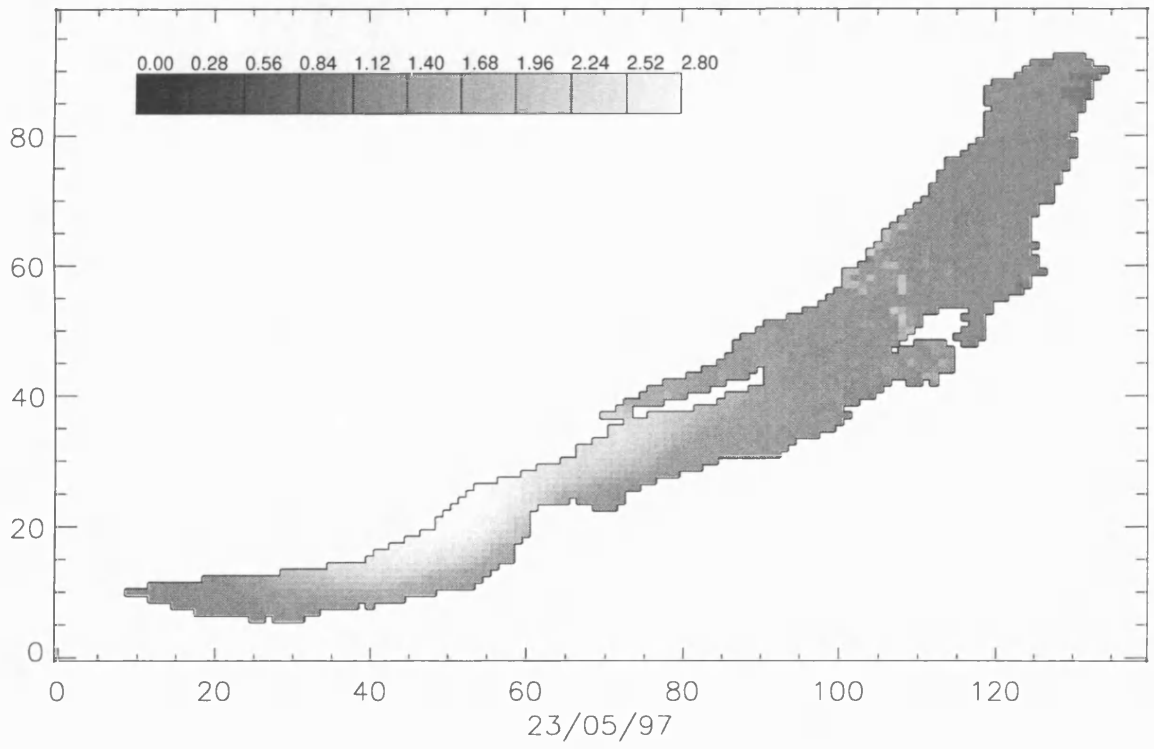

(b)

Figure 5.7: (Page 1 of 2) Temperature field for top layer (i.e. at a depth of 2.5 m), model run R1. (a) 01/04/97 and (b) 23/05/97. The temperature increases most rapidly in the region of the north-west coast of the South Basin and around Olkhon Island in the Central Basin.

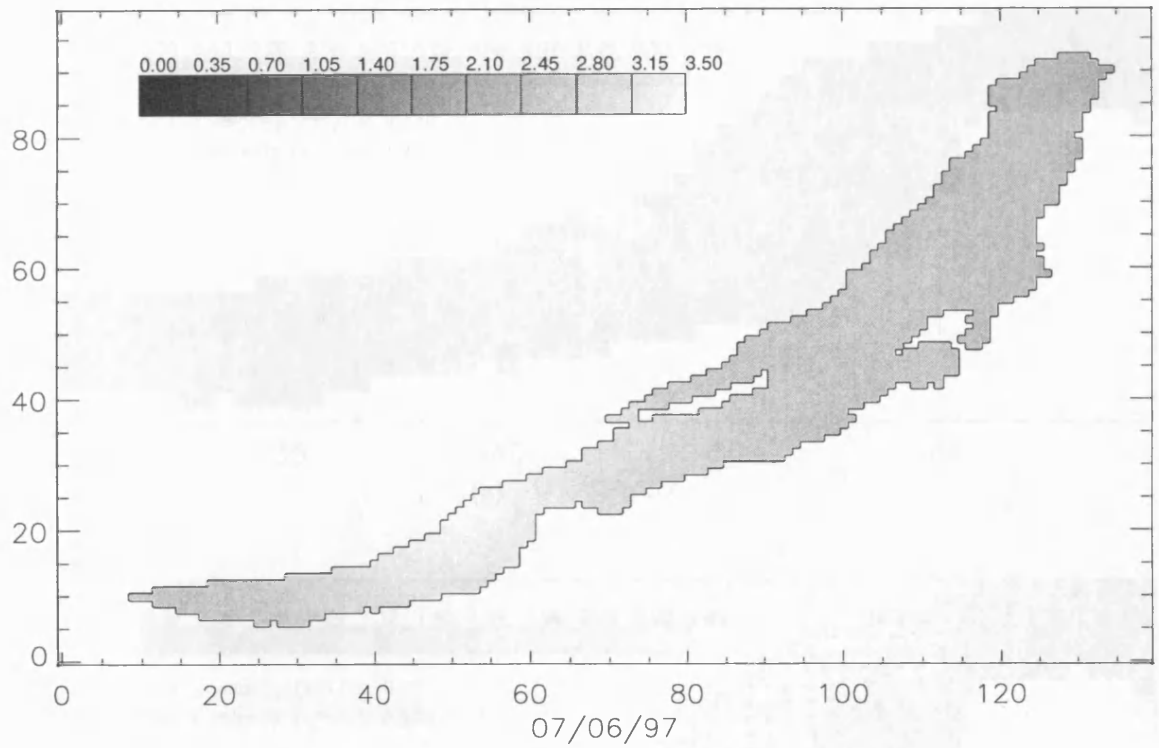

(c)

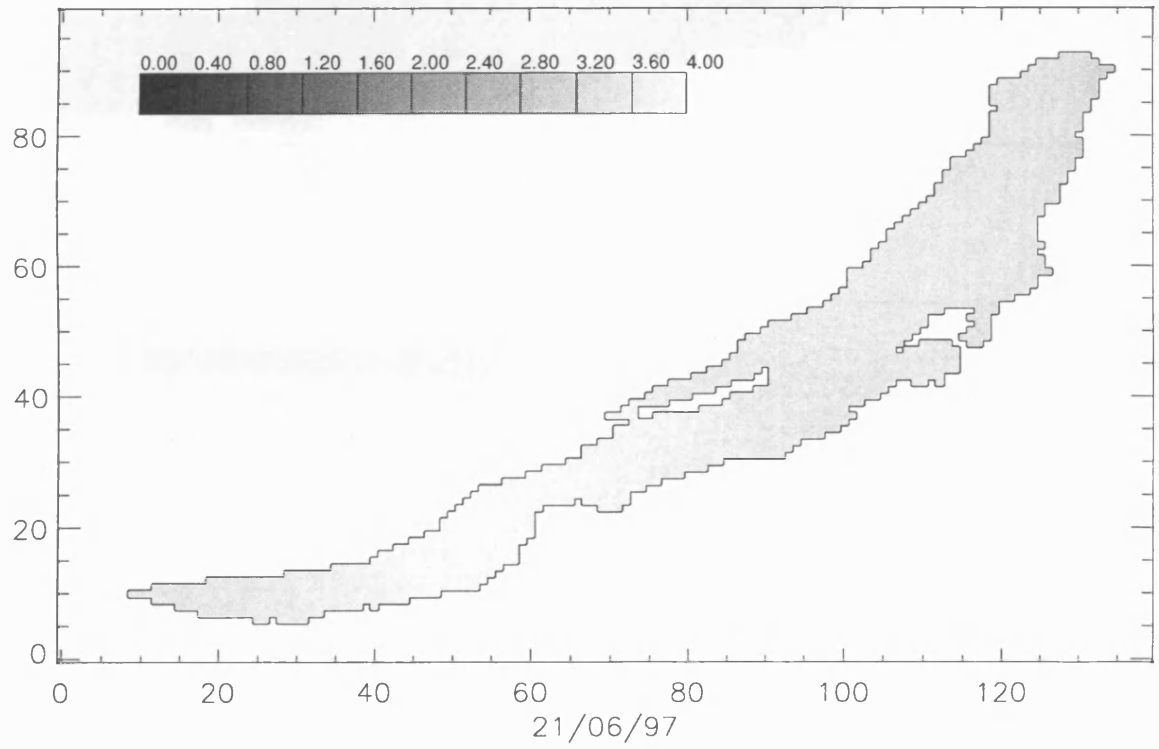

(d)

Figure 5.7: (Page 2 of 2) Temperature field for top layer (i.e. at a depth of 2.5 m), model run R1. (c) 07/06/97 and (d) 21/06/97. The temperature over the whole lake has become more uniform, but the warmest region is still in the South Basin, near the Selenga Delta.

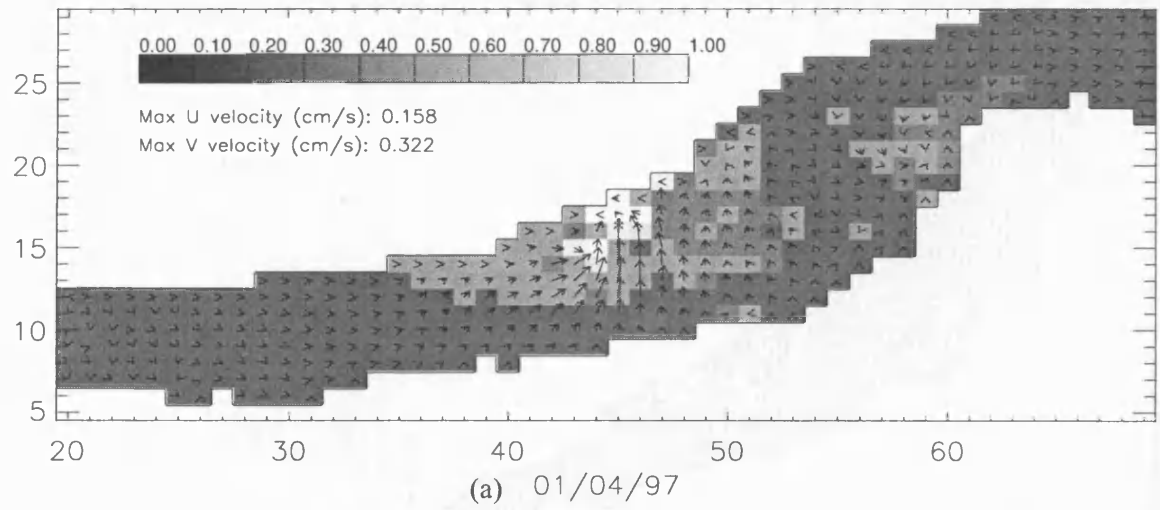

(a) 01/04/97

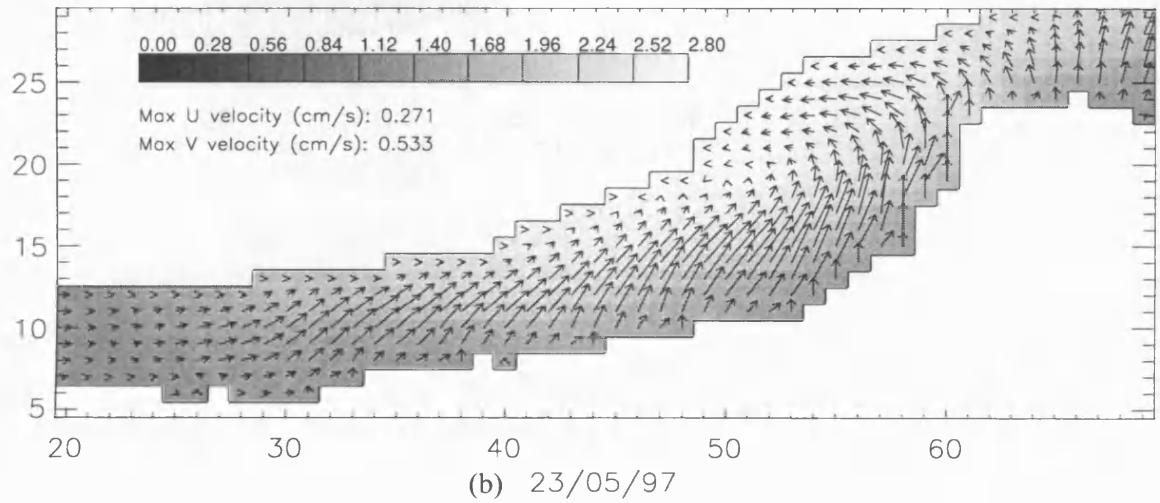

(b) 23/05/97

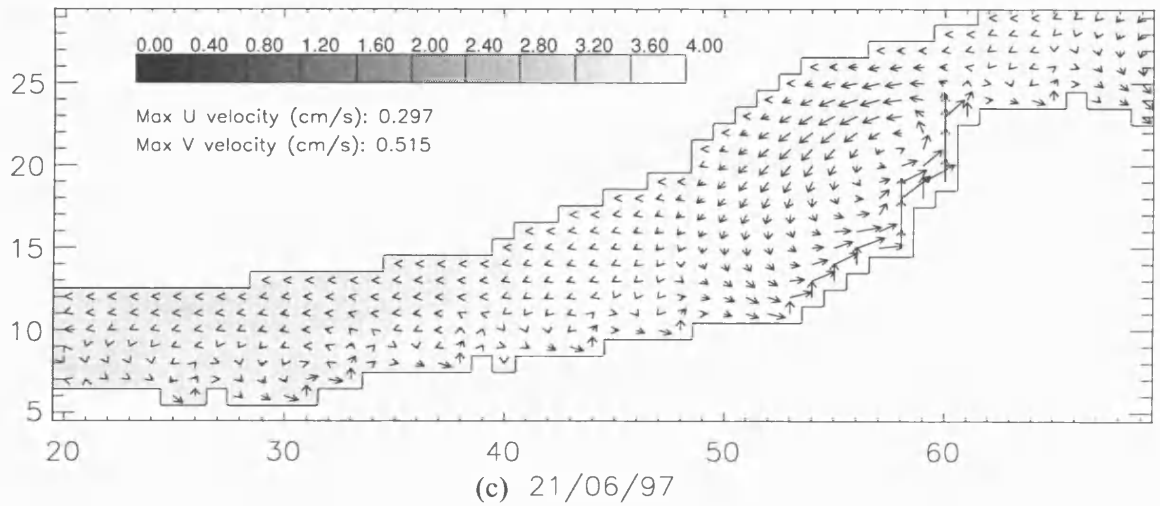

(c) 21/06/97

Figure 5.8: **Top layer velocity field (arrows) overlaid on temperature field for the South Basin region, model run R1. (a) 01/04/07, (b) 23/05/97 and (c) 21/06/97. Arrows indicate the direction and relative strengths of the currents. The maximum current speed is around 10^{-3} ms^{-1}. Currents flow towards regions of higher temperature (higher density). The co-ordinate system refers to the model grid.**

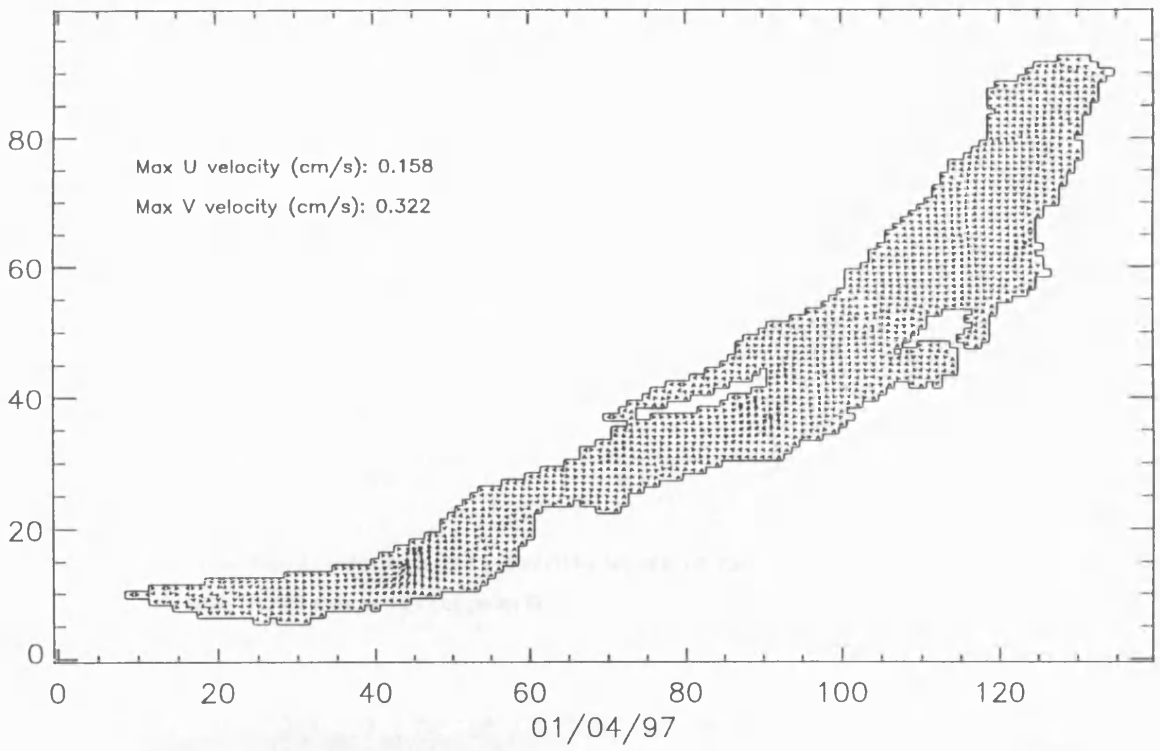

(a)

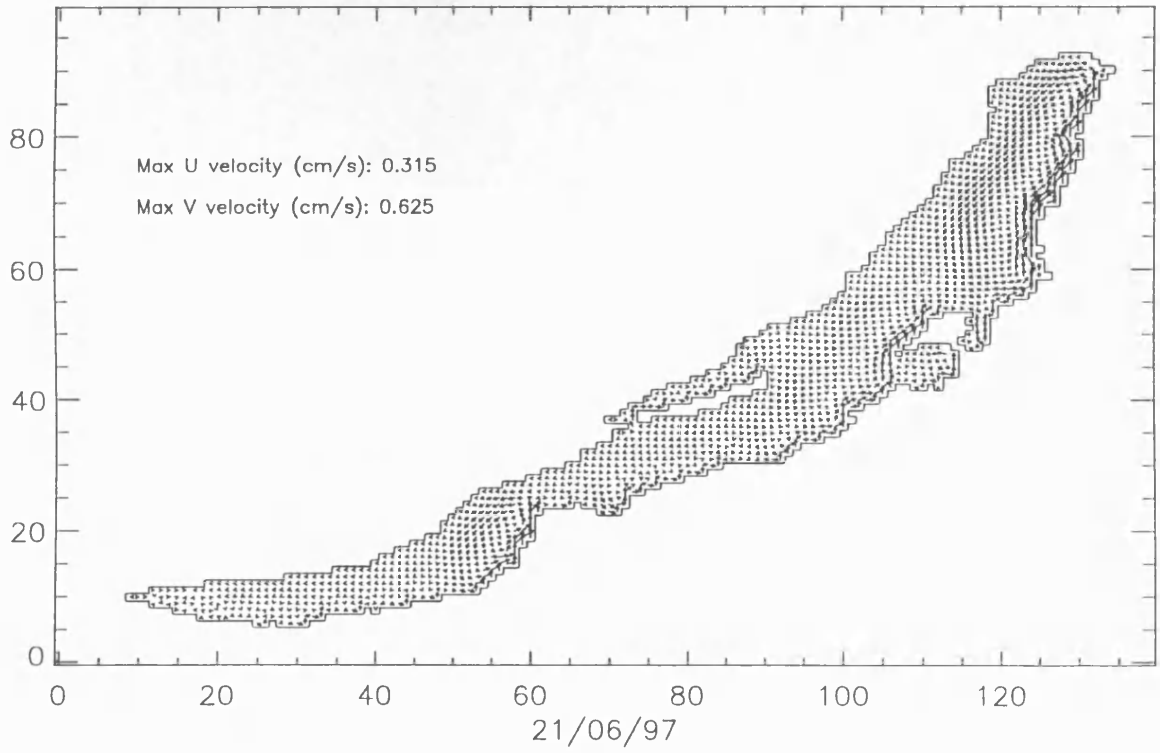

(b)

Figure 5.9: Velocity field for the top layer of model run R1 at (a) 01/04/97 and (b) 21/06/97. Arrows show the direction and relative strength of the currents.

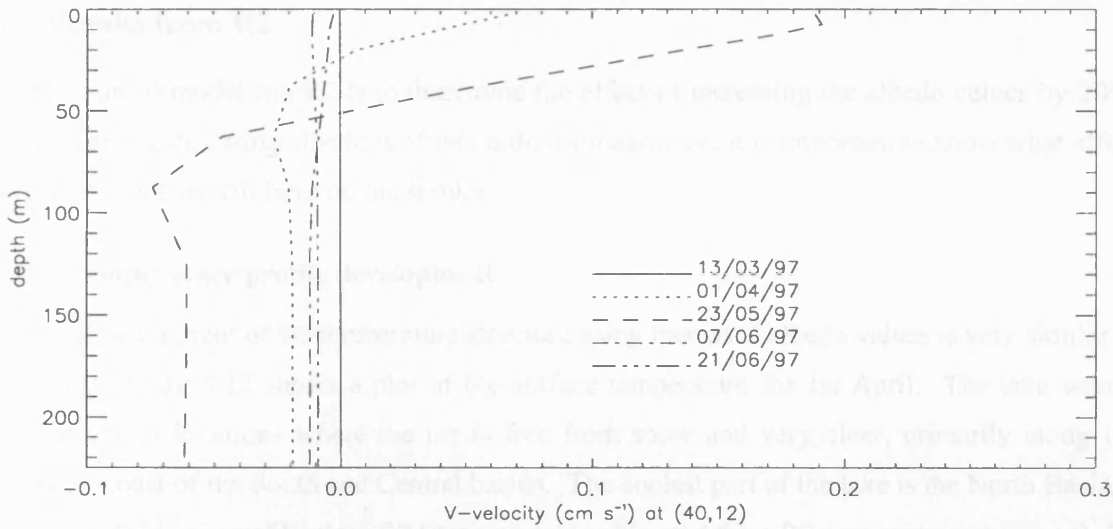

Figure 5.10: Depth profiles of velocity in the v-direction for R1, on the dates 13th March, 1st April, 23rd May, 7th June and 21st June 1997 at point B.

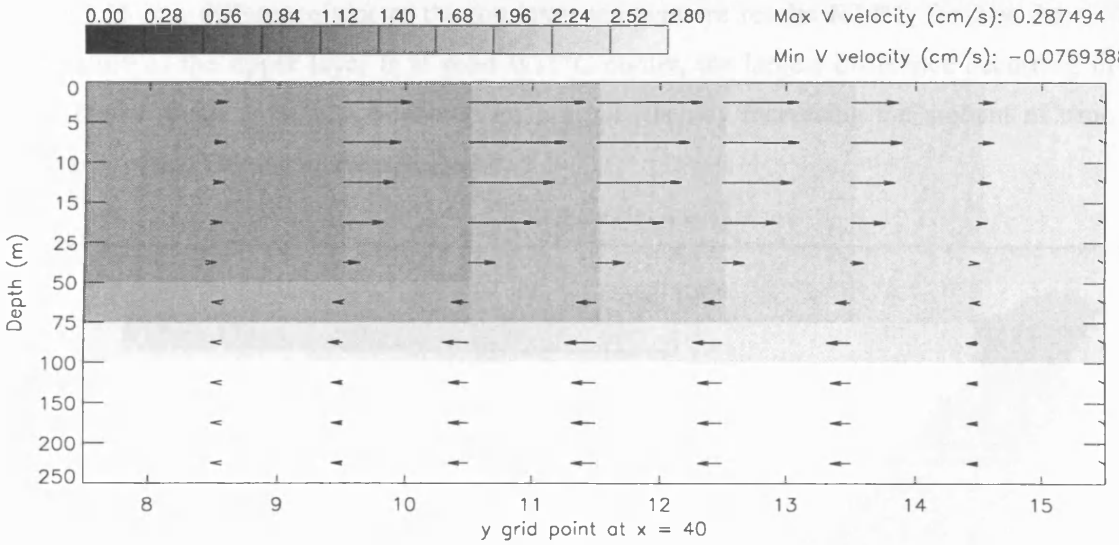

Figure 5.11: Cross-section of temperature and velocity on 23rd May, in the y-direction at x=40, showing flow from South to North (towards the higher density region) in the upper 50 m, and return flow below.

5.8 Results from R2

The aim of model run R2 is to determine the effect of increasing the albedo values by 20%. As the error in calculating albedo is of this order of magnitude, it is important to know what effect changes of this size will have on the results.

5.8.1 Temperature profile development

The development of the temperature structure using increased albedo values is very similar to that in R1. Figure 5.12 shows a plot of the surface temperature for 1st April. The lake warms most quickly at locations where the ice is free from snow and very clear, primarily along the north-west coast of the South and Central basins. The coolest part of the lake is the North Basin.

Figure 5.14 is a profile plot of R1 temperature subtracted from R2 temperature at point B, for dates between 13th March and 21st June. The peak in the maximum temperature difference (about 0.05°C) initially occurs in the upper 50 m, but has spread downwards by 21st June to 200 m, while the surface has returned to almost zero difference compared to the temperature in R1. Figure 5.15 is a difference plot of the top layer temperature results R2-R1, for 21st June. The temperature of the upper layer is at most 0.15°C cooler, the largest difference occurring in the North Basin which remains ice-covered for longest (thereby increasing the amount of time the heating is reduced by the increased albedo).

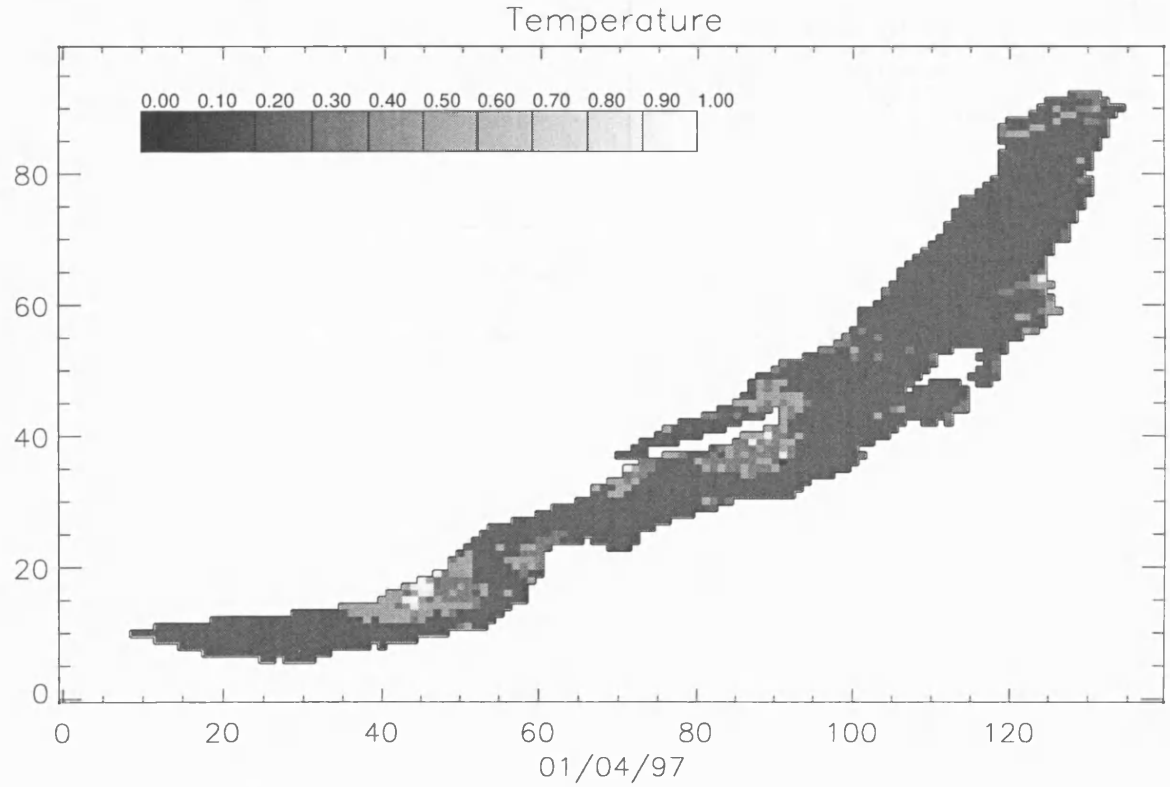

Figure 5.12: Temperature (°C) of top model layer, R2, for 1st April 1997.

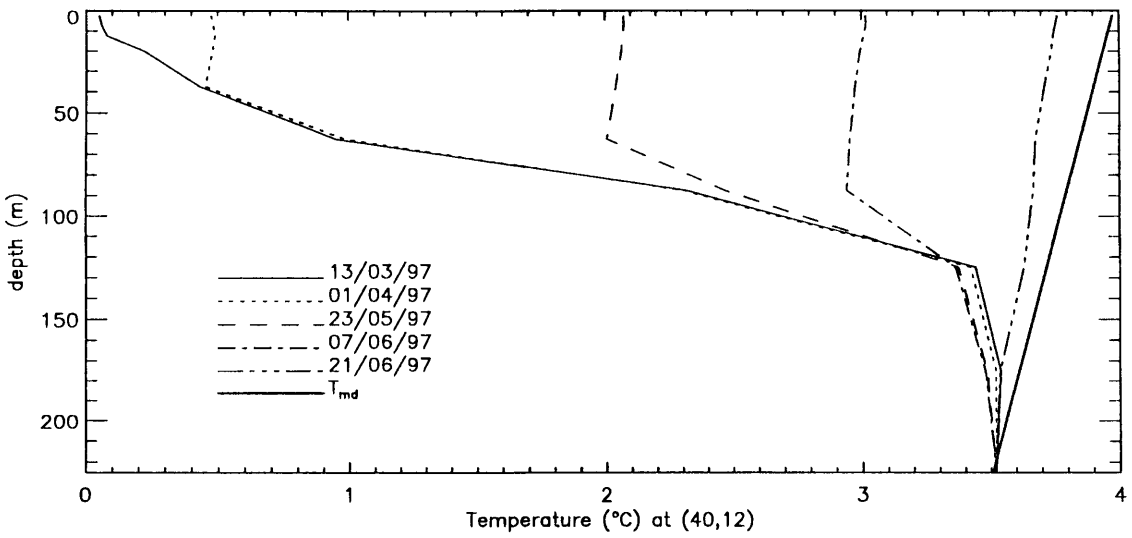

Figure 5.13: Temperature profile at point B for R2 on 13th March, 1st April, 23rd May, 7th June and 21st June.

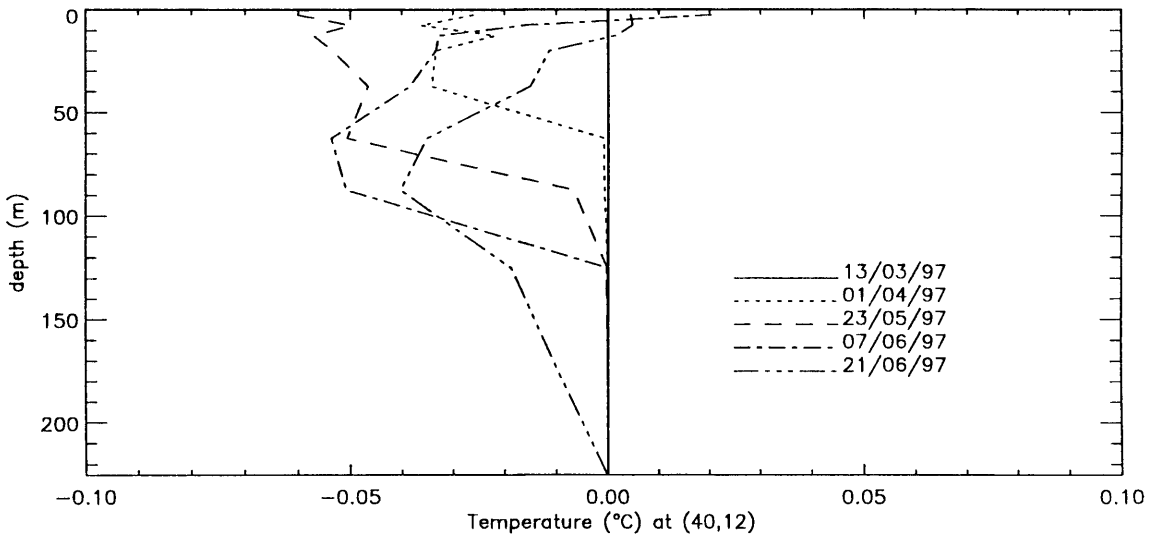

Figure 5.14: Temperature difference profile (R2-R1) at point B for 13th March, 1st April, 23rd May, 7th June and 21st June.

5.8.2 Under-ice currents

As for R1, currents in the top layer flow from low to higher density regions. The strongest currents arise at the boundary between snow-covered and snow-free ice in the South and Central basins, as can be seen in Figure 5.1. The maximum difference in velocity compared to R1, due to the temperature difference, is of the order 10^{-4} ms^{-1} (approximately 5%), but can be either an increase or a decrease depending on the date. On 1st April the velocities tend to be lower than in R1 by about $2x10^{-4}$ ms^{-1}, whereas on 23rd May the velocities are higher by the same amount.

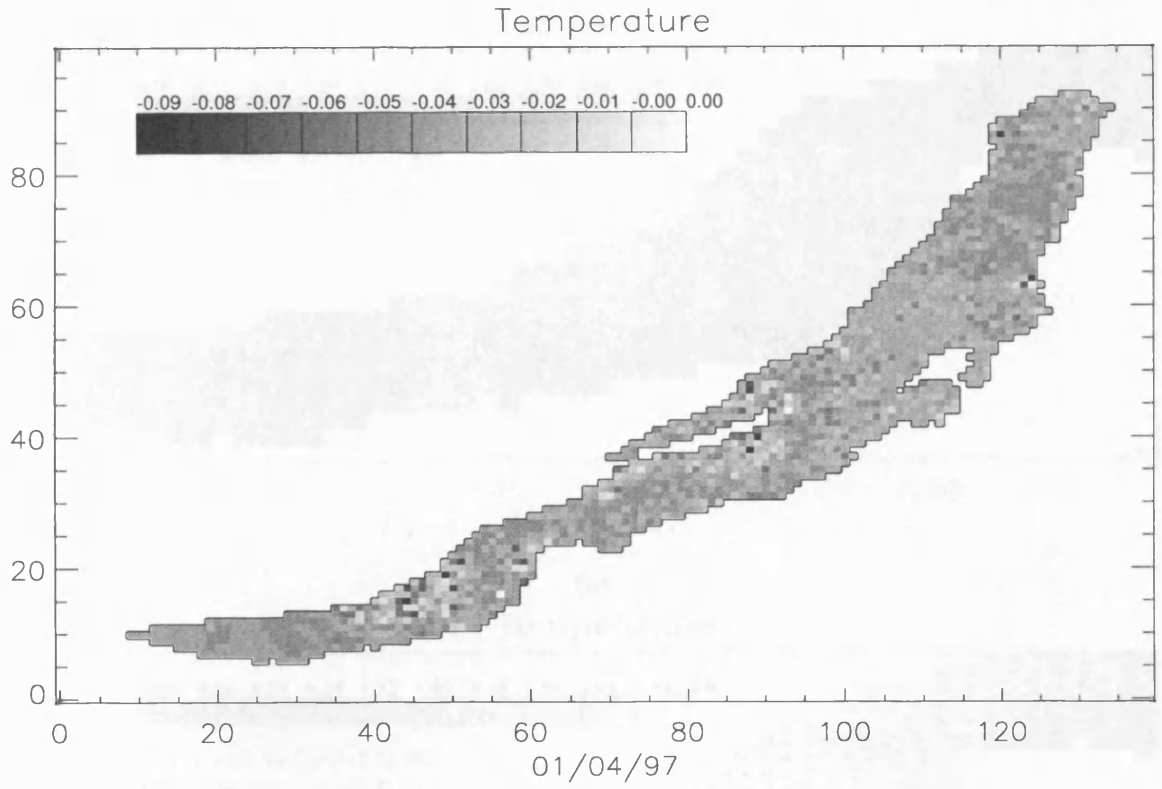

(a)

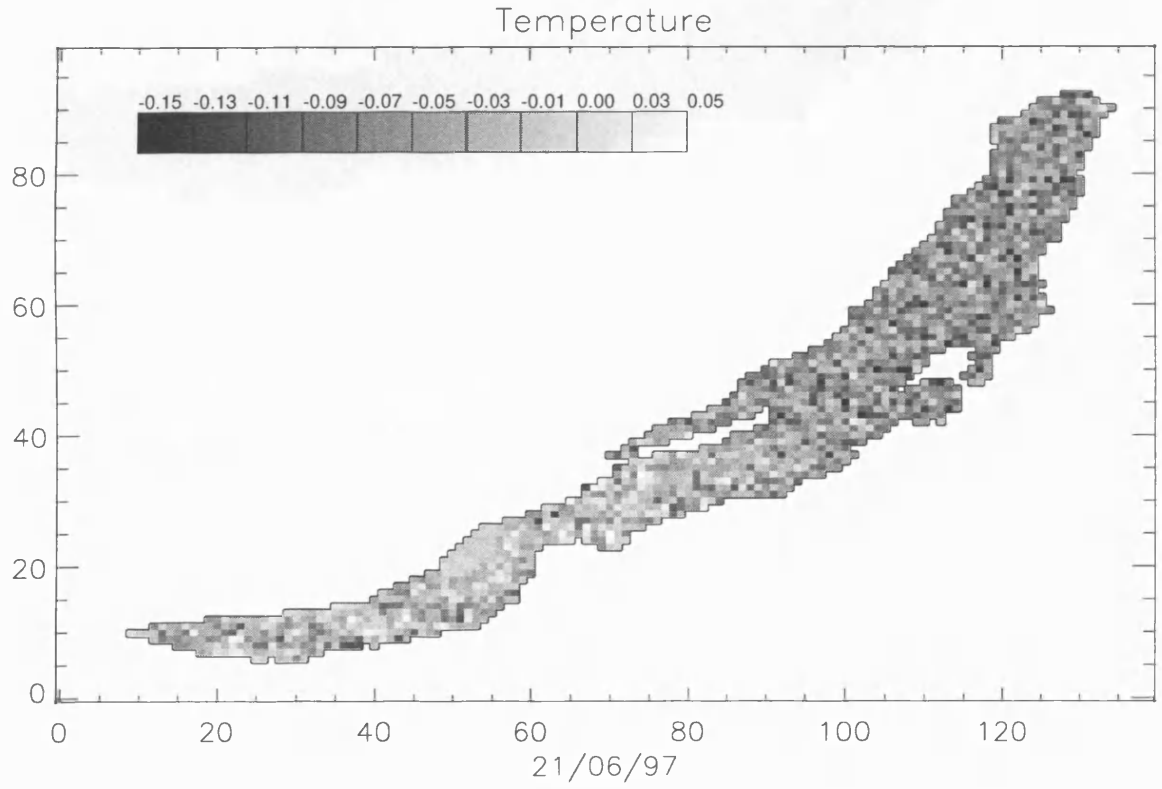

(b)

Figure 5.15: Top layer temperature difference plot (R2-R1) for (a) 1st April and (b) 21st June 1997. R2 is cooler than R1 by a maximum of 0.15°C in the North Basin. The difference between the two runs is almost zero in the South Basin by 21st June.

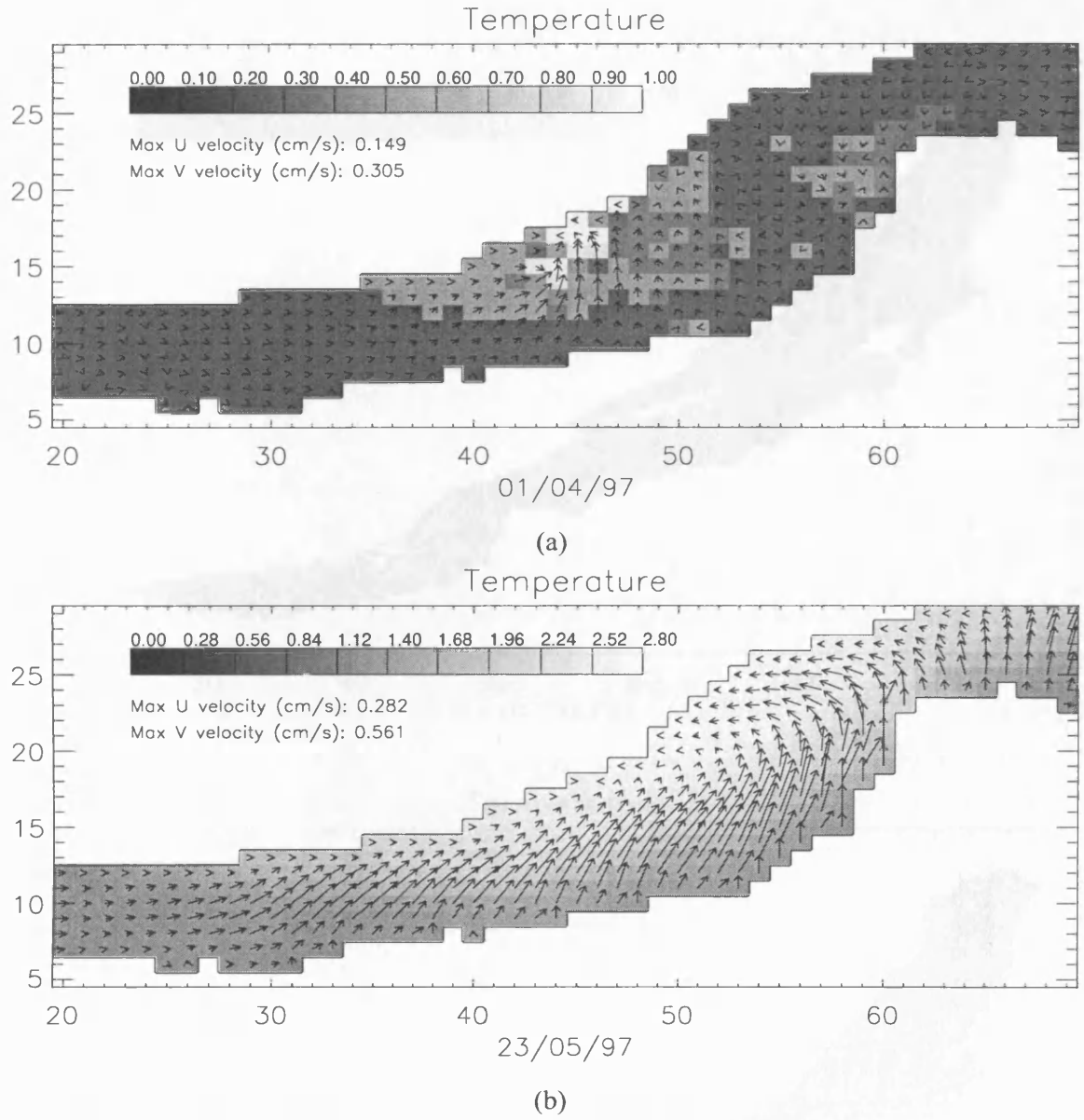

Figure 5.16: Top layer temperature overlaid with velocity field for model run R2 on (a) 1st April and (b) 23rd May. Arrows indicate direction and relative speed of currents. Flow is from low to higher density regions (i.e. towards warmer temperature regions).

5.9 Results for R3 and R4

The aim of model runs R3 and R4 is to investigate the effect of varying the thickness of the snow layer, (t_{snow}) over a realistic range (0.01 m (R3) to 0.04 m (R4)). This is an important parameter to understand, as it cannot be measured from the satellite data and is likely to be highly variable spatially and temporally.

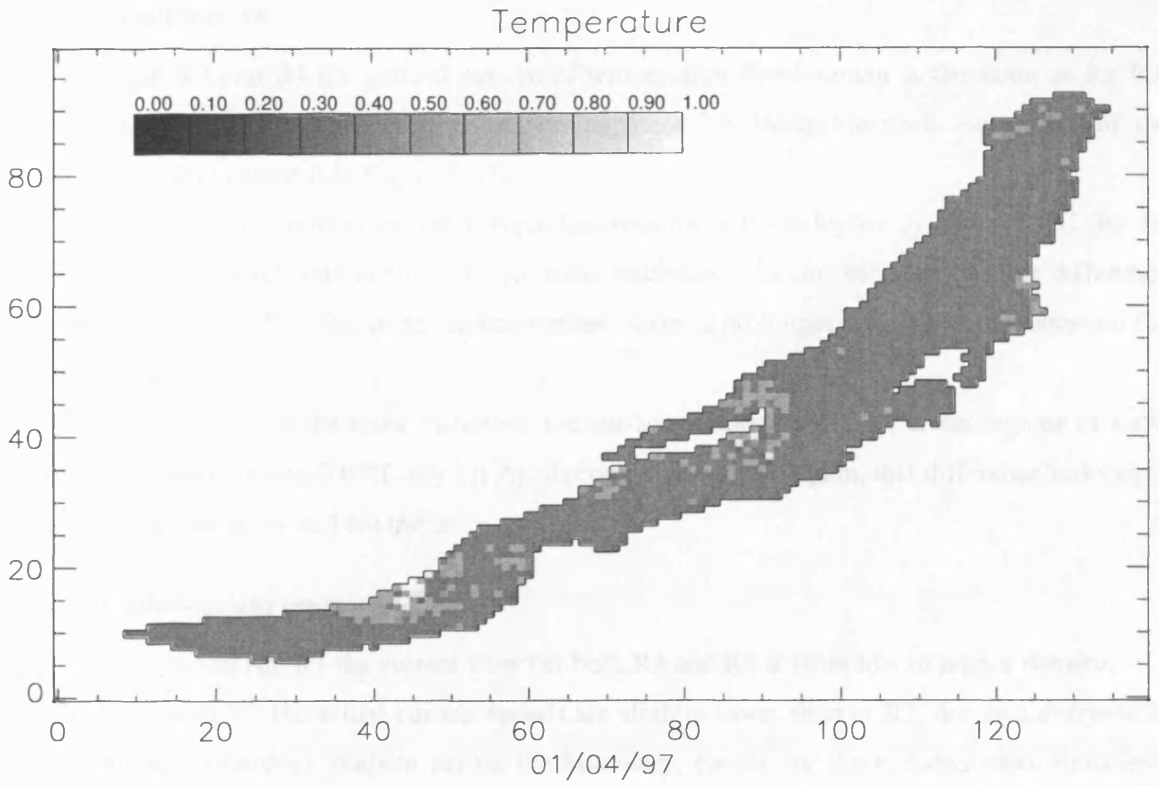

(a)

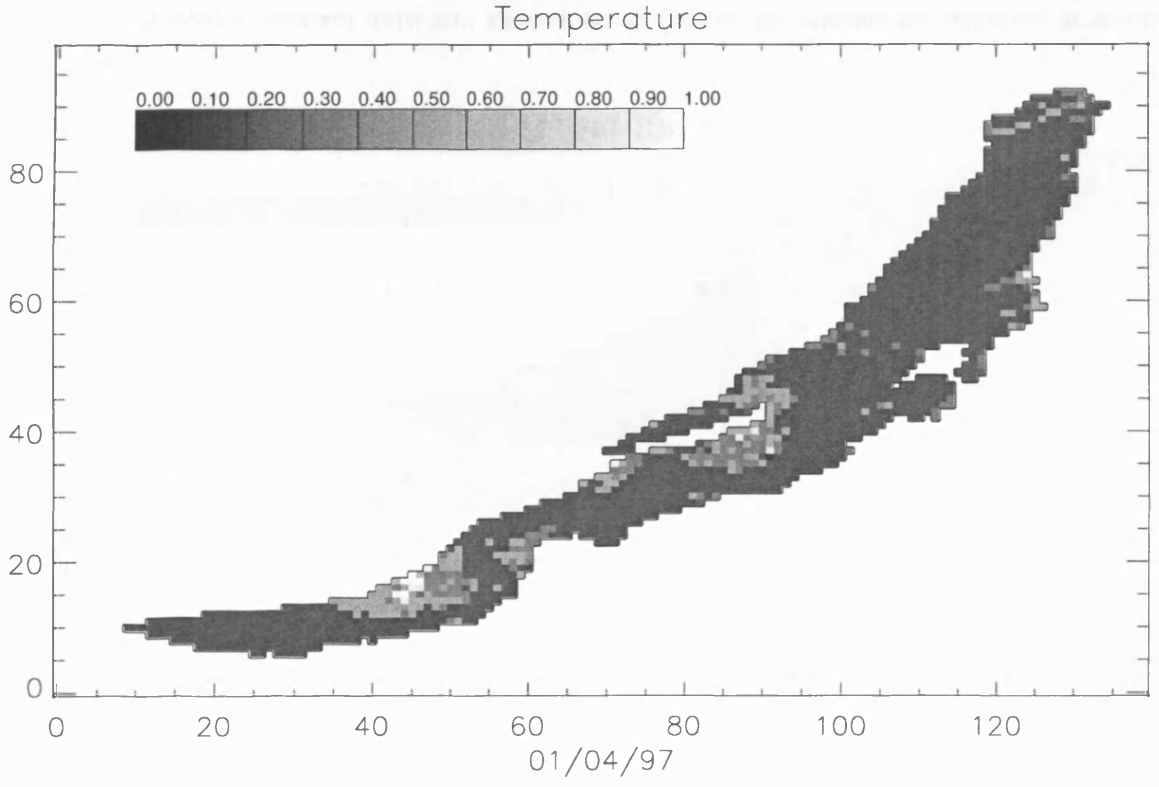

(b)

Figure 5.17: Top layer temperature field for (a) R3 and (b) R4 for 1st April.

5.9.1 Temperature

For both R3 and R4 the general pattern of temperature development is the same as for R1. The highest temperatures occur under semi-transparent ice, along the north-west coast of the South and Central basins (see Figure 5.17).

Under regions of snow cover the surface temperature in R3 is higher by about 0.1°C (by 1st April) compared to R1, due to the reduced snow thickness. As the snow melts, this difference reduces to about 0.03°C. Once the ice has melted, there is no longer any difference between the two model runs.

With an increase in the snow thickness, the surface temperature in R4 under regions of snow cover is reduced by about 0.07°C (by 1st April) compared to R1. Again, this difference reduces to almost zero as the snow and ice melts.

5.9.2 Under-ice currents

As with model run R1 the current flow for both R3 and R4 is from low to higher density.

In model run R3 the actual current speeds are slightly lower than in R1, due to a decrease in the temperature (density) gradient across the boundary, caused by the reduced snow thickness. The maximum difference in current speeds is approximately 4×10^{-4} m s^{-1} (see Figure 5.18), which occurs at the border between snow and snow-free ice (where the currents are strongest at around 3×10^{-3} m s^{-1}).

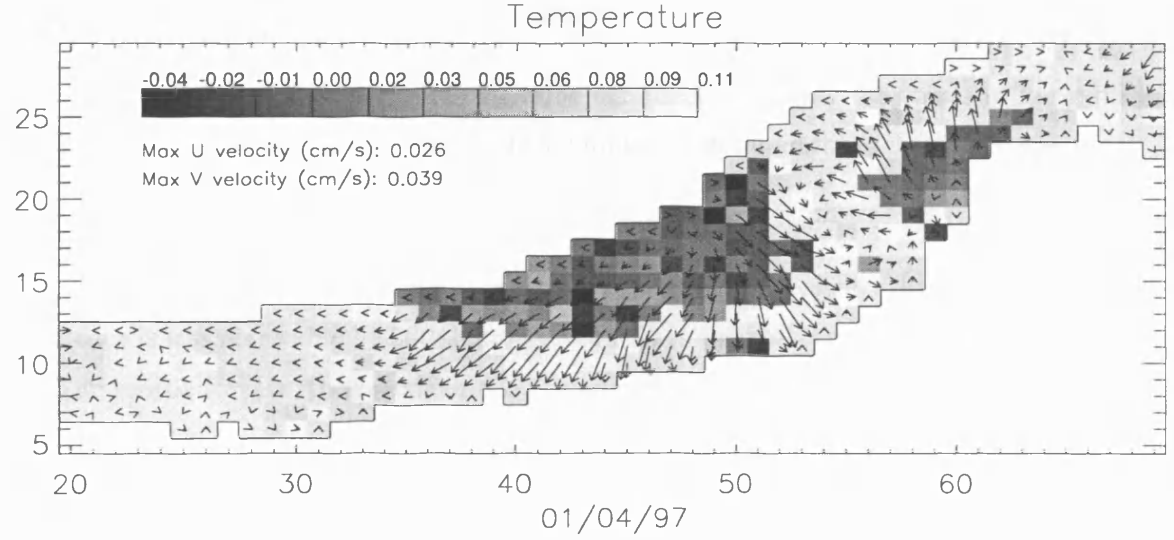

Figure 5.18 Difference between temperature (°C) and velocity fields for R3-R1 for 1st April.

The increased snow thickness in R4 results in a maximum increase in current speed of about 2×10^{-4} ms^{-1} (see Figure 5.19), which again occurs at the border between snow and snow-free ice (where the currents are strongest at around 3×10^{-3} ms^{-1}). This difference is due to an increase in the temperature (density) gradient across the boundary, caused by the increased snow thickness.

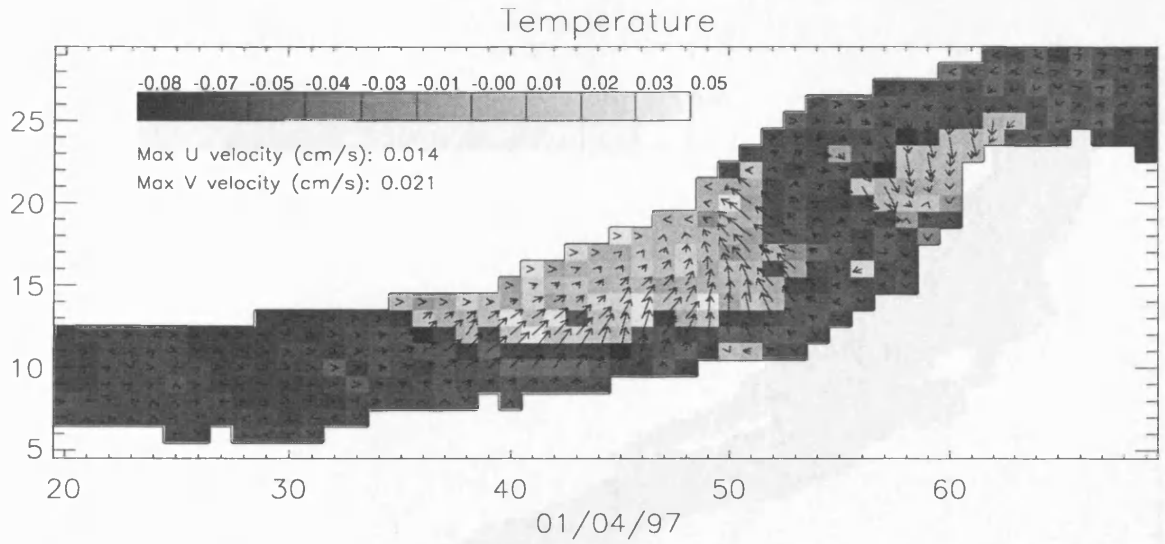

Figure 5.19: Difference between temperature and velocity fields for R4-R1 for 1st April.

5.9.3 Summary

Decreasing or increasing the snow thickness by 0.015 m results in a maximum increase/decrease in the top layer temperature of 0.1°C, and a maximum decrease/increase in the current speeds of about $4x10^{-4}$ ms^{-1}. The effect is most noticeable initially, when the lake is predominantly snow covered.

5.10 Results for R5

The aim of model run R5 is to determine the effect of varying the values of the extinction coefficients for each type of ice. See Table 5.2 for the values used for each surface type.

5.10.1 Temperature

The development of the temperature profile is initially much slower than in R1, although this difference is less noticeable by 26th June. Figure 5.21 is a plot of the temperature profiles at point B. The profile for 1st April is about 0.2°C cooler than for R1 in Figure b, but by 7th June the difference has reduced to almost zero.

Figure 5.20 shows how the top layer temperature in R5 differs from that in R1. On 1st April the difference between the two model runs occurs for regions with a semi-transparent ice cover, which results in a relative decrease in the temperature of around 0.3°C. Under snow-covered regions, the temperature decrease is slightly less. By 26th June, the temperature difference in the South Basin is almost zero, while in the North Basin the temperature is still considerably lower (by about 0.2°C).

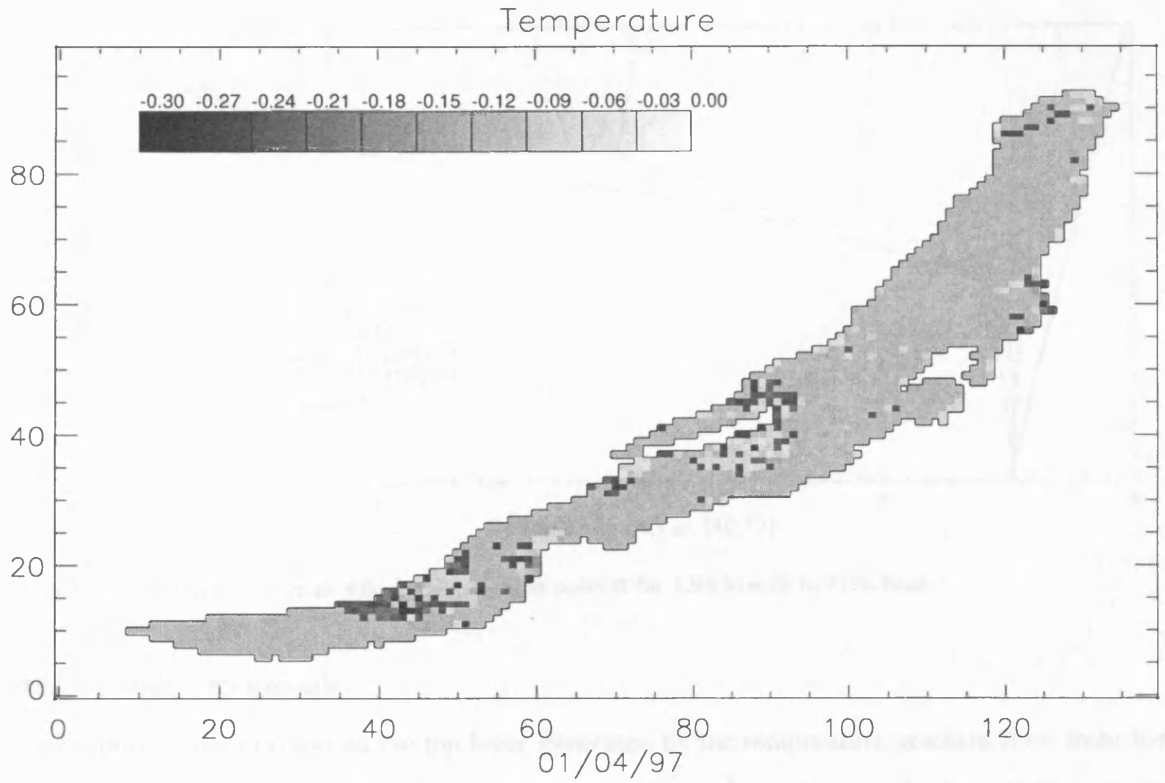

(a)

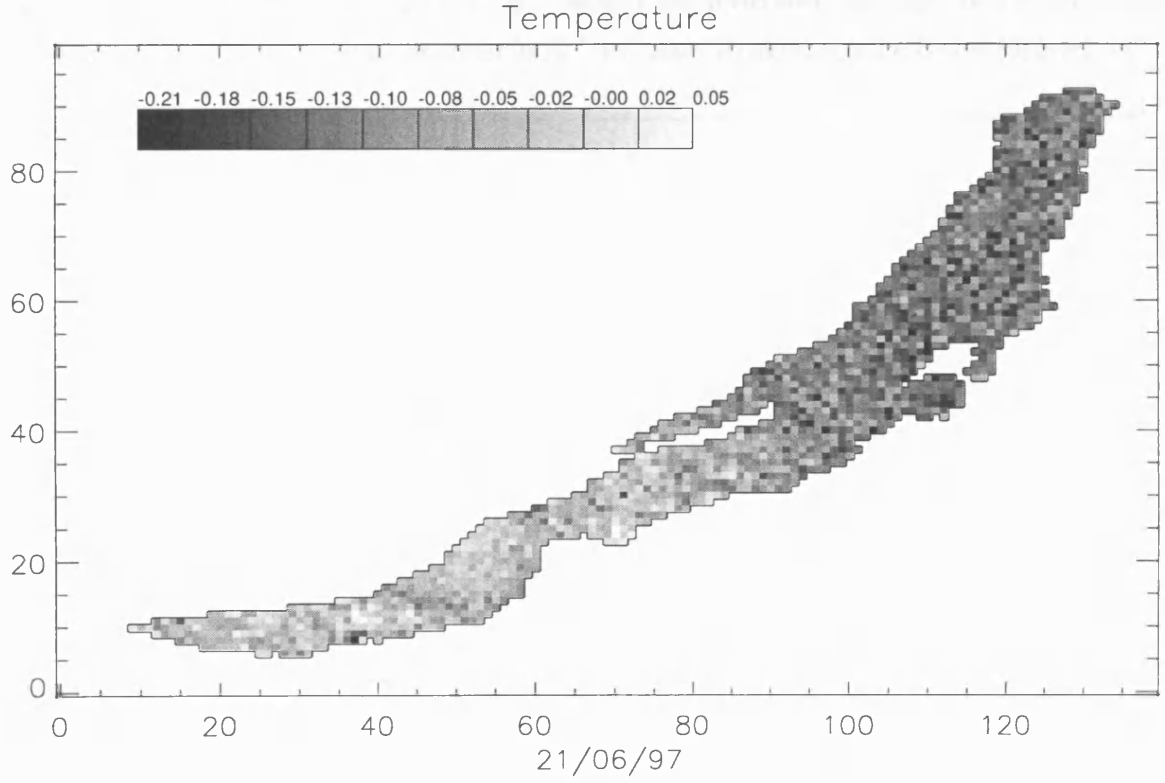

(b)

Figure 5.20: Top layer temperature difference, R5-R1, for (a) 1st April and (b) 21st June.

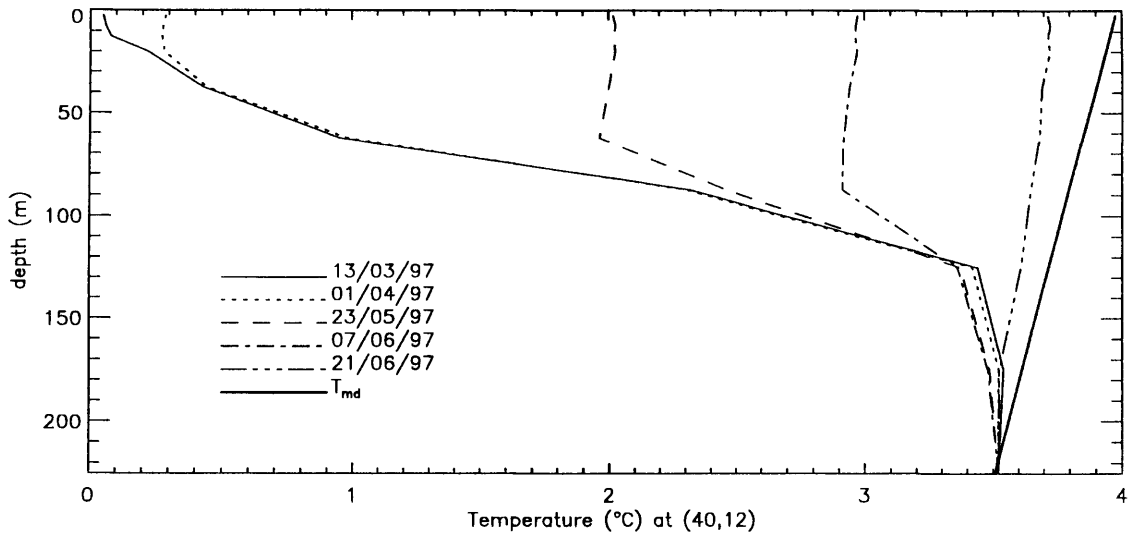

Figure 5.21: R5 temperature profile development at point B for 13th March to 21th June.

5.10.2 Under-ice currents

As before, the currents in the top layer generated by the temperature gradient flow from low to higher density, with maximum speeds of about $6x10^{-3}$ ms^{-1} occurring at the boundaries between snow and snow-free ice (see Figure 5.23). Initially the difference between the current speeds between R5 and R1 is a decrease of about $2x10^{-4}$ ms^{-1} after 10 days, at point B (see Figure 5.22).

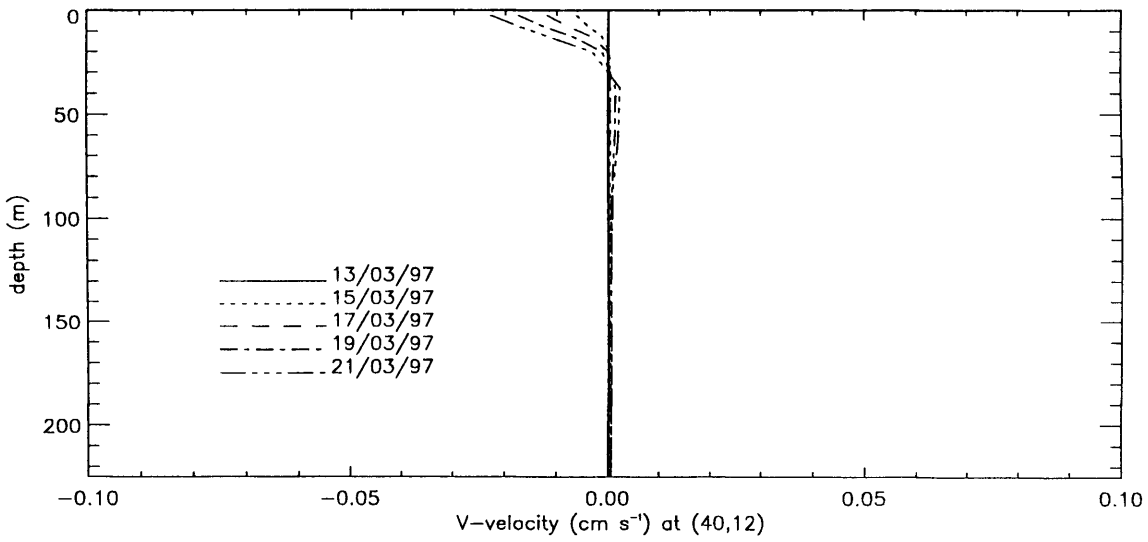

Figure 5.22: Difference between y-direction velocity profiles for R5-R1 for 13th March to 21st March.

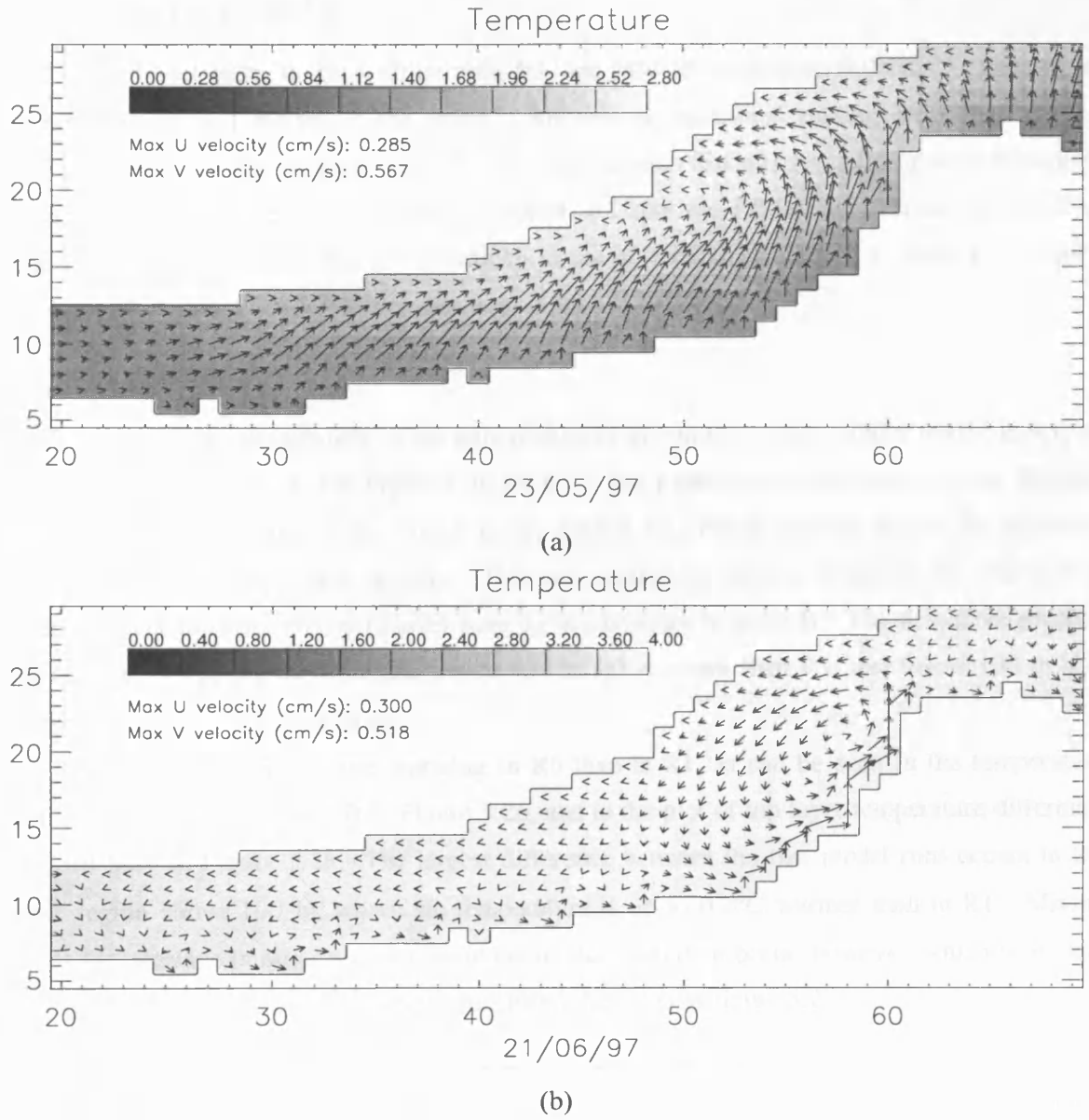

Figure 5.23: Temperature and velocity field for R5 on (a) 23rd May and (b) 21st June.

5.10.3 Summary

Increasing the extinction coefficients results in a small reduction in the temperature in the model lake (by about 0.2°C) initially. The overall development of the temperature profile is, however, relatively unaffected, in that there is little difference between the final (21st June) temperature profiles in model runs R5 and R1. Comparing the profile plot for R5 in Figure 5.21 with that for the *in situ* data in Figure 5.5 implies that the values for the extinction coefficients used in R5 actually produce a slightly more realistic development of the temperature structure than those used in the other model runs.

5.11 Results for R0 and R6

These model runs, in conjunction with R1, are used to investigate different techniques to parameterise vertical mixing in the model. R0 uses no additional mixing other than simple convective overturn; R6 uses the *Fixed Profile* method, such that mixing is strongest in the upper layers, and is independent of the density gradient; R1 uses the *PP variant* scheme discussed in Section 5.4.5 above which models mixing in terms of vertical stability (i.e. density gradient), coupled with the depth-dependent profile used in R6.

5.11.1 Temperature

In general, the development of the temperature profile in R0 is very similar to that in R1, as can be seen in Figure 5.24 (and Figure 5.5b for R1). The most obvious difference is that R0 does not produce a deepening of the mixed layer, caused by vertical mixing across the interface between the upper and lower regions. This can clearly be seen in Figure 5.25, which is a difference plot between the two model runs for temperature at point B. The first three profiles (1st April to 7th June) all show that above 100 m R0 is cooler than R1, and below 100 m it is warmer, by about 0.5°C on average.

There is considerably more warming in R6 than in R1, as can be seen in the temperature profile plots for points A and B in Figure 5.26, and in the plot of top layer temperature difference for 23rd May in Figure 5.28. The largest difference between the two model runs occurs in the upper region above 100 m, where the temperature is up to 0.2°C warmer than in R1. Mixing across the interface (similar to that seen in the *in situ* data) does occur, however, which is evident from the cooling of the profile in the region 100 to 225 m (see Figure 5.27).

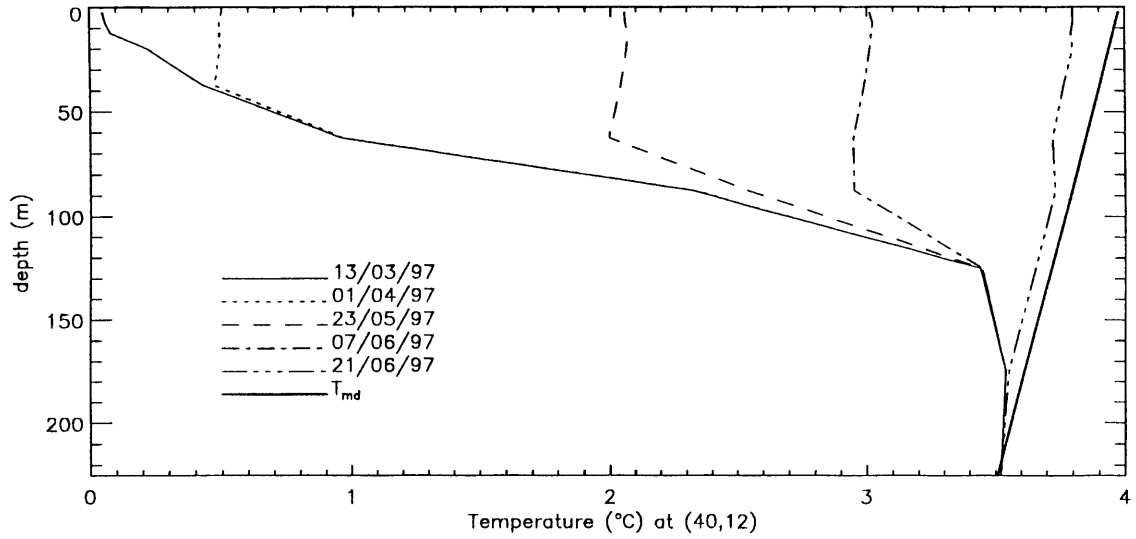

Figure 5.24: Temperature profile development for R0 at point B, from 13th March to 21st June.

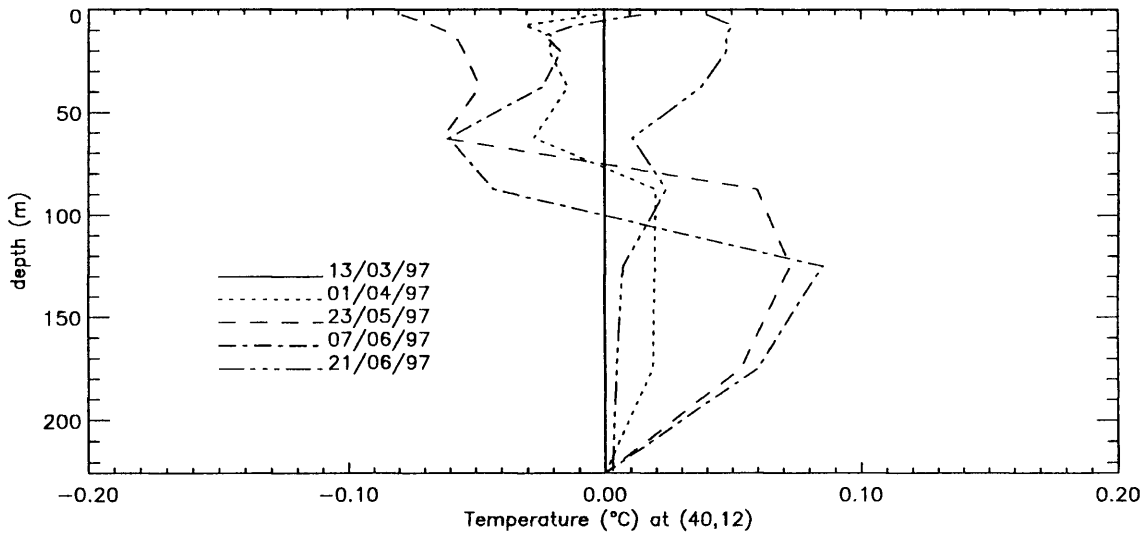

Figure 5.25: Temperature difference between R0 and R1 at point B, from 13th March to 21st June. Above 100 m the temperature in R0 is cooler than R1, but is warmer below 100 m.

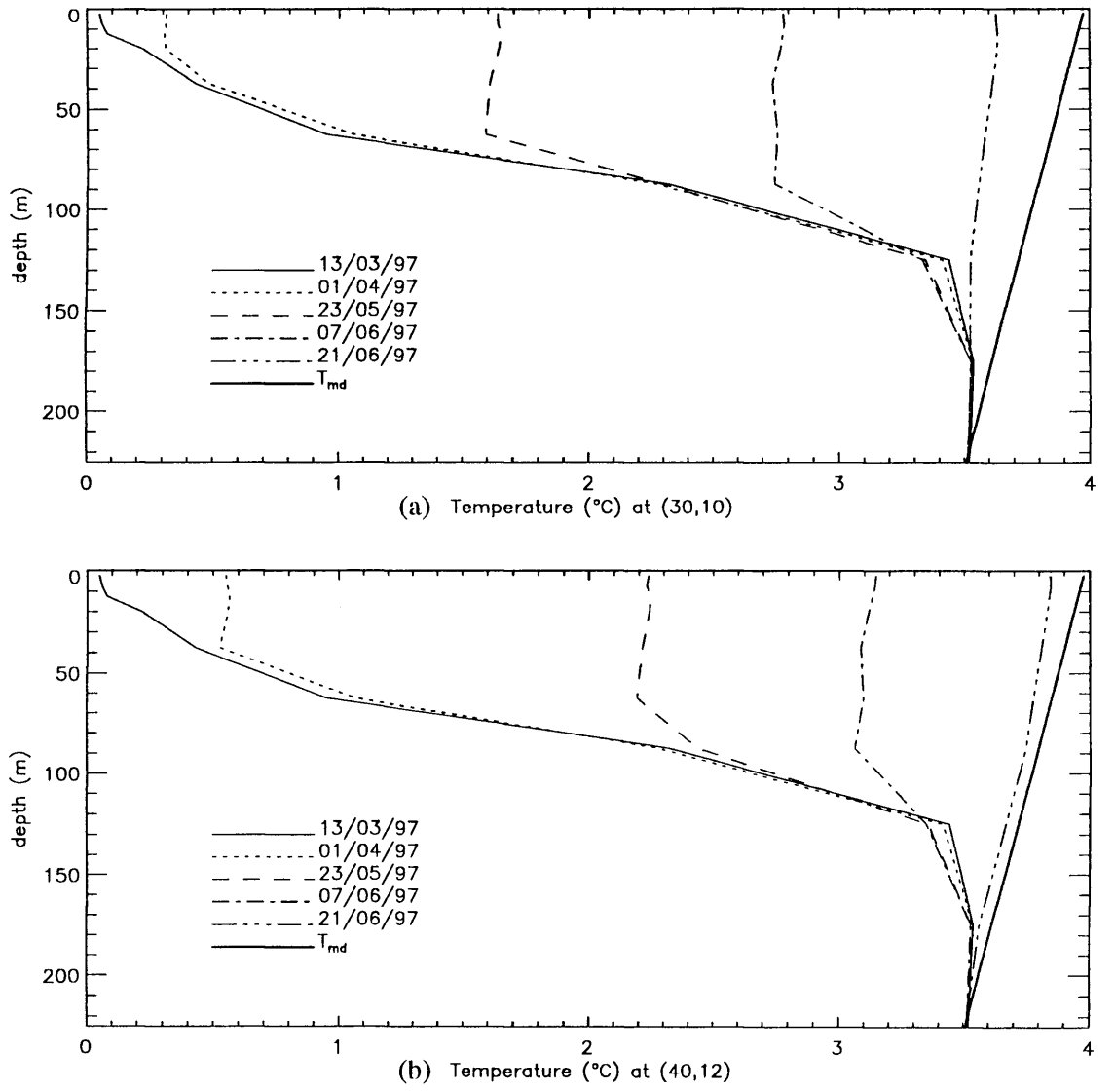

Figure 5.26: Temperature profile development for R6 at points (a) A and (b) B, from 13th March to 21st June.

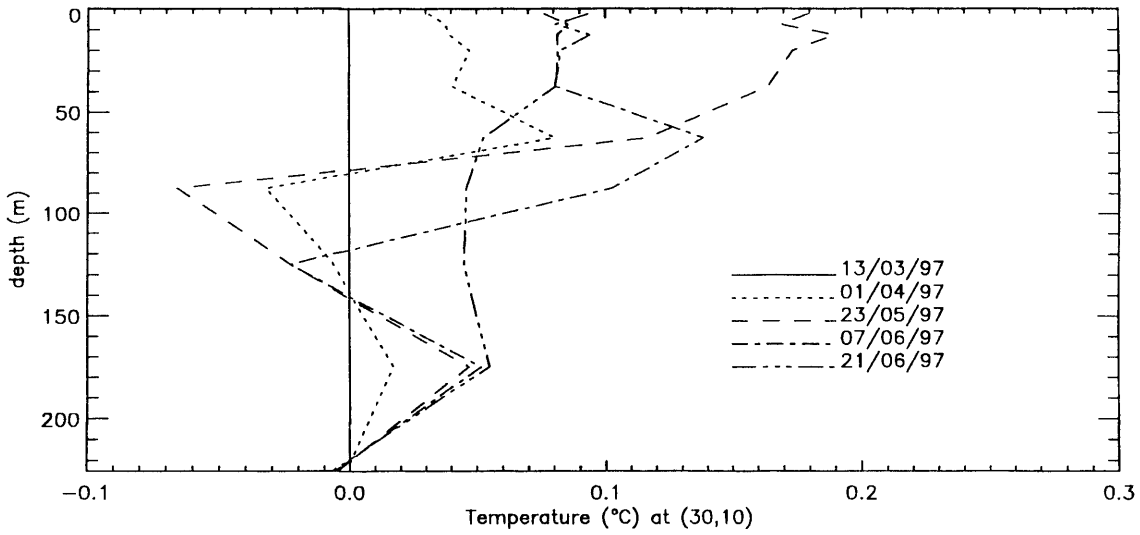

(a)

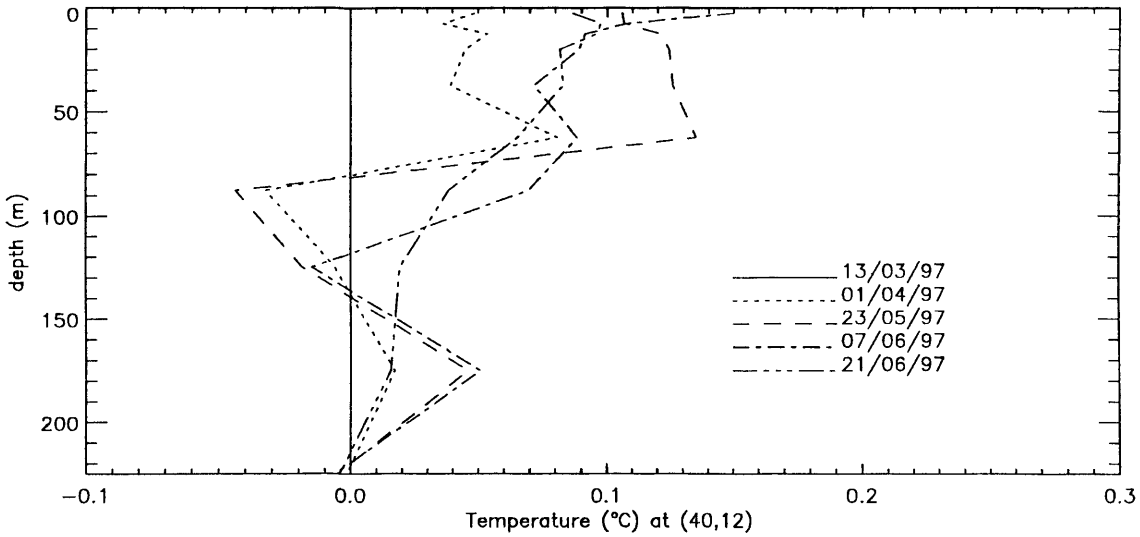

(b)

Figure 5.27: Temperature difference between R6 and R1 at points (a) A and (b) B, from 13th March to 21st June. At about 100 m the temperature in R6 is cooler than R1, but above and below this level it is warmer by up to 0.2°C.

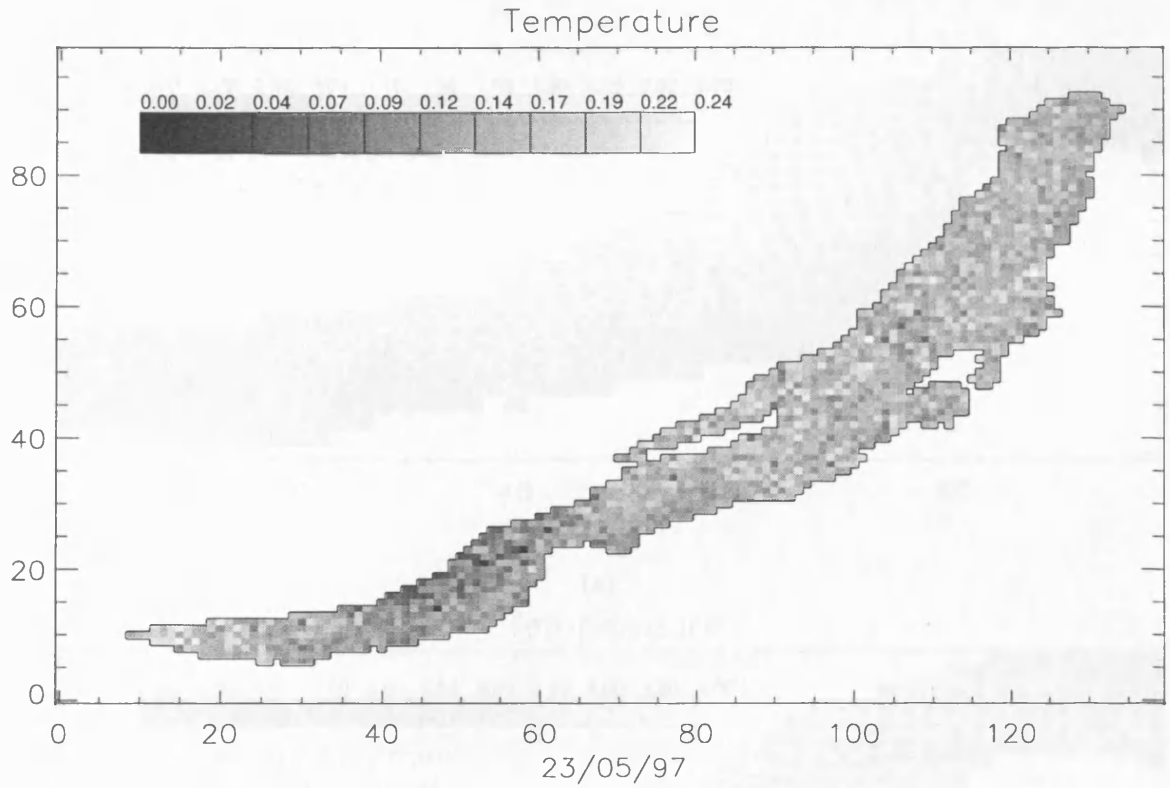

Figure 5.28: Top layer temperature difference plot for R6-R1. The whole of the top layer is warmer in R6 than in R1, with the greatest difference occurring in regions of snow-covered ice.

5.11.2 Under-ice currents

The direction of the currents in R0 and R6 are again approximately the same as in R1 (Figure 5.29 and Figure 5.30). In R0 the speeds are almost exactly the same, differing by less than 5×10^{-5} ms^{-1} at point B (Figure 5.31a), but in R6 they tend to be slower by up to about 1×10^{-3} ms^{-1} in the top few tens of metres (Figure 5.31b). The slight drop in current speed is due to a reduction in the temperature/density gradient at the snow/snow-free boundary.

5.11.3 Summary

The development of the temperature profile using no additional vertical mixing scheme, as in R0, is slightly unrealistic, with no deepening of the mixed layer indicating that there is little or no transfer of heat across the interface. The temperature of the upper layer is, however, consistent with the *in situ* data used here.

When a *fixed profile* mixing scheme is implemented, the interface between the mixed layer and the stratified region below 100 m does deepen as observed in the *in situ* data. However, the temperature of the upper mixed layer is now slightly warmer (by ~0.2°C) than the observation. This results in a small decrease in the top layer current speeds.

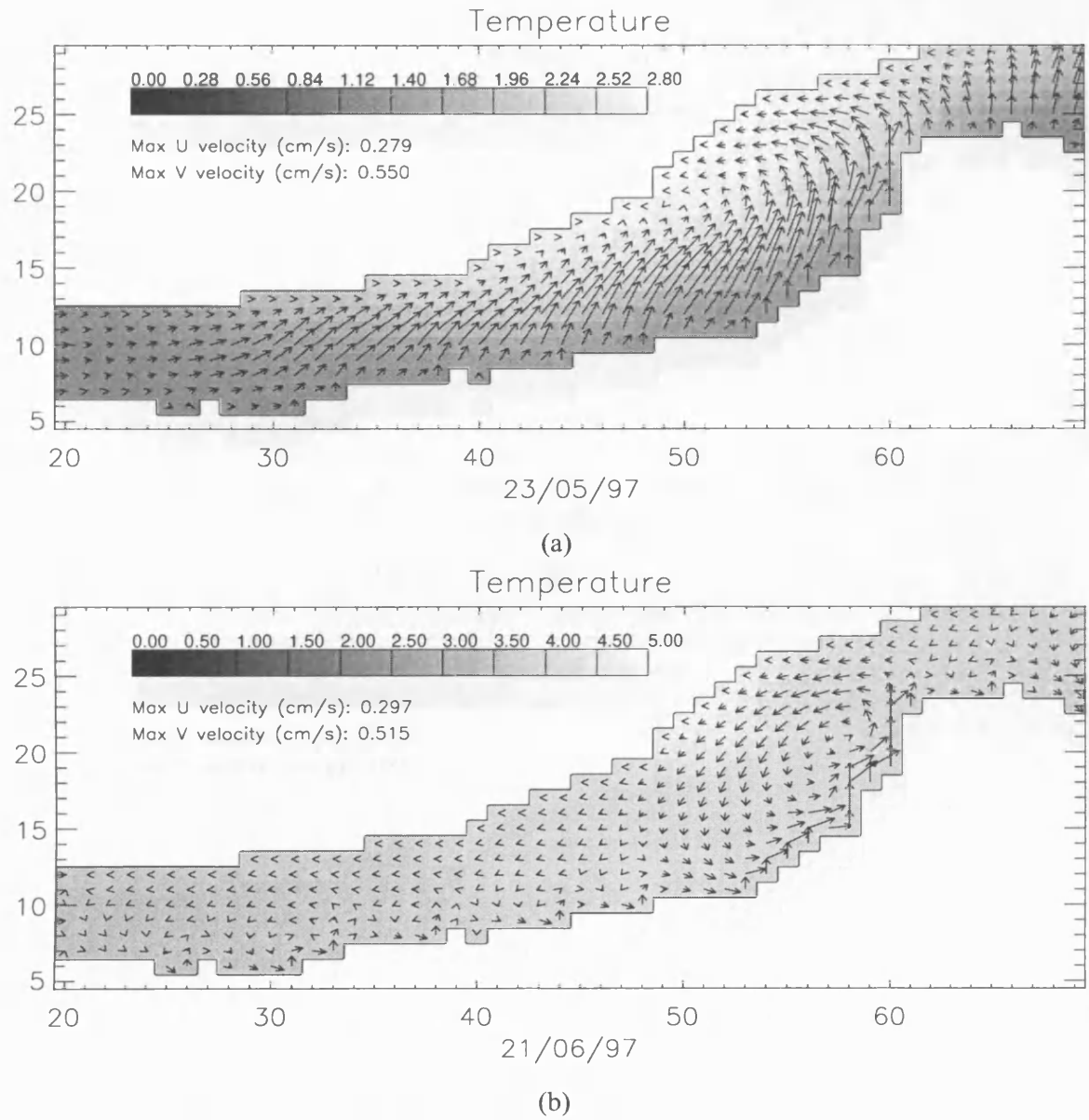

Figure 5.29: Top layer temperature and velocity fields for R0 on (a) 23rd May and (b) 21st June.

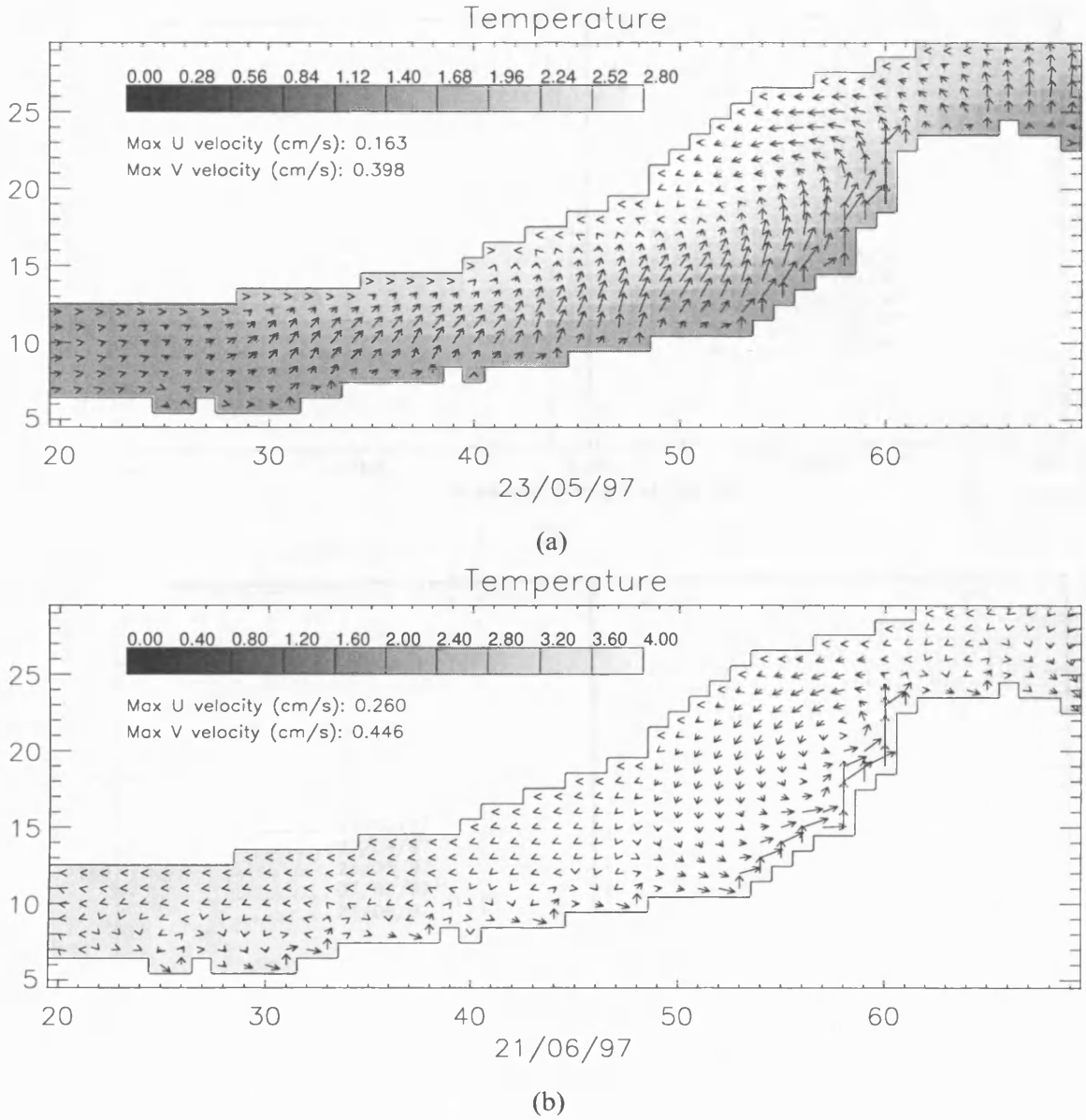

Figure 5.30: Top layer temperature and velocity fields for R6 on (a) 23rd May and (b) 21st June.

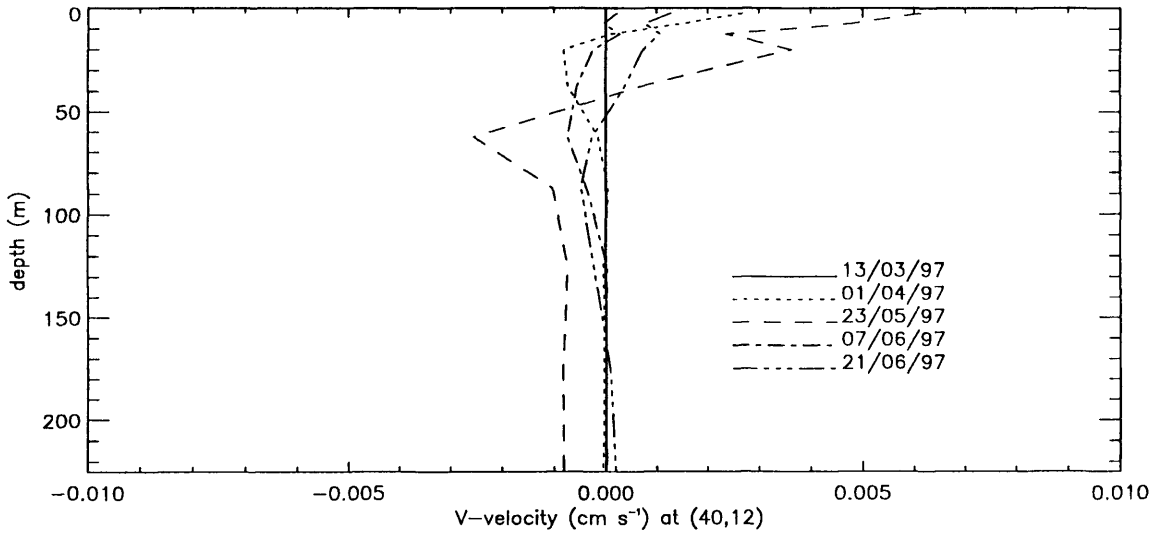

(a)

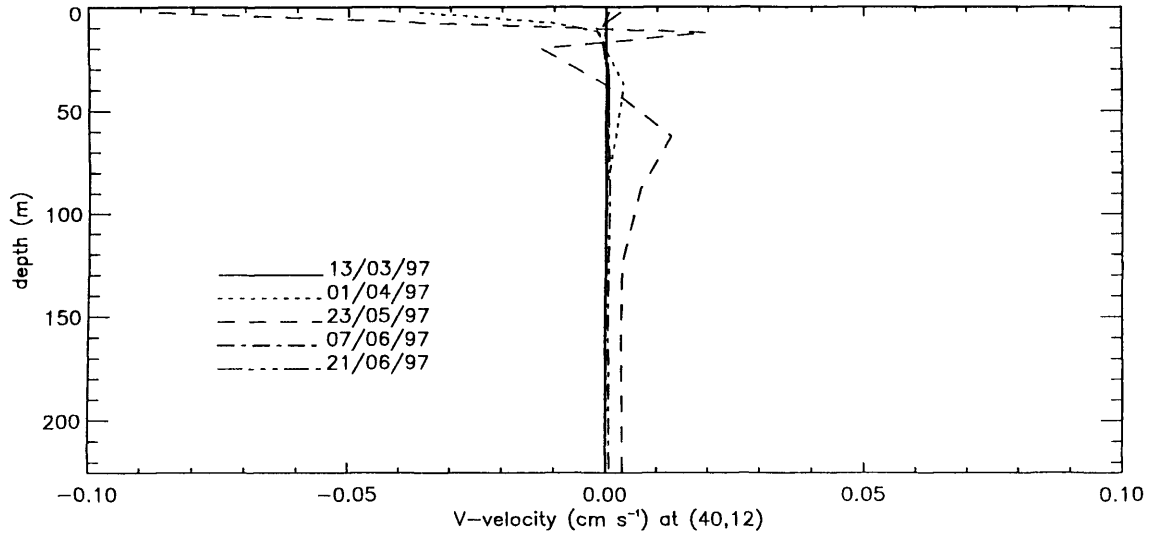

(b)

Figure 5.31: y-direction velocity difference for (a) R0-R1 and (b) R6-R1 at point B, for 13th March to 21st June.

5.12 Model runs investigating internal waves

Deep water ventilation due to thermobaric instability can only occur if the temperature above the mesothermal maximum T_{mm} is colder than that below, i.e. less than about 3.45°C. For a cold water jet to penetrate to the bottom of the lake, as observed by Shimaraev *et al.* (1993), the upper layer must have a temperature of about 3.3°C at most.

To investigate the formation of internal waves which could lead to a thermobaric instability (Carmack and Weiss, 1991), the model is run using two layers. The upper layer is initialised with a thickness of 250 m and a temperature (T_1) of 3.3°C, while the lower layer has a 50 m thickness and a temperature (T_2) of 3.45°C. Note that due to the formulation in the model of the equation of state with depth, the lower layer thickness cannot extend deeper than this (with the given temperature initialisation) or the initial situation will be unstable. A surface wind stress is applied to generate both surface and internal waves.

Given these initial conditions, the compensation depth H_c is 288 m. This means that for a thermobaric instability to occur, the interface between the two layers must be depressed to a depth of 288 m, i.e. the internal wave must have an amplitude of about 40 m.

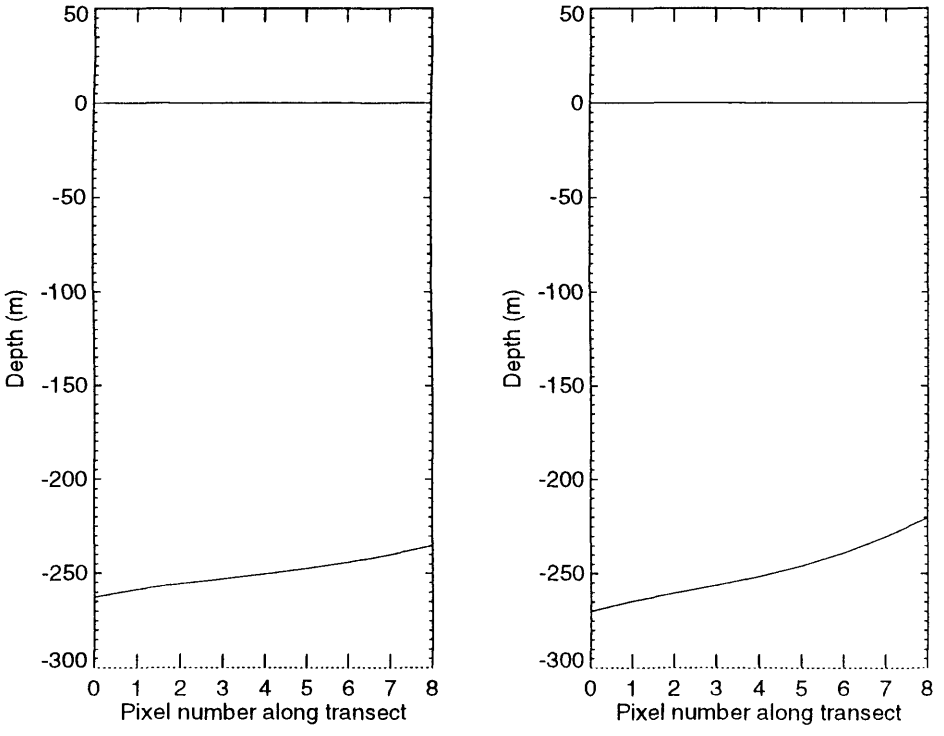

Figure 5.32: Transect across the model lake showing the positions of the layer interfaces after (a) one day and (b) two days. Initial layer temperatures are 3.3°C (upper layer) and 3.45°C (lower layer). The depth is relative to the initial position of the surface of the top layer (0 m). The interface between the two layers initially lies at a depth of 250 m. Motion of the interface is due to an applied constant north-westerly wind stress, of speed 30 ms^{-1}.

Figure 5.32 is a cross-section across the middle of the lake (south to north) showing the positions of the layer after one day (Figure 5.32a) and two days (Figure 5.32b), with a constant north-westerly wind speed of 30 ms^{-1} applied to the surface. After one day the interface has been displaced downwards at the south edge to a depth of 262 m, and upwards at the north edge to a depth of 235 m. After two days the interface has deepened further to 270 m (about 18 m short of the depth necessary to cause thermobaric instability), while the upwards displacement has increased to give a minimum interface depth of 220 m. The slight difference in interface displacement from south to north is due to entrainment of cold water from the lower layer to the upper layer as the interface is depressed downwards. Entrainment timescales are of the order of one day, i.e. after one day entrainment has had little effect on the depth of the interface. The difference in interface displacement from south to north becomes increasingly more noticeable with time. Continuing the model run results in a continued upwelling of the interface in the north, while the maximum depth reaches, and remains at about 285m. However, it is unrealistic to run the model with such a high constant wind stress for more than about a day, so results from Figure 5.32b should be considered to be the outer limit for this run.

The model was run again with T_1 = 3°C and T_2 = 3.45°C to determine how critical the initial layer temperatures are to the amplitude of the interface wave. Results from the model show that interface displacement is approximately the same as the previous run with T_1 = 3.3°C. This suggests that small differences in the initial layer temperatures are not critical to the internal wave amplitude. However, the compensation depth using this lower temperature for T_1 is now 312 m (using Eq. 5.3), which makes the generation of a thermobaric instability more unlikely.

Using the original initial layer temperatures of 3.3°C and 3.45°C the model was run again using stronger north-westerly winds of 50 m s^{-1}. Figure 5.33 is a cross-section across the middle of the lake (south to north) showing the positions of the layer after one day (Figure 5.33a) and two days (Figure 5.33b). After one day the interface has been displaced downwards at the south edge to a depth of 278 m, and upwards at the north edge to a depth of 207 m. In Figure 5.33b the interface has deepened further to 286 m, while the upwards displacement has increased to give a minimum interface depth of 170 m. The depth of the interface has, therefore, virtually reached the compensation depth (i.e. the depth at which a thermobaric instability may arise).

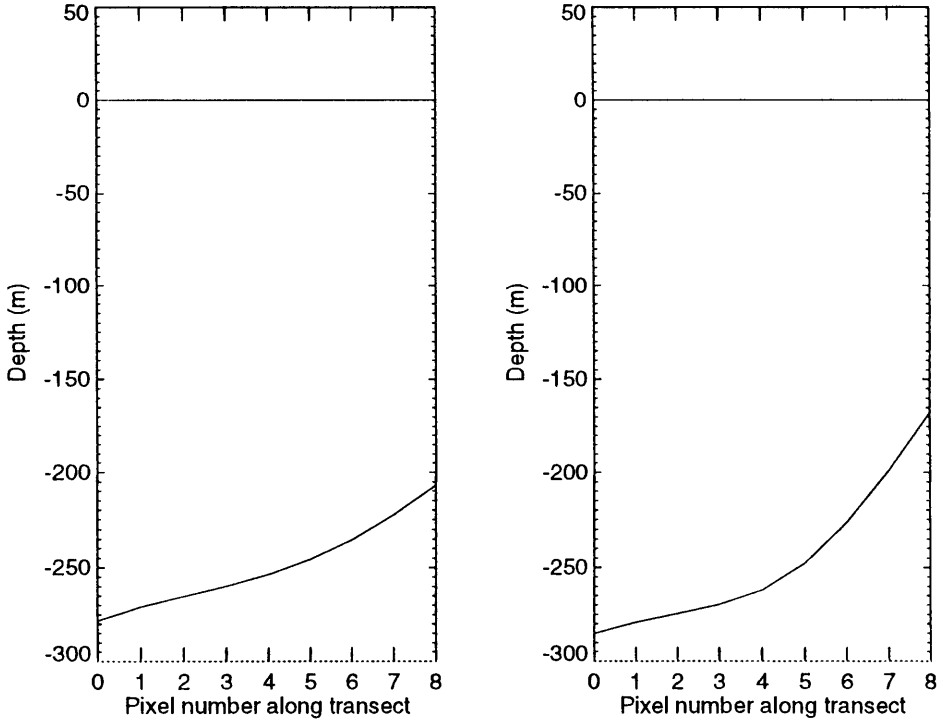

Figure 5.33: Transect across the model lake showing the positions of the layer interfaces after (a) one day and (b) two days. Initial layer temperatures are 3.3°C (upper layer) and 3.45°C (lower layer). The depth is relative to the initial position of the surface of the top layer (0 m). The interface between the two layers initially lies at a depth of 250 m. Motion of the interface is due to an applied constant north-westerly wind stress, of speed 50 ms^{-1}.

6. Conclusions and Summary

6.1 Conclusions

- Current flow in the multi-layer baroclinic model is caused by differential under-ice heating, and has a direction consistent with observation, i.e. from cool, low density regions to warmer, higher density regions. Current strengths are, however, an order of magnitude less than those observed in the real lake.

- Model-generated temperature profiles show evidence of convective mixing under snow-free ice. Negligible mixing was evident under snow-covered ice.

- Model runs investigating the conditions required to cause deep water ventilation (DWV) events show that wind-induced thermobaric instabilities (thought to be a mechanism for DWV) are possible, although the high wind speed and strength required suggests these events would be rare in the real lake.

- A methodology has been developed to produce classification maps of snow and ice cover on the lake using thermal and visible wavelength satellite data. These maps were integrated into the multi-layer baroclinic model to determine the extent of under-ice heating, by assigning known values of albedo and extinction coefficient to each surface type.

- Eddy structures (similar to the observed gyres) were generated in the single-layer barotropic model, due to a combination of forcing from a north-westerly wind, the basin topography around the Academician Ridge, and the Coriolis effect.

- A number of physical processes which occur in the lake were observed with satellite data, including thermal bars, gyres, coastal upwelling and suspended sediment plumes. The five month period of ice cover was also monitored in detail for 1997.

6.2 Summary of results

6.2.1 Satellite data

Thermal bars have been observed in satellite data from the spring warming period of 1993 and 1995, primarily around the Selenga Delta region of the lake. Histogram plots of lake pixel brightness temperature were used to determine for each image the BT equivalent to 4°C (the temperature of maximum density) and hence the exact location of the thermal bars in each image. However, quantitative analysis of thermal bars was restricted due to extensive cloud cover during this time.

Warm circular or spiral features known as gyres, about 30 km in diameter, have been observed in satellite images in the region of the Academician Ridge. These persist for several weeks when present in October and November, but are shorter lived and more open in structure when present in the summer months of July and August. Quantitative analysis of gyres as a mechanism for deep water ventilation was prevented due to the difficulty in obtaining wind data in the Lake Baikal region.

Upwelling of cool hypolimnetic water was observed as regions of water at about 4°C in satellite data for July 1993.

Regions of relatively high reflectance (about five times greater than the surrounding water) have been observed in satellite images from October 1994. They appear to originate from four river mouths along the south-east coast of the South and Central Basins, and spread out in to the middle of the lake, covering areas over 100 km^2. Comparison between *in situ* bulk temperature and satellite BT show that the BT in the high reflectance region is cooler by between 0.2 and 1.0°C. *In situ* measurements show that light transmission in the same location was lower than in the surrounding water, and that a severe storm had passed over the lake during the previous few days. It is concluded that these 'plumes' are an indication of the presence of suspended sediment, washed down from the rivers by the storm.

6.2.2 Ice and snow cover

The period of ice cover on Lake Baikal has been observed using satellite data for 1997. Formation of ice begins in the North Basin at the end of December and is complete by the end of January. Ice melt starts in the South Basin towards the end of April and proceeds throughout May to become ice-free by the beginning of June.

The primary aim of analysing the ice covered period was to produce a time series of 'maps' of albedo and extinction coefficients for use in a numerical model of Lake Baikal.

Thermal wavelength data (11-12 μm) from the ATSR instrument can be used to differentiate between types of surface cover on the lake (e.g. water, ice and snow) by analysing histogram plots of brightness temperature. Threshold BT values given by the location of minima in the histogram plots are used to classify pixels into different types. Classification plots produced from

this information show the location of boundaries between these different surfaces which may not show up clearly in visible images due to similarities in albedo. These boundaries will appear in a BT image as a clear interface because the two surfaces have slightly different emissivities (and/or temperature). This method of determining the actual type of surfaces involved (e.g. whether the interface is water/clear ice, white ice/snow-covered ice etc.) was not considered to be sufficiently accurate for use in a numerical model requiring surface albedo (reflectance). This type of analysis would be useful in the absence of visible channels, for example with data obtained prior to the launch of ATSR-2, or for using in conjunction with other methods (discussed below).

Visible wavelength data (0.55 - 0.87 μm) from ATSR-2 were analysed in a similar manner (i.e. using histogram plots) to produce classification images showing regions of snow, ice and water. To some extent, comparison between known albedos and the reflected radiation values can be used to determine the type of surface (i.e. high values, around 70%, suggest snow; low values, around 10%, suggest transparent ice). This information could be used to assign albedo and extinction coefficients to regions of the lake for input to a numerical model. However, the use of visible wavelength data alone was not considered to be accurate enough, and so an additional method was used.

The Normalised Difference Snow Index (NDSI), defined as the difference over the sum of the 0.55 μm (blue) and 1.6μm (reflected infra-red) channels, was used to discriminate between land, cloud and snow/ice/water pixels. Further separation of the latter into 11 classes (e.g. water, clear ice, white ice, fresh snow, snow melt pond etc.) was achieved by applying threshold values of near infra-red reflectance and brightness temperature, as given in table 6.1. Classification images derived from these thresholds of NDSI, NIR and BT are used to assign values of albedo and extinction coefficient to each surface type, as required by the numerical model in Chapter 5 to determine the extent to which solar radiation penetrates under ice.

The percentage cover of the main classes (snow, ice and water), using each classification image, was plotted as a function of time. This showed that snow-free ice dominates between January and February, and between April and May, whereas snow-covered ice is most prevalent in March. This agrees well with historical observations, providing a good indication that the classification analysis is sufficiently accurate for incorporation into the numerical model.

Table 6.1 Thresholds, albedos and extinction coefficients for each classification type. Two sets of albedo and extinction coefficient are given, as used to determine the effect of varying these parameters.

Classification type	Thresholds			Assigned albedo (%)	Extinction coefficient (m^{-1})
	NIR	BT	NDSI		
Water	< 4%	> 270 K	> 0.55	5/6	0.2/0.2
Clear (fresh) ice	< 15%	< 270 K	> 0.55	25/30	0.2/0.3
Slush ice	< 15%	> 270 K	> 0.55	20/24	3.5/3.5
Frazil ice	< 30%	> 270 K	> 0.55	25/30	3.5/3.5
Fresh white ice	< 55%	< 255 K	> 0.55	45/54	2.0/3.5
Old white ice	< 55%	> 255 K, < 270 K	> 0.55	40/58	3.0/3.5
White ice melt pond	< 55%	> 270 K	> 0.55	38/46	3.0/3.5
Clear/white ice mix	< 30%	< 270 K	> 0.55	30/36	0.8/1.0
Ice/snow mix	55%, < 70%	< 270 K	> 0.55	50/60	2.0/3.5
Snow melt pond	55%, < 70%	> 270 K	> 0.55	58/70	40.0/40.0
Snow	> 70%	< 270 K	> 0.55	60/72	40.0/40.0

6.2.3 Barotropic model

A single layer barotropic model was developed to investigate the hydrodynamics of Lake Baikal. Of particular interest were the factors which influence the formation of gyres, observed in satellite images, and thought to be a possible mechanism for ventilation of deep water.

The model reproduces standing waves known as seiches, a) as predicted by the Merian formula when the model basin has a uniform depth, and b) as observed in Lake Baikal when a realistic basin topography is applied. This shows that seiche oscillations are highly dependant on lake topography.

Current speeds generated in model runs forced only by river inflow/outflow are between one and two orders of magnitude smaller than those observed in Lake Baikal. Also, the circulation patterns seen in the lake are not reproduced by this model.

Eddy structures are reproduced in the model due to a combination of wind forcing (from the north-west), basin topography (specifically the Academician Ridge) and the Coriolis force. Although a 'true' gyre was not generated, it is likely that the same factors are highly influential in their formation in Lake Baikal.

The failure to reproduce true gyres and circulation cells may be due to the following limitations:

- Only barotropic motion is resolved by this model. If the observed gyre, or circulation cells, are baroclinic effects (i.e. arise due to density variations), they cannot be reproduced by this model.
- The observed gyre may arise due to interactions between the circulation cells in the North and Central basins. As these are themselves not reproduced by the model, it may not be possible for the gyre to be reproduced.
- Interactions between the land and the water may be unrealistic in this model. The viscosity of the water has been increased at the boundary regions, but this may not adequately reproduce the effect of friction between the water and the coast.
- Wind stress has not been applied realistically in the model. A constant stress at all points on the lake, as used in the model, is an unrealistic approximation of the temporally and spatially varying wind field which occurs naturally.

6.2.4 Multi-layer model

In order to study hydrodynamic processes in Lake Baikal a multi-layer model (including both the baroclinic and barotropic wave modes) was developed from an existing two-layer baroclinic only model. The primary aim of the model was to investigate under-ice heating and current flow, which are thought to influence strongly the motion of diatoms in the upper few hundred metres of the lake. The model was used in conjunction with satellite data of the lake, which determines the extent to which solar radiation penetrates the ice and snow to heat the water beneath.

Model temperature profile development from the initial date (using *in situ* data for 13th March 1997 (Jewson, personal correspondence)) to the final date 100 days of model integration time later (equivalent to 21st June) compares extremely well with *in situ* profiles over the same period at an equivalent point on the real lake. This suggests that the parameterisations used in the model are an adequate representation of the physical processes which occur in the lake.

Temperature profile development varies depending on the type of snow or ice present at that location. The mixed layer extends to a greater depth under regions of snow-free transparent ice than under snow-covered white ice. Regions which are well mixed are likely to have a higher diatom population in the real lake, as strong vertical mixing is required to keep the diatoms in suspension.

Under-ice currents generated by the model flow from regions of low to high density. As water beneath snow-free ice warms, its density increases, causing it to sink. As it does so, water from the surrounding region is drawn towards the high-density region, resulting in the observed flow from low to high density regions. This is consistent with observation, allowing the flow of

nutrients into regions of high diatom concentration. Maximum current speeds in the model are, however, about one order of magnitude smaller than those measured in the real lake.

These results show that it is possible to predict, to a certain extent, the development of the temperature structure and the direction of current flow in Lake Baikal during the ice-covered period.

A 20% increase in albedo values has only a small impact on the temperature, resulting in an overall decrease in temperature of about 0.05°C over the three month period investigated, and a decrease in the maximum current speed of about $2x10^{-4}$ ms^{-1}. This is a relatively insignificant difference, implying that this model is therefore not overly sensitive to small changes in albedo.

Decreasing or increasing the snow thickness by $1.5x10^{-2}$ m results in a maximum increase/decrease in the top layer temperature of 0.1°C, and a maximum decrease/increase in the current speeds of about $4x10^{-4}$ ms^{-1}. The effect is most noticeable initially, when the lake is predominantly snow covered.

Running the model with two slightly different sets of extinction coefficients (Table 6.1) results in a small initial difference in the temperature in the model lake (about 0.2°C cooler using the second, higher, set). The overall development of the temperature profile is, however, relatively unaffected, in that there is little difference between the final temperature profiles in the two model runs. Comparison with *in situ* data implies a slightly more realistic development of the temperature structure using the second set of extinction coefficients than the first.

The vertical mixing scheme which produces the most realistic development of the temperature profile is the *PP variant* scheme. When no parameterisation of vertical mixing is included in addition to convection, no deepening of the mixed layer occurs, indicating that there is little or no transfer of heat across the interface between the mixed layer and the stratified region. The *fixed profile* mixing scheme does reproduce this, but the temperature of the upper mixed layer is slightly warmer (by ~0.2°C) than the observation.

An additional aim of the model was to determine whether internal waves could be generated on the 250 m T_{mm} (mesothermal temperature maximum) interface with sufficient amplitude to induce a thermobaric instability, thus generating a deep water ventilation event. The model was run with two layers, with initial temperatures of 3.3°C (top layer) and 3.45°C (lower layer), the interface between the two lying at a depth of 250 m as in the real lake. A constant north-west wind stress was applied to the surface for a period of several days in order to set up motion on the interface. The model run with 50 ms^{-1} winds resulted in a deepening of the interface to the depth required for a thermobaric instability to be generated. A very strong, persistent wind stress would therefore be necessary in order to generate conditions required for thermobaric instability to occur. It is possible that deep convection events could arise from instabilities caused by depression of the 250 m interface, although such events are likely to be very rare due to the prolonged high wind speeds required.

6.3 Discussion of results from the baroclinic model

This is the first model of its kind to be discussed in open literature, and attempts to reproduce large-scale horizontal circulation patterns and vertical temperature profile development for a realistic Lake Baikal geometry, over the period of spring warming (March to June). It is important to study the full spatial variation of temperature and velocity as these parameters have a considerable impact on diatom suspension. In addition to the study of present-day diatom populations, this has consequences for the reconstruction of the climate record from diatoms in the lake sediment. For example, deposition rates must be known for particular sites in order to produce accurate climate reconstructions. Three-dimensional modelling is an important tool for studying ice-covered lakes, as very little data exists due to the difficulty in obtaining measurements. Temperature profile data tends to be for single locations at sparse time intervals, and measured current speeds can have errors of order 2 cm s^{-1} (Bengtsson, 1996).

The use of satellite data has been shown to be particularly useful for parameterising the spatial distribution of heat fluxes in the model. More ground-truthing would be required for a more accurate classification algorithm, but the accuracy of the temperature profile development in the model suggests that the current scheme is sufficient as it is presently used.

One of the questions arising from these results is why are the current speeds an order of magnitude smaller than those measured in the real lake. One possibility is that the effect of wind stress on the surface during the period of total ice cover has been assumed to be zero. However, wind-induced seiche oscillations have been observed in ice-covered lakes, giving rise to current speeds of a few cm s^{-1} (Bengtsson, 1996). The net current speed is small, as these currents typically alternate in direction with the same period as the seiche, a value which depends on the lake depth and length (see Chapter 4). This could also explain why the current flow under ice in Lake Baikal has been observed to change directions rapidly (Jewson, personal correspondence). Also, although an ice and snow layer is used in the model, the effect of this 'lid' on surface pressure has not been included. The high current speeds observed in the lake may be a result of this increased pressure, and are therefore not reproduced by this model. An incorrect parameterisation of heat fluxes through the ice could lead to errors in current speeds, for example if the differential heating was not strong enough. However, the consistency of the model-generated temperature profiles with observation suggests that this is unlikely. Another possible source of error is that the whole lake is initialised with the same *in situ* temperature profile, obtained from one point in the South Basin. In reality, however, there are likely to be some differences, which may cause stronger currents resulting from stronger temperature gradients. The difficulty in obtaining *in situ* data, particularly from the more inaccessible Central and North Basins, necessitated the use of a single initial profile.

6.4 The relative merits of other modelling techniques

Existing models which are one-dimensional in the vertical (Patterson and Hamblin, 1988), or two-dimensional in the horizontal and vertical (Killworth *et al.*, 1996), do not have the capability for reproducing under-ice currents caused by differential heating. The Killworth *et al.*(1996) model was used to investigate deep water ventilation events in Lake Baikal. No attempt was made to apply a realistic lake geometry or to modify heat fluxes due to ice and snow cover. Reducing the number of dimensions from three to two did allow long model integration times (several years), but this was not considered to be an important requirement for the work discussed here. Patterson and Hamblin (1988) describe a model which couples a one-dimensional lake mixing model with a thermodynamic model of the heat fluxes at the interfaces of ice and snow layers. Although the thermodynamic model would be an improvement over the simplifications used in the Killworth *et al.* (1996) model, it was thought to be too complex (and hence computational expensive) to incorporate into the required three-dimensional model. The Walker and Watts (1995) non-hydrostatic three-dimensional model has a high spatial resolution but, although suitable for investigating short time-scale events (~ few days), would be too computationally expensive to run for timescales of a few months which are required for studying under-ice current flow and mixing processes. Again, it also lacks the more detailed heat flux modification during snow and ice cover. Kelley (1997) investigates algal suspension by using analytical methods to model circulation flow fields (eddies). However, this restricts the study to simple geometry and steady flow only. It also concentrates on a relatively small spatial scale, i.e. individual circulation cells, rather than lake-wide circulation patterns, and provides no information on the temperature regime.

McCreary and Anderson (1983, 1991) describe an intermediate level model of the tropical Pacific Ocean. This was two-dimensional horizontally, with two vertical layers representing the ocean above and below the thermocline. This model became the framework for the N-layer (hence effectively three-dimensional) model of Lake Baikal used in this research. As described in Chapter 1, it allowed a three-dimensional investigation of temperature and current flow, on timescales of days to months necessary for the study of mixing processes affecting diatom suspension.

6.5 Suggestions for further work

6.5.1 The formation of gyres

As discussed in section 6.2.3 above, although eddies were formed in the barotropic model, true gyres were not reproduced for a number of possible reasons. These need to be addressed in order to progress any further with investigations into their formation and possible role as a mechanism of deep water ventilation. Firstly, it is likely that in the real lake, friction between the land and the water will have a significant impact on current flow. An adequate parameterisation

of this effect should, therefore, be included in the model. In addition, wind stress has not been applied realistically in the model due to the difficulty in obtaining real wind data of the lake region. Quantitative analysis and modelling of gyres will be severely restricted until such data become available.

6.5.2 Thermal bars and gyres as a mechanism for deep water ventilation

Although salinity levels in the lake are extremely small, the effect on the density when temperatures are close to that at which maximum density occurs could be significant. For example, deep water ventilation in the region of thermal bars and gyres may be aided by small increases in salinity. Therefore, in the baroclinic model, salinity should be included in the equation of state, so that this possibility can be explored.

6.5.3 Current flow under ice

River inflow and outflow is likely to have a significant impact on current flow in the lake, as shown in results from the barotropic model in Chapter 4. During the ice covered period the rivers are mostly frozen and so mass input to the lake is minimal. However, as the ice melts the rivers will become an important source of heat, salinity and momentum transfer. Sources and sinks should, therefore, be included in the baroclinic model for completeness.

Further investigation into the cause of the high currents observed in the lake during the ice covered period is needed, as these were not reproduced in the model by density gradients caused by differential heating. Parameterisation of an increased surface pressure due to the layer of ice may lead to more realistic current speeds. The effect of a wind stress on the ice surface should also be investigated, as currents have been observed under ice cover due to seiche oscillations (Bengtsson, 1996). Increasing the grid resolution could also be studied, to determine whether this has a significant effect on current speeds.

6.5.4 Investigation of deep water processes

To investigate processes which result in the ventilation of deep water, numerical modelling of the entire water column is required. At present, the model is limited to the depth at which the temperature profile crosses the line of the temperature of maximum density, around 250 m in the case of Lake Baikal. Initialising the lake with the full depth-temperature profile would result in numerical instability, as density apparently decreases with depth below 250 m. For the model to function correctly, the effect of high pressure on the density of water should be included in the model equations.

7. Bibliography

Abbott, M.B. and Basco, D.R., 1989. *Computational Fluid Dynamics, an Introduction for Engineers.* Longman Scientific and Technical

Bearman, G., (ed), 1989. *Ocean Circulation.* Pergamon Press and The Open University

Bengtsson, L., 1996. Mixing in ice-covered lakes. *Hydrobiologia.* **322**: 91-97

Bolgrien, D.W. and Brooks, A.S., 1992. Analysis of thermal features of Lake Michigan from AVHRR satellite images. *Journal of Great Lakes Research.* **18 (2)**: 259-266

Bolgrien, D.W., Granin, N.G. and Levin, L., 1995. Surface temperature dynamics of Lake Baikal observed from AVHRR images. *Photogrammetric Engineering and Remote Sensing.* **61 (2)**: 211-216

Callender, E. and Granina, L., 1997. Geochemical mass balances of major elements in Lake Baikal. *Limnol. Oceanog.* **42(1)**: 148-155

Carmack, E.C. and Weiss, R. F., 1991. Convection in Lake Baikal: an example of the thermobaric instability. *Deep Convection and Deep Water Formation in the Oceans.* **57**: 215-228, Elsevier Oceanography

Chen, C.T. and Millero, F.J., 1986. Precise thermodynamic properties for natural waters covering only the limnological range. *Limnol. Oceanog.* **31**: 657-662

Dean, R.G. and Dalrymple, R.A., 1984. *Water Wave Mechanics for Engineers and Scientists.* Prentice-Hall

Dorsey, N.E., 1968. *Properties of ordinary water-substance.* Hafner Publishing Company

Edwards, T., Browning, R., Delderfield, J., Lee, D. J., Lidiard, K. A., Milborrow, R. S., McPherson, P. H., Peskett, S. C., Toplis, G. M., Taylor, H. S., Mason, I., Mason, G., Smith, A. and Stringer, S., 1990, The Along Track Scanning Radiometer – measurement of sea-surface temperature from ERS-1. *J. Brit. Interplanetary Soc.* **43**: 160-180

Eklund, H., 1963. Fresh water: temperature of maximum density calculated from compressibility. *Science.* **142**: 1457-1458

Eklund, H., 1965. Stability of lakes near the temperature of maximum density. *Science.* **149**: 632-633

Farrow, D.E., 1995b. A numerical model of the hydrodynamics of the thermal bar. *Journal of Fluid Mechanics.* **303**: 279-295

Gill, A.E., 1982. *Atmosphere-Ocean Dynamics.* Academic Press

Goldman, C.R. and Horne, A., J., 1983. *Limnology.* McGraw-Hill Book Company

Grenfell, T.C. and Maykut, G.A., 1977. The optical properties of ice and snow in the arctic basin. *Journal of Glaciology.* **18**: 445-463

Hoffman, 1993. *Numerical methods for engineers and scientists.* McGraw-Hill Book Co., Singapore

Keller, H.B., 1978. Computational Fluid Dynamics.

Kelley, D. E., 1997. Convection in ice-covered lakes: effects on algal suspension. *J. Plankton Res.* **19(12)**: 1859-1880

Killworth, P. D., Carmack, E. C., Weiss, R. F. and Matear, R., 1996. Modelling deep-water renewal in Lake Baikal. *Limnol. Oceanog.* **41(7)**: 1521-1538

Kozhov, M., 1963. *Lake Baikal and its Life.* Dr. W. Junk, The Hague

Logatchev, N., 1993. History and geodynamics of the Lake Baikal rift in the context of the Eastern Siberia rift system. *BCREDP.* **17**: 353-370

Malm, J. and Jonsson, L., 1993. A Study of the thermal bar in Lake Ladoga using water surface temperature data from satellite images. *R. Sens. Environ.* **44**: 35-46

Malm, J., Jonsson, L, 1994. Water surface temperature characteristics and thermal bar evolution during spring in Lake Ladoga. *R. Sens. Environ.* **48** 332-338

Matthews, P.C. and Heaney, S.I., 1987. Solar heating and its influence on mixing in ice-covered lakes. *Freshwater Biology.* **18**: 135-149

McCreary, J.P. and Anderson, D.L.T., 1983. A model of El Nino and the Southern Oscillation.

McCreary, J.P. and Anderson, D.L.T., 1991. An overview of coupled ocean-atmosphere models of El Nino and the Southern Oscillation. *J. Geophys. Res.* **96** (Supplement): 3125-3150

Moore, J. K. and Villareal, T. A., 1996. Size-ascent rates relationships in positively buoyant marine diatoms. *Limnol. Oceanog.* **41**: 1514-1520

Morassutti, M.P., 1989. Surface albedo parameterization in sea-ice models. *Progress in Physical Geography.* **13 (3)**: 348-366

Mutlow, C.T., Zavody, A.M., Barton, I.J. and Llewellyn-Jones, D.T., 1994. Sea surface temperature measurements by the along-track scanning radiometer on the ERS 1 satellite: Early results. *J. Geophys. Res. (Oceans).* **99 (C11)**: 22,575-22,588

Pacanowski, R.C. and Philander, S.G.H., 1981. Parameterization of vertical mixing in numerical models of tropical oceans. *J. Phys. Oceanog.* **11**: 1443-1451

Patterson, J. C. and Hamblin, P. F., 1988, Thermal simulation of a lake with winter ice cover. *Limnol. Oceanog.*, **33(3)**: 323-338

Press, W.H., Flannery, B.P., Teukolsky, S.A. and Vetterling, W.T., 1986. *Numerical Recipes: The art of scientific computing*. Cambridge University Press

Riggs, G., 1995. MODIS snow and ice algorithm development. *First Moderate Resolution Imaging Spectrometer (MODIS) snow and ice workshop (proceedings)*. 55-60

Robinson, I.S., Wells, N.C. and Charnock, H., 1984. The sea surface thermal boundary layer and its relevance to the measurement of sea surface temperature by airborne and spaceborne radiometers - Review Article. *Int. J. Rem. Sens.* **5**: 19-45

Shimaraev, M.N., Granin, N. G. and Zhdanov, A. A., 1993. Deep ventilation of Lake Baikal waters due to spring thermal bars. *Limnol. Oceanog.* **38 (5)**: 1068-1072

Shimaraev, M.N., Verbolov, V.I., Granin, N.G. and Sherstyankin, P.P., (ed), 1994. *Physical limnology of Lake Baikal: A review*. BICER, Irkutsk - Okayama 1994

Shine, K.P. and Henderson-Sellers, A., 1985. The sensitivity of a thermodynamic sea ice model to changes in surface albedo parameterization. *J. Geophys. Res.* **90 (D1)**: 2243-2250

Skabitchevsky, A. P., 1929. Concerning the biology of Melosira baicalensis. *Russian Hydrobiological Journal.* **8**: 93-113

Stockdale, T.N., 1992. Simulation and prediction of tropical SST with a coupled ocean-atmosphere model. *PhD thesis*. 241

Votinsev, K. K. and Popovskaya, G. I., 1964. On the state of Melosira baicalensis, sinking in the depths of Lake Baikal. *Dokl. Acad. Scien. USSR*. **155**: 673-676

Walker, S. J. and Watts, R. G., 1995. A three-dimensional numerical model of deep ventilation in temperate lakes. *J. Geophys. Res.* **100 (C11)**: 22,711-22,731

Weiss, R. F., Carmack, E. C. and Koropalov, V. M., 1991. Deep-water renewal and biological production in Lake Baikal. *Nature*. **349**: 665-669

Yu, Y., Rothrock, D. A. and Lindsay, R. W., 1995. Accuracy of sea ice temperature derived from the advanced very high resolution radiometer. *J. Geophys. Res.* **100 (C3)**: 4525-4532

Zavody, A.M., Mutlow, C.T. and Llewellyn-Jones, D.T., 1995. A radiative transfer model for sea-surface temperature retrieval for the along-track scanning radiometer. *J. Geophys. Res. (Oceans)*. **100 (C1)**: 937-952

Zilitinkevich, S.S., Kreiman, K.D. and Terzhevik, 1992. The thermal bar. *Journal of Fluid Mechanics*. **236**: 27-42